

**WIDE FIELD OF VIEW CT:
CLINICAL IMPACT IN MEDICAL IMAGING**

JOHN MIKEY TROUPIS

BACHELOR OF MEDICINE, BACHELOR OF SURGERY

CLINICAL SCHOOL, MONASH HEALTH

2013 NOVEMBER 25

Notice 1

Under the Copyright Act 1968, this thesis must be used only under the normal conditions of scholarly fair dealing. In particular no results or conclusions should be extracted from it, nor should it be copied or closely paraphrased in whole or in part without the written consent of the author. Proper written acknowledgement should be made for any assistance obtained from this thesis.

TABLE OF CONTENTS

| | |
|----------|--|
| PAGE 4: | ACADEMIC/SCHOLARLY WORK- 4 DIMENSIONAL COMPUTER TOMOGRAPHY NATIONAL & INTERNATIONAL PRESENTATIONS |
| PAGE 6: | SUMMARY/ABSTRACT |
| PAGE 7: | GENERAL DECLARATION: |
| PAGE 8: | INTRODUCTION |
| PAGE 12: | 1. CORONARY IMAGE QUALITY OF 320-MDCT IN PATIENTS WITH HEART RATES ABOVE 65 BEATS PER MINUTE: PRELIMINARY EXPERIENCE |
| PAGE 23: | 2. COMPARISON OF 4CM Z-AXIS AND 16 CM Z-AXIS MULTIDETECTOR CT PERFUSION |
| PAGE 33: | 3. NORMAL PERFUSION OF THE LEFT VENTRICULAR MYOCARDIUM USING 320 MDCT |
| PAGE 43: | 4. MYOCARDIAL DENSITY ANALYSIS UTILIZING AUTOMATED MYOCARDIAL DEFECT ANALYSIS SOFTWARE ON RESTING 320-DETECTOR MDCT |
| PAGE 53: | 5. THE NEW 4-DIMENSIONAL COMPUTED TOMOGRAPHIC SCANNER ALLOWS DYNAMIC VISUALISATION AND MEASUREMENT OF NORMAL ACROMIOCLAVICULAR JOINT MOTION IN AN UNLOADED AND LOADED CONDITION |
| PAGE 62: | 6. DYNAMIC MOTION ANALYSIS OF DART THROWERS MOTION VISUALIZED THROUGH COMPUTERIZED TOMOGRAPHY AND CALCULATION OF THE AXIS OF ROTATION |

PAGE 74: 7. FOUR-DIMENSIONAL COMPUTED TOMOGRAPHY AND TRIGGER LUNATE SYNDROME

PAGE 82: DISCUSSION/CONCLUSION

PAGE 87: REFERENCES/BIBLIOGRAPHY:

ACADEMIC/SCHOLARLY WORK- 4 DIMENSIONAL COMPUTER TOMOGRAPHY

NATIONAL & INTERNATIONAL PRESENTATIONS

1. KEY NOTE SPEAKER : INAUGURAL CONFERENCE –CLINICAL IMPACT OF VOLUMETRIC & HELICAL CT IMAGING, TORONTO, CANADA, 2013 APRIL
 - a. VOLUME IMAGING OF AIRWAYS
 - b. INITIAL EXPERIENCE USING HIGH SPEED TRUE VOLUME CT
2. RADIOLOGICAL SOCIETY OF NORTH AMERICA: ORAL SCIENTIFIC PRESENTATION:
 - a. 2013 – DYNAMIC FOUR DIMENSIONAL CT IMAGING FOR RE-ENTRY RISK ASSESSMENT IN RE-DO STERNOTOMY
 - b. 2012—4D CT AND LUNG CANCER OPERABILITY
3. AMERICAN ROENTGEN RAY SOCIETY ORAL SCIENTIFIC PRESENTATION:
 - a. 2013- 4D CT AND UPPER LIMB MOTION DISORDERS
4. SOCIETY OF CARDIOVASCULAR CT 2011, LAS VEGAS, USA- ELECTRONIC EXHIBITS
 - a. DIAGNOSTIC ACCUARACY OF 320 SLICE CARDIAC CT IN PATIENTS WITH ATRIAL FIBRILLATION BY CLINICAL OUTCOME: A PILOT STUDY WITH NINE MONTH FOLLOW-UP
 - b. CORONARY IMAGE QUALITY OF 320 MDCT IN PATIENTS WITH HEART RATES ABOVE 65 BEATS PER MINUTE: PRELIMINARY EXPERIENCE
 - c. NORMAL PERFUSION OF THE LEFT VENTRICULAR MYOCARDIUM USING 320 MDCT
5. INTERNATIONAL CONGRESS OF SHOULDER & ELBOW SURGERY APRIL 2013: 4D CT SCANS IMPROVE PRE OPERATIVE PLANNING IN SNAPPING SCAPULAR SYNDROME
6. ROYAL AUSTRALIAN & NEW ZEALAND COLLEGE OF RADIOLOGISTS ANNUAL SCIENTIFIC MEETING PRESENTATIONS:
 - a. 2013- RESPIRATORY DYNAMIC WIDE AREA DETECTOR 4D CT FOR DETERMINATION OF LUNG CANCER OPERABILITY

7. RADAIM 2013, MELBOURNE : INVITED GUEST SPEAKER- 4D CT AND AIRWAYS, 4D CT AND MUSCULOSKELETAL SYNDROMES

SUMMARY/ABSTRACT

Although Computer Tomography (CT) has been widely used for medical imaging over the previous thirty years, recent advances in the superior to inferior coverage of multidetector systems have contributed to the introduction of wide field of view CT units. The immediate clinical benefit of wide field of view is the ability to apply the scan to a region of interest with a view to avoiding table motion, should the coverage with one gantry rotation be adequate.

We considered investigating wide field of view CT and determining other potential benefits, which may not be readily visible. Areas of interest include myocardial tissue and the ability to assess density of the entire heart at the same point in time, brain perfusion and joint motion assessment.

We determined that certain absolute parameters for imaging the heart with regard to temporal resolution no longer need to be met, and establishment of baseline myocardial density values were of importance considering the significant impact of volumetric imaging in the setting of myocardial perfusion and both rest and stress assessment.

Baseline measurements for previously poorly assessed and poorly understood joints were determined, including the acromioclavicular and wrist joints.

A significant benefit of investigating abnormal wrist motion was the discovery of a clinical entity which has previously not been appreciated, that of trigger lunate syndrome.

We propose that wide field of view CT, and in particular 4D CT, have a significant benefit in clinical imaging, and that 4D CT may be considered a new imaging technique allowing us to visualize and examine motion and perfusion disorders which have previously either been not possible or significantly limited.

PART A: General Declaration

Monash University

Declaration for thesis based or partially based on conjointly published or unpublished work

General Declaration

In accordance with Monash University Doctorate Regulation 17.2 Doctor of Philosophy and Research Master's regulations the following declarations are made:

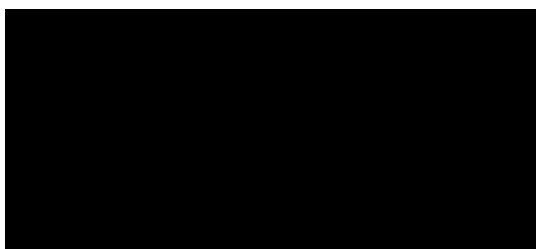
I hereby declare that this thesis contains no material which has been accepted for the award of any other degree or diploma at any university or equivalent institution and that, to the best of my knowledge and belief, this thesis contains no material previously published or written by another person, except where due reference is made in the text of the thesis.

This thesis includes seven original papers published in peer reviewed journals and no unpublished publications. The core theme of the thesis is wide field of view computer tomography and clinical impact in medical imaging. The ideas, development and writing up of all the papers in the thesis were the principal responsibility of myself, the candidate, working within the Monash Health Clinical School under the supervision of Julian Smith.

The inclusion of co-authors reflects the fact that the work came from active collaboration between researchers and acknowledges input into team-based research.

I have not renumbered sections of submitted or published papers in order to generate a consistent presentation within the thesis.

Signed: JOHN MIKEY TROUPIS



Date: 13 NOVEMBER 2013

INTRODUCTION

Computer Assisted Tomography (CT) was first reported by Hounsfield in 1973 [1, 2]. The first prototype was installed in Atkinson Morley's Hospital in South London and used the translate/rotate principle where the gantry scanned across the region of the interest and then rotated by one degree prior to scanning back across the field of view with a different angulation. [3] This process was repeated until the region of interest was scanned with numerous angulations so that appropriate filtered back projection mathematical calculations could be applied to reconstruct an image of the portion of the human anatomy being scanned. These early CT scanners were referred to as first and second generation.

Further development resulted in third generation CT scanners which utilized the rotate/rotate principle where the mostly xenon gas detectors were arranged in an arc to offer faster scan times. [4]

With the advent of helical [5] and multislice scanning in 1998[6], four slice acquisitions were possible with rapid acquisition. Multislice CT scanning involves widening the xray beam and adding several detector rows in the superior-inferior axis (Z axis), with advantages of reduced heat loading, reduced time of acquisition, and simultaneous data acquisition.

Over the last several years, further advances in CT technology have resulted in 16 slice[7], 64 slice[8] and recently in both 256 and 320 slice capability[9].

The introduction of 64 slice technology in 2005 offered both reduced slice thickness (down to 0.5mm), thereby making isotropic volume data sets possible, and in additionally offered markedly improved acquisition times for scanning large areas of the body[10]. This resulted in significant clinical benefits in large parts of the human body which were previously difficult to assess due to the vascularity, thereby requiring rapid scanning.

However, one of the more significant benefits of 64 slice multidetector system was the introduction of a wider superior-inferior (z) axis coverage with one rotation of the xray gantry. These systems were able to scan 4cm in the z axis. The wide coverage renders dynamic CT imaging of a volume of tissue feasible. The term 4 Dimensional Computed Tomography (4D CT) was introduced. The first three dimensions are those used in conventional CT (depth, width, height), with the fourth dimension representing motion[11]. 4D CT requires a two-dimensional detector with a large area in conjunction with a continuous rotating gantry capable of high speeds. CT data is acquired repeatedly at a stationary table position with the obtained information then correlated with respiration. This enables the movement of structures to be visualised[11, 12]. The data is reconstructed as a volume image which enables the images to be assessed with any available post processing work station capability. Due to the 4cm limitation in the field of view, the clinical utility of 4D CT in the diagnostic arena remained limited. However in the therapeutic arena, the impact had been significant. 4D CT has been used to verify the position of a lung tumour during volumetric arc therapy, which enables the arc therapy to be delivered using the entire 360 degrees of beam directions in order to optimize the dose delivery to the entire volume of tissue within a single source rotation[13]. With regard to radiation therapy in the setting of oncology management, 4D CT has also been utilized to provide an accurate position of the lung cancer during the entire respiratory cycle, with the aim to more accurately deliver the relevant dose[14].

In four-dimensional volumetric modulated arc therapy, the entire breathing cycle is incorporated into the optimisation process using 4DCT data. Delivery of the radiotherapy beam can be synchronised with a specific phase of target motion, enabling more sparing of healthy tissue[15].

Improved assessments were now possible for scanning of the coronary arteries[16, 17], coronary artery bypass grafts[16], gastrointestinal bleeding[18], small bowel and large bowel

obstruction[19], acute multitrauma[20], head and neck angiography[21, 22], neoplasm assessment[23] and vascular anomalies[24].

The 64-slice technology resulted in 4 cm z-axis coverage. More recent developments have aimed to improve the ability to reliably and repeatedly scan the coronary arteries. This vision has resulted in the introduction of CT scanners with further increase in the wide field of view z-axis coverage, either using 256 detectors (8cm) or 320 detectors (16 cm). Due to the volumetric coverage, significant benefits in tissues which are prone to motion artefact has resulted especially with regard to coronary artery computed tomography[25, 26].

The wide field of view CT has significantly contributed toward an improvement in coronary artery visualisation[9, 26] whilst allowing visualization of previously difficult to identify cardiac conditions such as arrhythmogenic right ventricular cardiomyopathy[27].

Although the development of wide field of view has been with coronary artery scanning as the region of interest, due to the nature of the technical innovation, we have postulated that if the region being scanned (either cardiac or non cardiac) were to remain within the scan range (ie no table motion) with subsequent continual scanning, the acquired volume data set would be updated thereby showing motion which may be assessed in numerous planes. By using the principle used previously for radiation therapy planning purposes, 4D CT may potentially be of use in a number of regions, in particular in the visualization of cardiac motion or wrist motion, which can be examined from numerous planes.

As the clinical utility of 4D CT is relatively unknown, our aim is to explore regions of the body, which are subject to either rapid change in anatomy with time or rapid change of density with time.

The wide field of view technology was initially developed with a view to improving coronary cardiac CT capabilities by being able to scan the entire heart in one heart beat. We aim to provide confirmation that significant advances in cardiac imaging have been achieved, and

that the principles of needing to achieve a patient heart rate below the temporal resolution of the scanner and needing to have a patient in sinus rhythm, do not necessarily need to be followed with this technology. Furthermore when considering the myocardial density, which can vary from superior to inferior depending on timing of contrast, we aim to investigate whether wide field of view CT offers clinical insight into myocardial density abnormalities, whether non ischaemic or ischaemic.

As in index case in the investigation of abnormal angiography, we consider the issue of brain perfusion and the issue of whether wide field of view has advantages over traditional field of view with regard to recognition and detection of abnormalities.

We will then consider musculoskeletal imaging, in particular joint imaging. It is well accepted that numerous instability and / or impingement conditions can afflict a number of joints. Due to the symptoms associated with motion, these conditions have been poorly assessed previously due to the static nature of previous imaging. We have selected the acromion-clavicular (AC) joint and the wrist joint as index research.

In conclusion, our aim is to investigate an index case in the various regions identified where our research paper will likely stimulate further research.

CHAPTER 1:**CORONARY IMAGE QUALITY OF 320-MDCT IN PATIENTS WITH HEART
RATES ABOVE 65 BEATS PER MINUTE: PRELIMINARY EXPERIENCE**

The development of 64 slice multidetector CT units with isotropic resolution resulted in a significant impact on medical imaging as techniques previously considered not possible were now easily available. These included high resolution multiplanar reconstructed images especially of the vascular anatomy but also including the liver, lung and neurological systems. Post processing applications were now also possible such as markedly improved metallic artefact reduction, and perfusion assessments. However although imaging of the heart chamber morphology was adequate, coronary artery CT was subject to the traditional limitations imposed by the temporal resolution of the CT unit and by the multisegment reconstruction acquisition technique, which is prone to stair step artefact [28-30].

As the concept of wide field of view computed tomography was the result of a concerted effort to improve the diagnostic quality of coronary artery computed tomography angiography, the initial emphasis of this class of CT units has been for installation in the centres which target cardiac imaging. Cardiovascular centres world wide began to install such units, with a view to improved coronary artery CT image quality which is not subject to traditional limitations.

The evaluation of wide field of view CT imaging of the heart has not been extensively studied prior to the universal acceptance of installation. Due to the volumetric nature of data acquisition, we considered whether the previously established principles of heart rate manipulation in order to reach level below the temporal resolution of the CT unit, were still required.

Our first examination of the impact of wide field of view CT imaging was to demonstrate that temporal resolution of the CT unit is no longer an absolute limitation, and that for this type of imaging, it may be considered a relative limitation. In particular, our aim was to determine whether, wide field of view CT cardiac imaging and the concept of volumetric imaging was able to modify the generally accepted limitation of CT units through their temporal resolution.

In summary, the work was performed to investigate whether volumetric CT scanning was able to allow imaging principles to bypass previously held limitations in cardiac coronary artery imaging.

Declaration for Thesis Chapter ONE

Declaration by candidate

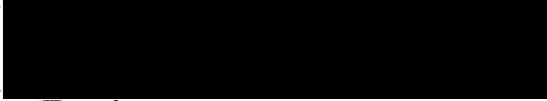
In the case of Chapter One, the nature and extent of my contribution to the work was the following:

| Nature of contribution | Extent of contribution (%) |
|--|----------------------------|
| Creation of idea, development of structure of the retrospective analysis, creation of the team of researchers, intimately involved with the writing of the paper, guiding the primary author who had very limited experience in this field | 50 |

The following co-authors contributed to the work. If co-authors are students at Monash University, the extent of their contribution in percentage terms must be stated:

| Name | Nature of contribution | Extent of contribution (%) for student co-authors only |
|-------------------------|--|--|
| Allan B Lee | Responsible for co ordination of review and primary authorship | Not a University student |
| Dee Nandurkar | Assisted with review of the studies | Not a University student |
| Michal Schneider-Kolsky | Statistical analysis | Not a University student |

The undersigned hereby certify that the above declaration correctly reflects the nature and extent of the candidate's and co-authors' contributions to this work*.

| | | |
|---------------------------------|--|---------------------|
| Candidate's Signature |  | Date 12 Nov 2013 |
| Head of Department's Signature* |  | Date 12/11/13 |

Coronary Image Quality of 320-MDCT in Patients With Heart Rates Above 65 Beats per Minute: Preliminary Experience

Allan B. Lee¹
Dee Nandurkar¹
Michal E. Schneider-Kolsky²
Marcus Crossett^{1,3}
Sujith K. Seneviratne³
James D. Cameron³
John M. Troupis^{1,3}

Keywords: 320-MDCT, cardiac CT, heart rate above 65 beats/min

DOI:10.2214/AJR.10.5252

Received July 2, 2010; accepted after revision November 7, 2010.

¹Department of Diagnostic Imaging, Monash Medical Centre, Southern Health, 246 Clayton Rd, Clayton, Victoria 3168, Australia. Address correspondence to J. M. Troupis (John.Troupis@southernhealth.org.au).

²Department of Medical Imaging and Radiation Sciences, Faculty of Medicine, Nursing and Health Sciences, Monash University, Melbourne, Australia.

³MonashHEART, Southern Health and Department of Medicine, Monash University, Monash Cardiovascular Research Centre, Clayton, Victoria, Australia.

WEB

This is a Web exclusive article.

AJR 2011; 196:W729–W735

0361–803X/11/1966–W729

© American Roentgen Ray Society

OBJECTIVE. High heart rate may negatively influence the image quality of cardiac CT. The technical advances of 320-MDCT may overcome issues with poor image quality associated with high heart rate. This study aimed to evaluate the coronary image quality of 320-MDCT in patients with heart rates above 65 beats/min.

MATERIALS AND METHODS. Patients who presented for cardiac CT were divided into two groups according to heart rate, either greater than 65 beats/min or less than or equal to 65 beats/min. Two radiologists were blinded to the patient groups and evaluated images of 15 coronary artery segments per patient using 320-MDCT with consensus agreement. The image quality was scored subjectively as 1 or 2 (diagnostic quality) or 3 (poor quality and nondiagnostic).

RESULTS. There were no statistically significant differences between the two groups in terms of age, sex, and body mass index ($p > 0.05$). The median heart rate was 70 beats/min (range, 67–110 beats/min) for the group with heart rate greater than 65 beats/min and 60 beats/min (range, 48–65 beats/min) for the group with heart rate less than or equal to 65 beats/min ($p < 0.001$). In patients with heart rates greater than 65 beats/min, diagnostic quality images (scores of 1 or 2) were obtained in 95.6% of the analyzed segments, compared with 96.9% in the group with heart rate less than or equal to 65 beats/min ($p = 0.7$).

CONCLUSION. Our initial evaluation suggests that coronary artery images of diagnostic quality can be obtained using 320-MDCT in most patients with heart rates greater than 65 beats/min, in percentages similar to those for patients with heart rates less than or equal to 65 beats/min. This finding may be the result of the inherent image acquisition and reconstruction technique of 320-MDCT.

Cardiac CT is a rapidly evolving noninvasive technique used in the detection and assessment of coronary artery disease. The images produced by cardiac CT need to be of high quality for it to be a sensitive and diagnostic tool.

Patient-specific factors such as high heart rate may degrade the image quality of cardiac CT [1]. High-quality images free of cardiac motion artifact may be obtained by slowing the heart rate [2]. The current practice is aimed at decreasing the heart rate to below 65 beats/min, often with β -blocker medication, before cardiac CT [3, 4]. Alternatively, the temporal resolution of the scanner needs to be fast enough to freeze the heart motion [3]. The temporal resolution of the scanner is limited by the gantry rotation time, which is the time needed to complete a 360° revolution. The temporal resolution of a single tube and detector system is one half of the gantry

rotation time, because image reconstruction requires 180° [2]; 320-MDCT uses multisegment reconstruction to improve the effective temporal resolution by using data from more than one R-R interval of the cardiac cycle to reconstruct an image [5]. Using this method, an effective temporal resolution of 87.5 milliseconds can be obtained if two-segment reconstructions are used, compared with the temporal resolution of a dual-source scanner, which ranges from 75 to 83 milliseconds [2, 5]. The trade-off for using multisegment reconstruction is higher radiation dose to the patient as a result of longer exposure time.

With 16 cm of craniocaudal coverage per gantry rotation, 320-MDCT enables scanning of the whole heart in a single heartbeat, thereby eliminating the “stair-step” artifact [3]. This artifact occurs as a result of sub-volume cardiac imaging over multiple gantry rotations, leading to nonoverlapping reconstruction intervals [6]. All scan data can be

obtained in the same R-R interval, which enables scanning of patients with arrhythmias [7]. The wide area detector coverage decreases the overall scan time, thereby allowing the contrast material bolus to be imaged at a single time point. This results in uniform contrast in the arterial tree [5]. Experimental cardiac CT applications such as myocardial perfusion and coronary artery contrast opacification gradients have used this feature of 320-MDCT [2, 8]. In comparison, the dual-source scanner has less volume coverage per gantry rotation, between 1.9 and 3.84 cm [2, 5].

Prospective and retrospective ECG gating are used in cardiac CT to synchronize image acquisition with the cardiac cycle [9], thereby minimizing motion artifact. During retrospective gating, data are acquired throughout the cardiac cycle, enabling image reconstruction at any cardiac phase. Retrospective gating is used in cardiac functional and valve assessment. In prospective gating, scanning occurs during the set R-R interval. The latter is associated with significant reduction in radiation exposure [2].

Patients who present for cardiac CT may have high heart rates refractory to the effects of β -blocker medication, which often is administered as part of the standard protocol to lower heart rate before scan acquisition. High heart rate can be associated with deterioration in image quality of cardiac CT. To our knowledge, the coronary image quality of 320-MDCT in patients resistant to β -blockade with heart rates greater than 65 beats/min has not been specifically evaluated. We hypothesize that diagnostic-quality images are reproducible in this cohort because of improved image acquisition and reconstruction technique of 320-MDCT.

Materials and Methods

Patients and Study Protocol

This study was performed as a retrospective audit and was approved by the institutional review board affiliated with our hospital. A total of 390 cardiac imaging scans were performed during the study period from September 2008 to February 2009. In this period, 45 consecutive patients with heart rates greater than 65 beats/min were identified. Of this subgroup, 15 patients were excluded from the retrospective analysis because of targeted examination of noncoronary cardiac structures. As a result, 30 patients with heart rates greater than 65 beats/min were included for review. An additional 30 patients with heart rates of 65 beats/min or less who underwent cardiac CT

for coronary artery evaluation were allocated to the control group. Patients in the control group were matched to the subjects in terms of sex, age, and body mass index (BMI), where possible, to minimize confounding variables.

Patients were selected from routine clinical referrals with acute chest pain, exertional angina, or increasing shortness of breath. No patients were excluded because of previous coronary intervention, including stenting and presence of atrial fibrillation.

The exclusion criteria were the presence of congenital heart disease other than patent foramen ovale or atrial or ventricular septal defects. These were selected to minimize variations to standard coronary artery anatomy, which may otherwise affect assessment of image quality.

Patient demographics, including sex, age, and BMI, were documented. After selection, patients were identified by their unit record number only. The radiologists were blinded to the patient's heart rate.

The patients fasted for at least 2 hours before scan acquisition and abstained from caffeine on the day of scanning, as per standard protocol. Each patient's heart rate and blood pressure were recorded 1 hour before imaging. An 18-gauge IV cannula was inserted into the right antecubital fossa.

All patients with heart rates greater than 60 beats/min were administered β -blocker medication unless contraindicated (e.g., anaphylaxis or severe asthma). Patients with heart rates between 60 and 70 beats/min with systolic blood pressure of greater than 100 mm Hg were given 50 mg of oral metoprolol. If the heart rate and blood pressure were above 70 beats/min and 100 mm Hg, respectively, 100 mg of oral metoprolol was administered. If the heart rate remained above 65 beats/min immediately before scanning, a 5-mg dose of IV metoprolol was administered. The dose was titrated up by 1 mg per minute to a maximum of 25 mg, depending on the heart rate and blood pressure response. Four hundred micrograms of sublingual glyceryl trinitrate spray was given 2 minutes before imaging for coronary artery vasodilatation. The patients who failed to reach the target heart rate of 65 beats/min or less were included in the high heart rate group. The reasons for the inability to decrease the heart rate to less than or equal to 65 beats/min with β -blocker therapy have not been documented for individual patients. They included development of borderline hypotension with systolic blood pressure of approximately 100 mm Hg, acute exacerbation or history of severe exacerbation of asthma or chronic obstructive pulmonary disease, or resistance to the effects of maximal β -blocker premedication according to protocol. In some patients who were initially "well β -blocked," the heart rates increased to greater than 65 beats/min during scan acquisition.

Seventy-five to 100 mL of IV contrast agent was administered for each patient (Ultravist 370, Bayer HealthCare) at a rate of 6 mL/s, followed by 50 mL of normal saline flush. Bolus tracking with a region of interest placed in the left ventricle was performed using a 180 HU threshold.

Image Acquisition

Images were acquired using a 320-MDCT scanner (Aquilion One, Toshiba Medical Systems). The field of view (z-axis) included the mid-ascending aorta to the upper abdomen. No table movement occurred during axial volumetric scanning because the scanner provides 16 cm of z-axis volume using 0.5-mm detectors. The number of detectors selected was based on cardiac size as displayed on the anteroposterior and lateral surface images. All relevant cardiac anatomy was successfully displayed on the field of view. No patient required more z-axis coverage than the scanner detector bank could cover in a single acquisition.

Tube voltages used were between 100 and 135 kVp, on the basis of the patient's BMI, according to the vendor's specifications. Tube current ranged between 400 and 580 mA. A medium field of view was selected. The gantry rotation time was 350 milliseconds, with a minimum temporal resolution of 175 milliseconds [6]. Single gantry rotation generally occurred if images were obtained with heart rate of 65 beats/min or less. Acquisition was generally obtained over two or more heartbeats, triggered by the scanner "arrhythmia rejection" software if the heart rate went above 65 beats/min or if atrial fibrillation was detected. Data acquisition was automatically terminated by the scanner if a total of four heartbeats were reached.

If functional information (e.g., left ventricular ejection fraction) was not required, end-diastolic prospective scanning with an ECG-gated window of 65–99% of the R-R interval was performed. If functional information was required, full R-R retrospectively gated scan was acquired in one to four heartbeats. ECG dose modulation was used to reduce radiation dose with this method by decreasing tube current during the systolic phase of the R-R interval [10].

Images were obtained in moderate inspiration with breath-holding. Breath-holding and heart rate tests were performed before image acquisition. The final heart rate was recorded at the time of acquisition.

Image Reconstruction

Raw data reconstruction was performed using 0.5-mm slices in 0.25-mm intervals at 75% of the R-R phase. If full R-R scanning was performed, functional information at 1-mm contiguous slices was reconstructed at 10% intervals from 0–90%

320-MDCT in Patients With Elevated Heart Rates

of the R-R phase. A default medium soft-tissue kernel (FC04) was used.

If there was movement artifact in a vessel on initial review, a more optimal phase to minimize the effect was chosen with reconstruction at 20-millisecond intervals across all available phases. After this, an additional 0.5×0.25 mm motion-free reconstruction was performed.

ECG editing was used in patients with atrial fibrillation who underwent multibeam acquisition to obtain an optimal reconstruction phase. This involved deselecting the R peak of the shorter heart-beat and rejecting it from the dataset, resulting in a half segmental reconstruction from a multisegment acquisition.

Postprocessing and Image Analysis

Images were reviewed and postprocessed using a workstation (Vitrea Fx Workstation, Vital Images). The "vessel probe" software was used, and biperpendicular curved multiplanar reconstruction images were created for all coronary artery segments.

The coronary arteries were divided into 15 segments according to the American Heart Association classification [11]. This included the right coronary artery (segments 1–4), left main artery (segment 5), left anterior descending artery (segments 6–10), and circumflex artery (segments 11–15).

Two radiologists with level 3 American Society of Cardiovascular CT accreditation in cardiac CT evaluated the images on the Vitrea workstation. They were blinded to the patient groups. The images included biperpendicular views of the three coronary arteries and all 15 segments, if present.

No segment was excluded from analysis on the basis of vessel caliber and size, contrast opacification, or presence of calcification. If there was no contrast material visible in the ostium and extending down the length of the expected position of the coronary artery segment, then this segment was deemed to be congenitally absent.

The radiologists graded the quality of the images subjectively at the same time via a consensus approach using a 3-point scoring scale: 1 was defined as excellent quality and diagnostic, 2 was defined as suboptimal quality but still diagnostic, and 3 was defined as poor quality and nondiagnostic. The specific criteria used by the radiologists when judging image quality were overall appearance of the vessel, internal and external wall definition, the degree of motion artifact, the distinction between calcified and noncalcified plaque, and vessel lumen. A diagnostic image free of motion artifact with excellent wall and plaque definition was scored as 1. An image that did not meet these criteria but remained diagnostic was scored as 2. A score of 3 was given to images for which diagnostic assessment was not possible. A specific diagnosis was not required. Discrepancy did not occur because of the consensus reading. Anatomically absent segments were excluded from analysis. Examples of the images evaluated by the radiologists are shown in Figures 1, 2, and 3.

Effective Dose Calculation

The effective dose was calculated in millisieverts for each patient using modified CT dose index volume specific for the Aquilion One unit

(Toshiba Medical Systems). The dose-length product was calculated by multiplying the volume scanned in craniocaudal direction with the CT dose index volume. The estimated effective dose was calculated by multiplying the dose-length product with a conversion factor ($\kappa = 0.014$) [12].

Statistical Analysis

All analyses were performed using SPSS software (version 16, SPSS). Demographic data and effective doses were compared between the two groups of patients using the Mann-Whitney *U* test. Chi-square tests were used to compare the image quality scores between the two groups. Effective dose variability in multibeam acquisition was tested using analysis of variance. Statistical significance was set at *p* value less than 0.05.

Results

Patient Characteristics

The relevant demographic characteristics of patient groups are shown in Table 1. The two patient groups were well matched in terms of age, sex, and BMI ($p > 0.05$). The median heart rate for the group with heart rate greater than 65 beats/min was 70 beats/min (range, 67–110 beats/min), and that for the group with heart rate less than or equal to 65 beats/min was 60 beats/min (range, 48–65 beats/min) ($p < 0.001$). Notably, three patients in the high heart rate group had heart rates greater than or equal to 80 beats/min (80–110 beats/min). Seven patients with heart rates greater than 65 beats/min and two

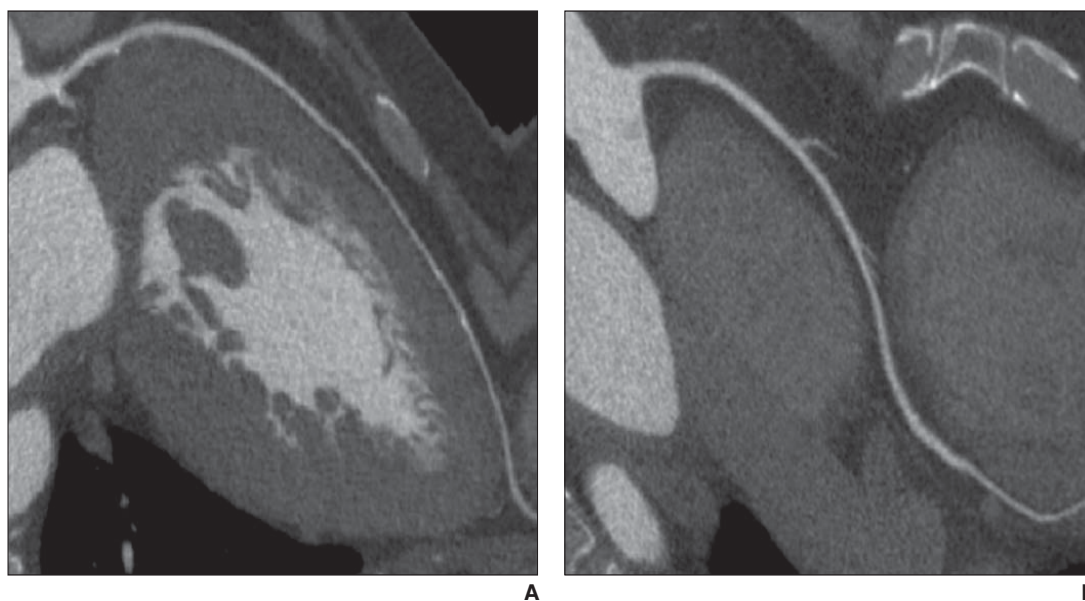


Fig. 1—59-year-old man who was imaged with mean heart rate of 70 beats/min using double-beat retrospective acquisition.

A and B, Images show biperpendicular views of left anterior descending artery (A) and right coronary artery (B). Both arteries were assigned image quality score of 1.

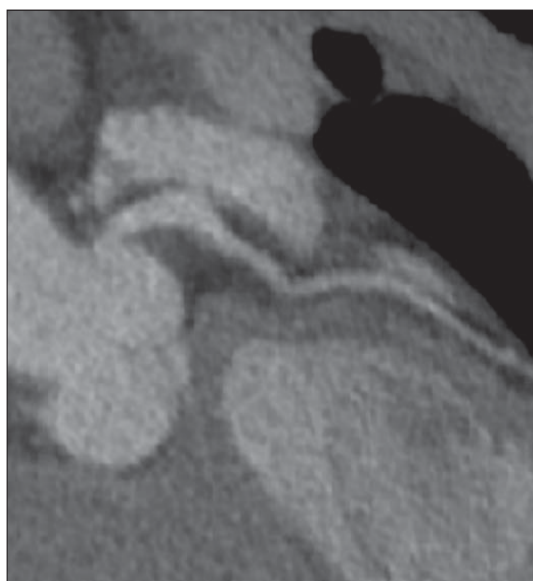


Fig. 2—69-year-old man with heart rate of 60 beats/min who was scanned using double-beat retrospective acquisition. Image shows left circumflex artery, which was given score of 2.

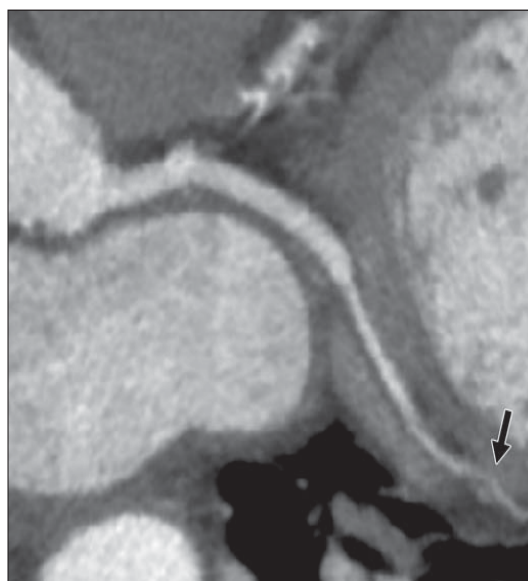


Fig. 3—77-year-old woman with heart rate of 70 beats/min. She was scanned using double-beat retrospective acquisition. Image shows distal circumflex artery (arrow), which was assigned score of 3.

patients with heart rates less than or equal to 65 beats/min were in atrial fibrillation at the time of image acquisition.

In the group of patients with heart rates greater than 65 beats/min, single-, two-, three-, and four-beat acquisitions were acquired in seven, 14, seven, and two patients, respectively. Twenty-four patients (80%) in the control group had a single-beat study, four had two-beat studies, and a single person underwent a three-beat study ($p < 0.001$, subjects vs control group). Heart beat acquisition data were not documented in one patient with heart rate less than or equal to 65 beats/min.

Seven patients with heart rates greater than 65 beats/min underwent prospective scanning, whereas the remaining 23 patients were scanned retrospectively. In the control group, prospective-gated acquisition was performed in 12 patients, and retrospective acquisition was performed in 18 patients ($p = 0.273$).

Image Quality Scores

A total of 900 potential coronary segments were available for analysis (450 in each group, comprising 15 segments/patient; Table 2). Sixty-five segments (38 segments from the heart rate greater than 65 beats/min group and 27 segments from the heart rate less than or equal to 65 beats/min group) were anatomically absent and were, therefore, excluded from analysis, leaving 412 and 423 evaluable segments in the two groups, respectively.

In patients with heart rates greater than 65 beats/min, diagnostic quality images (scores of 1 and 2) were obtained in 95.6% (394/412) of the analyzed segments, compared with 96.9% (410/423) in the group with heart rates less than or equal to 65 beats/min ($p = 0.7$); 92.9% (39/42) of the analyzed segments in the three patients with heart rates greater than or equal to 80 beats/min were of diagnostic quality.

The most common nondiagnostic segment was the distal circumflex artery. These segments accounted for 50% of segments in the group with heart rates greater than 65 beats/min (9/18) and 84.6% in the group with heart rates less than or equal to 65 beats/min (11/13) ($p = 0.04$).

Effective Dose

The median effective dose was 22.40 mSv (range, 3.07–40.32 mSv) for the patient group

with heart rates greater than 65 beats/min and 10.63 mSv (range, 2.96–27.93 mSv) for the group with heart rate less than or equal to 65 beats/min ($p < 0.001$). The median effective dose was significantly higher in the retrospective study than in the prospective study for both groups (Table 3). The effective dose increased with the number of heartbeat acquisitions ($p < 0.001$; Table 4). The effective dose could not be normalized for the z-axis field of view and tube current because those data were not documented for individual patients.

Discussion

To our knowledge, this study is the first evaluation of image quality of coronary artery segments in patients resistant to β -blocker therapy with heart rates greater than 65 beats/min using 320-MDCT. A previous study showed that coronary artery images were diagnostic in nearly 90% of patients

TABLE 1: Demographic Characteristics of Patients Undergoing Coronary 320-MDCT According to Heart Rates

| Characteristic | Heart Rate > 65 Beats/Min ($n = 30/390$) | Heart Rate \leq 65 Beats/Min ($n = 30/390$) | p^a |
|--|--|---|---------|
| Age (y), median (range) | 60.5 (37–87) | 61.0 (37–84) | 0.98 |
| Male (no. of patients) | 12 | 11 | 0.14 |
| Body mass index (kg/m^2), median (range) | 27.3 (20.4–50.7) | 27.5 (21.0–41.9) | 0.86 |
| Heart rate (beats/min), median (range) | 70 (67–110) | 60 (48–65) | < 0.001 |

^aMann-Whitney U test.

320-MDCT in Patients With Elevated Heart Rates

TABLE 2: Image Quality of Coronary Artery Segments According to Heart Rate

| Image Quality Score | Heart Rate > 65 Beats/Min (n = 412 Segments) | Heart Rate ≤ 65 Beats/Min (n = 423 Segments) | p ^a |
|---------------------|---|---|----------------|
| 1 | 339 (82.3) | 376 (88.9) | 0.63 |
| 2 | 55 (13.3) | 34 (8.0) | 0.03 |
| 3 | 18 (4.4) | 13 (3.1) | 0.36 |
| Diagnostic quality | 394 (95.6) | 410 (96.9) | 0.7 |

Note—Data are no. (%) of segments.

^aChi-square test.

TABLE 3: Effective Dose in Prospective Versus Retrospective Gating

| Variable | Heart Rate > 65 Beats/Min ^a | | Heart Rate ≤ 65 Beats/Min ^b | |
|--------------------------------------|--|---------------------|--|--------------------|
| | Prospective | Retrospective | Prospective | Retrospective |
| No. of patients | 7 | 23 | 12 | 18 |
| Effective dose (mSv), median (range) | 7.29 (3.07–36.07) | 22.68 (11.44–40.32) | 5.72 (2.96–9.42) | 13.59 (4.40–27.93) |

^ap < 0.03, Mann-Whitney U test.

^bp < 0.001, Mann-Whitney U test.

TABLE 4: Effective Dose Variability in Multibeam Acquisition

| Variable | Number of Beats per Scan | | | |
|--------------------------------------|--------------------------|--------------------|---------------------|---------------------|
| | 1 | 2 | 3 | 4 |
| No. of patients | 31 | 18 | 8 | 2 |
| Effective dose (mSv), median (range) | 9.42 (2.96–19.17) | 22.58 (9.03–26.28) | 31.25 (21.82–36.07) | 31.97 (23.62–40.32) |

Note—p < 0.001 by analysis of variance test, for all comparisons.

with mean heart rates less than 65 beats/min using 320-MDCT [6]. However, the effect of high heart rate on image quality has not been documented in this setting. Hence, we specifically evaluated the image quality of coronary artery segments in patients with heart rates greater than 65 beats/min using 320-MDCT because this patient group is commonly referred for cardiac evaluation. We have shown that the vast majority (95.6%) of coronary artery images were of diagnostic quality in patients with heart rates greater than 65 beats/min. There was no statistically significant difference in the number of diagnostic images between the groups with heart rate greater than 65 and less than or equal to 65 beats/min. More images of coronary artery segments were given a score of 2 (suboptimal quality but diagnostic) in patients with heart rates greater than 65 beats/min compared with the control group (55/412 [13.3%] and 34/423 [8.0%], respectively; p = 0.03).

The distal circumflex artery was the most common nondiagnostic segment (scored 3) in our analysis. This was mainly the result of

small vessel size in the setting of a dominant right coronary arterial system.

Achieving low heart rate is vital, especially for earlier generation CT scanners, because the temporal resolution needs to be fast enough to produce motion-free images. Significant image degradation was reported at higher heart rates with 4- and 16-MDCT scanners [13, 14]. Temporal resolution may be a limiting factor even with 64-MDCT scanners, whereby higher heart rates have been shown to be independent predictors of insufficient overall image quality [15–17]. The 320-MDCT scanner has a minimum temporal resolution of 175 milliseconds [6]. Other CT units with different acquisition techniques may have shorter temporal resolution, which allows diagnostic imaging with heart rates up to 90 beats/min [18].

The 320-MDCT scanner performs multisegment reconstruction by using data from more than one heartbeat to improve the temporal resolution when scanning patients with high heart rates [5]. Using this method, parts of the projection data from various cardiac cycles are selected and combined for image re-

construction. The result is further improvement in effective temporal resolution, which can be as low as 80 milliseconds if the scanner uses retrospective multibeam acquisition [19]. Furthermore, there was a relatively wide phase window in those patients who underwent prospective ECG gating, allowing additional reconstruction for images with subtle motion artifact. The acquisition and reconstruction technology of 320-MDCT has been used to produce diagnostic motion-free images in most of our patients with heart rates greater than 65 beats/min. The trade-off for multibeam scanning is higher radiation dose to the patients resulting from longer exposure time [5]; 320-MDCT also enables whole heart coverage because of its large field of view (16 cm), thereby eliminating the stair-step, or misregistration, artifact. This artifact may occur as a result of noncontiguous scanning used in a 64-MDCT scanner [6].

When using the ECG-gating technique, the decision to proceed with a single-beat or multibeam study is determined by the operator after recommendation from the scanner software. Preliminary assessment for the mode of acquisition depends on the baseline heart rate during the initial breath-hold test. If the heart rate is less than or equal to 65 beats/min, a single-beat study is planned. A multibeam study is planned for patients with heart rates greater than 65 beats/min. However, scan protocol may change depending on the heart rate and rhythm during image acquisition. A study that was initially planned as a single-beat study may automatically change to a multibeam study if the heart rate speeds up dramatically during the scan. The presence of ectopic beats, arrhythmia, or ECG artifact, even in a patient with heart rate less than or equal to 65 beats/min, will trigger multibeam scanning. Also, a single-beat study may be performed in a patient in sinus rhythm with heart rate slightly above 65 beats/min.

The median effective radiation dose received by patients with heart rates greater than 65 beats/min was 22.40 mSv (range, 3.07–40.32 mSv). The cited radiation dose range in cardiac CT is 3–26.2 mSv [20, 21]. The six patients who received radiation doses greater than 30 mSv underwent three-to-four-beat acquisition studies. The patient who acquired the highest effective dose of 40.32 mSv had a BMI of 50.7 kg/m² and a heart rate of 110 beats/min during a four-beat study. All the images of the coronary artery segments for this patient, except for the posterior descending artery, were

Lee et al.

of diagnostic quality. Two of the patients with high heart rates underwent prospective two-to-three-beat scanning to achieve good temporal resolution. A large number of our patients with high heart rates were also imaged with retrospective multibeat methods for left ventricular functional assessment, which significantly increased their radiation dose.

In comparison, the median effective radiation dose received by the control group was 10.63 mSv. Although many of these patients (18/30 [60%]) also had functional assessment performed, most of the images were acquired using single-beat retrospective gating. The overall effective dose is influenced by the proportion of prospective versus retrospective studies. Prospective gating was shown to have a lower effective radiation dose than retrospective gating, with dose reduction of up to 77% [22, 23]. The disadvantage of using a prospective gating strategy is that cardiac function cannot be assessed.

One of the limitations of this study is its retrospective design. The interest in higher heart rates is grounded in the idea that, if it were possible to scan patients without β -blockade, this would reduce cost, increase scan turn-around time, decrease strain on nursing staff, and avoid the uncommon adverse reaction. Because this study was done retrospectively, the patients in the high heart rate group had experienced the usual interventions designed to reduce their heart rates. This resulted in only a minor difference in heart rates between the control group, at an average of 60 beats/min, and the study group, at 70 beats/min, which will limit the power of this study to detect differences in scan quality related to patients with higher heart rates. Future studies could be performed using larger patient numbers, which would permit a wider range of heart rates to be analyzed, or a regression analysis could be used to assess the trend toward lower image quality at higher heart rates. Because we had only three patients with heart rates greater than or equal to 80 beats/min, it would be of interest to formally assess image quality in this subgroup in a larger cohort.

The use of 320-MDCT is being studied for myocardial perfusion [2]. Other new developments, including vascular profiling and contrast opacification gradients, have used single-beat scanning with 320-MDCT [8, 24]. Further assessment of these novel techniques in the setting of multibeat cardiac CT will need to be considered in light of our study, which confirms the ability of multibeat acquisition

to produce images of high diagnostic quality with high heart rate. To date, our data support work for coronary artery disease assessment alone. There was no direct correlation between our results and catheter angiography. Our study focused on the evaluation of image quality rather than correlation with catheter angiography. Specific assessment of coronary artery disease burden on cardiac CT was not performed, which may have been differing in the two groups and potentially affected our results. Also, there was no standardization in gating acquisition protocols which affected radiation dose delivery to some patients. Various acquisition protocols with lower radiation doses have been proposed [6, 25]. These may be applied in future studies with the specific aim to evaluate radiation dose reduction strategies.

In summary, our initial evaluation suggests that coronary artery images of diagnostic quality can be obtained in patients who are resistant to β -blocker therapy with heart rates greater than 65 beats/min using 320-MDCT. This could be because of the inherent technology of 320-MDCT, where scanning with multibeat acquisition and multisegment reconstruction could be used in this subgroup of patients.

References

- Burgstahler C, Reimann A, Brodoefel H, et al. Quantitative parameters to compare image quality of non-invasive coronary angiography with 16-slice, 64-slice and dual-source computed tomography. *Eur Radiol* 2009; 19:584–590
- Otero HJ, Steigner ML, Rybicki FJ. The “post-64” era of coronary CT angiography: understanding new technology from physical principles. *Radiol Clin North Am* 2009; 47:79–90
- Min JK, Lin FY. What makes a coronary CT angiogram nondiagnostic? *J Cardiovasc Comput Tomogr* 2008; 2:351–359
- Pannu HK, Alvarez W Jr, Fishman EK. β -blockers for cardiac CT: a primer for the radiologist. *AJR* 2006; 186(suppl 3):S341–S345
- Choi SI, George RT, Schuleri KH, Chun EJ, Lima JAC, Lardo AC. Recent developments in wide-detector cardiac computed tomography. *Int J Cardiovasc Imaging* 2009; 25:23–29
- Rybicki FJ, Otero HJ, Steigner ML, et al. Initial evaluation of coronary images from 320-detector row computed tomography. *Int J Cardiovasc Imaging* 2008; 24:535–546
- Pasricha SS, Nandurkar D, Seneviratne SK, et al. Image quality of coronary 320-MDCT in patients with atrial fibrillation: initial experience. *AJR* 2009; 193:1514–1521
- Steigner ML, Mitsouras D, Whitmore AG, et al. Iodinated contrast opacification gradients in normal coronary arteries imaged with prospectively ECG-gated single heart beat 320-detector row computed tomography. *Circ Cardiovasc Imaging* 2010; 3:179–186
- Desjardins B, Kazerooni EA. ECG-gated cardiac CT. *AJR* 2004; 182:993–1010
- Jakobs TF, Becker CR, Ohnesorge B, et al. Multislice helical CT of the heart with retrospective ECG gating: reduction of radiation exposure by ECG-controlled tube current modulation. *Eur Radiol* 2002; 12:1081–1086
- Austen WG, Edwards JE, Frye RL, et al. A reporting system on patients evaluated for coronary artery disease: Report of the Ad Hoc Committee for Grading of Coronary Artery Disease, Council on Cardiovascular Surgery, American Heart Association. *Circulation* 1975; 51(suppl 4):5–40
- Hausleiter J, Meyer T, Herrmann F, et al. Estimated radiation dose associated with cardiac CT angiography. *JAMA* 2009; 301:500–507
- Hoffmann MH, Shi H, Manzke R, et al. Noninvasive coronary angiography with 16-detector row CT: effect of heart rate. *Radiology* 2005; 234:86–97
- Giesler T, Baum U, Ropers D, et al. Noninvasive visualization of coronary arteries using contrast-enhanced multidetector CT: influence of heart rate on image quality and stenosis detection. *AJR* 2002; 179:911–916
- Bamberg F, Abbara S, Schlett CL, et al. Predictors of image quality of coronary computed tomography in the acute care setting of patients with chest pain. *Eur J Radiol* 2010; 74:182–188
- Ferencik M, Nomura CH, Maurovich-Horvat P, et al. Quantitative parameters of image quality in 64-slice computed tomography angiography of the coronary arteries. *Eur J Radiol* 2006; 57:373–379
- Wintersperger BJ, Nikolaou K, von Ziegler F, et al. Image quality, motion artifacts, and reconstruction timing of 64-slice coronary computed tomography angiography with 0.33-second rotation speed. *Invest Radiol* 2006; 41:436–442
- Chinnaiyan KM, McCullough PA, Flohr TG, Wegner JH, Raff GL. Improved noninvasive coronary angiography in morbidly obese patients with dual-source computed tomography. *J Cardiovasc Comput Tomogr* 2009; 3:35–42
- Mahesh M, Cody DD. Physics of cardiac imaging with multiple-row detector CT. *RadioGraphics* 2007; 27:1495–1509
- Wolak A, Gutstein A, Cheng VY, et al. Dual-source coronary computed tomography angiography in patients with atrial fibrillation: initial experience. *J Cardiovasc Comput Tomogr* 2008; 2:172–180
- Mayo JR, Leipsic JA. Radiation dose in cardiac CT. *AJR* 2009; 192:646–653

320-MDCT in Patients With Elevated Heart Rates

22. Shuman WP, Branch KR, May JM, Mitsumori LM, Lockhart DW, Dubinsky TJ. Prospective versus retrospective ECG gating for 64-detector CT of the coronary arteries: comparison of image quality and patient radiation dose. *Radiology* 2008; 248:431-437
23. Earls JP, Berman EL, Urban BA, Curry CA, Lane JL, Jennings RS. Prospectively gated transverse coronary CT angiography versus retrospectively gated helical technique: improved image quality and reduced radiation dose. *Radiology* 2008; 246:742-753
24. Rybicki FJ, Melchionna S, Mitsouras D, et al. Prediction of coronary artery plaque progression and potential rupture from 320-detector row prospectively ECG-gated single heart beat CT angiography: Lattice Boltzmann evaluation of endothelial shear stress. *Int J Cardiovasc Imaging* 2009; 25(suppl 2):289-299
25. Rogalla P, Blobel J, Kandel S, et al. Radiation dose optimisation in dynamic volume CT of the heart: tube current adaptation based on anterior-posterior chest diameter. *Int J Cardiovasc Imaging* 2010; 26:933-940

CHAPTER 2:**COMPARSION OF 4 CM Z-AXIS AND 16 CM Z-AXIS****MULTIDETECTOR CT PERFUSION**

With the establishment that wide field of view CT and volumetric imaging were able to modify previously widely held and universally accepted concepts of limitations in CT imaging, we then considered whether, there were specific areas where volumetric imaging would have significant impact.

Stroke is well recognized [31] as a major cause for both morbidity and mortality world wide. It is also now recognized that the rate of stroke in low and middle income countries is increasing with recent estimates of doubling of stroke rates in Southern India and rural South Africa[32]. With the protocol for advanced imaging for acute stroke in major centres targeting urgent acute intervention[33] and further protocols being investigated in the pre operative arena with NM[34] it is paramount that the ability to yield maximal information from brain perfusion techniques is considered as vital.

We therefore considered the potential for wide field of view CT and the possibilities for greater clinical diagnostic yield when applying the wide field of view to brain perfusion technique. The ability to visualize perfusion anomalies at an improved superior and inferior extent may have significant clinical impact on acute management. That is, the clinical treating team may find significant benefit in recognizing that a perfusion anomaly may either co exist with a perfusion anomaly in the corona radiata, but may also exist as a unifocal abnormality which may, if clinically difficult to localize, not be scanned specifically.

Our team therefore performed a retrospective analysis of the cases performed within the department.

In summary, the work was undertaken to explore whether wide field of view CT would have significant clinical impact in the medical imaging field of stroke imaging and specifically in the area of brain perfusion. We present our results as our second published chapter.

Declaration for Thesis Chapter TWO

Declaration by candidate

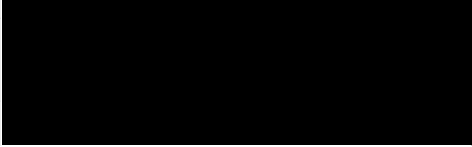
In the case of Chapter Two, the nature and extent of my contribution to the work was the following:

| Nature of contribution | Extent of contribution (%) |
|--|----------------------------|
| Creation of idea, development of structure of the retrospective analysis, creation of the team of researchers, intimately involved with the writing of the paper, guiding the primary author who had very limited experience in this field | 50 |

The following co-authors contributed to the work. If co-authors are students at Monash University, the extent of their contribution in percentage terms must be stated:

| Name | Nature of contribution | Extent of contribution (%) for student co-authors only |
|-------------------|--|--|
| Mark Page | Co ordinated the retrospective analysis and primary authorship | Not a University student |
| Dee Nandurkar | Assisted with review of the images with a consensus approach | Not a University student |
| Marcus P Crossett | Assisted with technical commentary regarding scan acquisitions | Not a University student |

The undersigned hereby certify that the above declaration correctly reflects the nature and extent of the candidate's and co-authors' contributions to this work*.

| | | |
|---------------------------------|---|---------------------|
| Candidate's Signature |  | Date 12 Nov 2013 |
| Head of Department's Signature* |  | Date 12/11/13 |

Mark Page
Dee Nandurkar
Marcus Peter Crossett
Stephen L. Stuckey
Kenneth P. Lau
Nicholas Kenning
John M. Troupis

Comparison of 4 cm Z-axis and 16 cm Z-axis multidetector CT perfusion

Received: 20 June 2009
Revised: 29 September 2009
Accepted: 30 October 2009
Published online: 16 December 2009
© European Society of Radiology 2009

M. Page · D. Nandurkar ·
M. P. Crossett · S. L. Stuckey ·
K. P. Lau · N. Kenning ·
J. M. Troupis (✉)
Department of Diagnostic Imaging,
Southern Health Network,
Monash Medical Centre,
246 Clayton Rd,
Clayton, 3168, Victoria, Australia

Abstract *Objective:* The aim of the study was to compare 4 cm with 16 cm Z-axis coverage in the assessment of brain CT perfusion (CTP) using 320 slice multidetector CT. *Methods:* A retrospective non-randomised review of CTP performed on MD320 CT between September 2008 and January 2009 was undertaken. Two experienced readers reviewed the studies along with the 4 cm and 16 cm Z-axis CTP image data set. The outcome parameters assessed were the extent of the original finding, any additional findings and a change of diagnosis. *Results:* 14 out of 27 patients were found to have abnormal CTP

(mean age 58.1 years, 9 male). The 16 cm Z-axis increased the accuracy of the infarct core in 78% and ischaemic penumbra quantification in 100% of the cases. It also diagnosed additional infarcts in the same vascular territory in 28% of cases and in a different vascular territory in 14%. *Conclusions:* The increased field of view with MD320 better defines the true extent of the infarct core and ischaemic penumbra. It also identified other areas of infarction that were not identified on the 4 cm Z-axis.

Keywords CT · Brain · Infarct · Ischemia · Perfusion

Introduction

CT perfusion (CTP) plays an important role in the acute management of stroke by confirming the diagnosis and providing quantification of infarct core and salvageable penumbra. The main limitation has been a limited imaging volume.

According to the World Health Organization (WHO), stroke is the second single largest killer after coronary artery disease and a leading cause of disability in the world [1]. Prompt diagnosis and treatment has been shown to decrease mortality and morbidity [2]. Neuroimaging plays a vital role in this process. Various imaging techniques have been used for brain perfusion measurement including Xenon-enhanced computed tomography (XeCT), positron emission tomography (PET), single photon emission tomography (SPECT), magnetic resonance imaging (MRI) and computed tomography perfusion (CTP) [3, 4].

Cerebral perfusion defects may be detectable before non-enhanced CT and provide clinicians with a powerful tool for stratification into a diagnosis, management and prognosis stratification. With regard to CTP, slow Mean Transit Time (MTT) has been shown to be the most sensitive for acute ischaemia [4]. Low Cerebral Blood Volume (CBV) is the most specific parameter for infarction [5]. Areas with Cerebral Blood Flow (CBF) and CBV mismatch are defined as penumbra and are possibly salvageable if adequate perfusion is restored [6, 7]. The main advantages of CTP over other imaging techniques are its use in the emergency setting, its application in adults and children, and the provision of Mean Transit Time (MTT), Time to Peak (TTP), Cerebral Blood Flow (CBF) and Cerebral Blood Volume maps (CBV) [3]. These aid in defining the infarct core and the size of the ischaemic penumbra. MTT is defined as the average time taken for blood to pass through a given brain region. TTP is calculated by the peak enhancement of the time-attenuation

curve caused by the contrast bolus. CBF is defined as the volume of blood passing through a brain region in a given time. CBV is defined as the proportion of a given volume of brain that is composed of blood [8].

The limited anatomical coverage of 20–48 mm thickness has been recognised as the traditional disadvantage of CTP with 16 and 64 slice systems. The recent introduction of the “toggling-table” technique with some of the 64 slice CT systems, although allowing increased coverage with non-contiguous slices, is still unable to cover the whole brain [9]. Multiple CT perfusion protocols exist with varying kVp, mAs [10], contrast density [11], image frequency [12, 13], reference vessels, regions of interest and post processing algorithms [14]. kVp of 80, higher contrast density and image frequency of at least one image per 3 seconds have been shown to provide diagnostic image quality with lower radiation dose.

Current CTP protocols with most 16 slice and 64 slice CT enabling a 4 cm field of coverage around the level of the foramen of Monro provides assessment of part of the cortex supplied by the anterior cerebral artery (ACA), middle cerebral artery (MCA) and posterior cerebral artery (PCA). This has been shown to have 95% sensitivity in the detection of supratentorial acute infarction [15]; however, identification of lesions in the superior cerebrum, cerebellum and brain stem is significantly limited because they are outside the field of view. In addition quantification of the size of the infarct and penumbra size is inadequate because of a lack of coverage [16]. The addition of CTA to non-enhanced CT brain (NECT) and CTP has also been shown to increase the accuracy of infarct localisation and the site of vascular occlusion [17]. However, until recently the NECT, CTA and CTP were done as separate examinations leading to longer imaging time and higher radiation dose.

The recent introduction of 320 slice multidetector CT with 16 cm Z-axis coverage addresses the problem of limited anatomical cover by being able to image the entire brain in one rotation [18, 19]. In addition the 320 detector CT system can acquire the NECT, CTA and CTP in a single examination requiring 68 seconds overall. The aim of this study was to compare the 4 and 16 cm Z-axis coverage of CTP in the assessment of cerebral ischaemia.

Materials and methods

Patients

A retrospective systematic audit of all CTP performed on consecutive patients in the clinical setting of cerebral ischaemia or infarct between September 2008 and January 2009 using the MD320 16 cm Z-axis system was undertaken. No patients having a CTP were excluded. All the patients underwent CT within 16 hours of acute

stroke like symptoms such as unilateral paresis or paresis presenting to the emergency department or post neurosurgical intervention complicated by new neurological deficit. All patients were referred by the stroke, neurology and neurosurgery units. Institutional approval was granted.

Imaging

All imaging was performed using 320 Multislice CT (Aquilion One Toshiba medical systems, Tokyo, Japan). Dynamic volume CT was employed comprising multiple volume acquisitions of the entire skull in an axial fashion, i.e. no table movement. The 0.5 mm MD320 detector array enabled 16 cm z-axis coverage. The imaging range covered from below the C1 vertebrae to the skull vertex. Imaging parameters were 80 kVp, 300–350 mA and a gantry rotation of 750 milliseconds. Contrast medium was administered as a biphasic injection using a Stellant Dual chamber contrast injector (Medrad, Warrendale, USA). Phase one consisted of 60 mls of Ultravist 370 (Bayer-Schering pharmaceuticals, Berlin, Germany) and phase two a 50 ml saline flush. Contrast medium was injected at a rate of 5 ml/second. All dynamic volumes were reconstructed to 0.5 mm slices with no interspace gap. All volumes were loaded in to the Toshiba console perfusion package (Toshiba medical systems, Tokyo, Japan). The ICA was manually selected as the arterial baseline. The

Table 1 CTP Comparison between 4 cm Z-axis and 16 cm Z-axis multidetector CT perfusion

| Patient | Number of diagnoses based on 4 cm FOV | Additional diagnostic information based on 16 cm FOV | | New Infarct |
|---------|---------------------------------------|--|-------------------------|-------------|
| | | Infarct size | Ischaemic penumbra size | |
| 1 | 1 | Yes | Yes | Yes |
| 2 | 1 | Yes | Yes | Yes |
| 3 | 1 | Yes | Yes | Yes |
| 4 | 2 | Yes | Yes | Yes |
| 5 | 1 | Yes | Yes | No |
| 6 | 1 | No | Yes | No |
| 7 | 1 | Yes | Yes | No |
| 8 | 2 | Yes | Yes | No |
| 9 | 1 | Yes | Yes | No |
| 10 | 1 | No | Yes | No |
| 11 | 1 | Yes | Yes | No |
| 12 | 1 | Yes | Yes | Yes |
| 13 | 1 | No | Yes | No |
| 14 | 1 | Yes | Yes | Yes |
| Total | 16 | 11 | 14 | 6 |

superior sagittal sinus was manually selected as the venous baseline. Cerebral Blood Flow (CBF), Cerebral Blood Volume (CBV), Mean Transit Time (MTT) and Time To Peak (TTP) perfusion maps were then automatically created. 3D perfusion maps were also imaged as required. Dynamic Angiography MIP 'movies' displaying a cinematic transition through the vascular phases were also generated in AP, Lateral and SI projections.

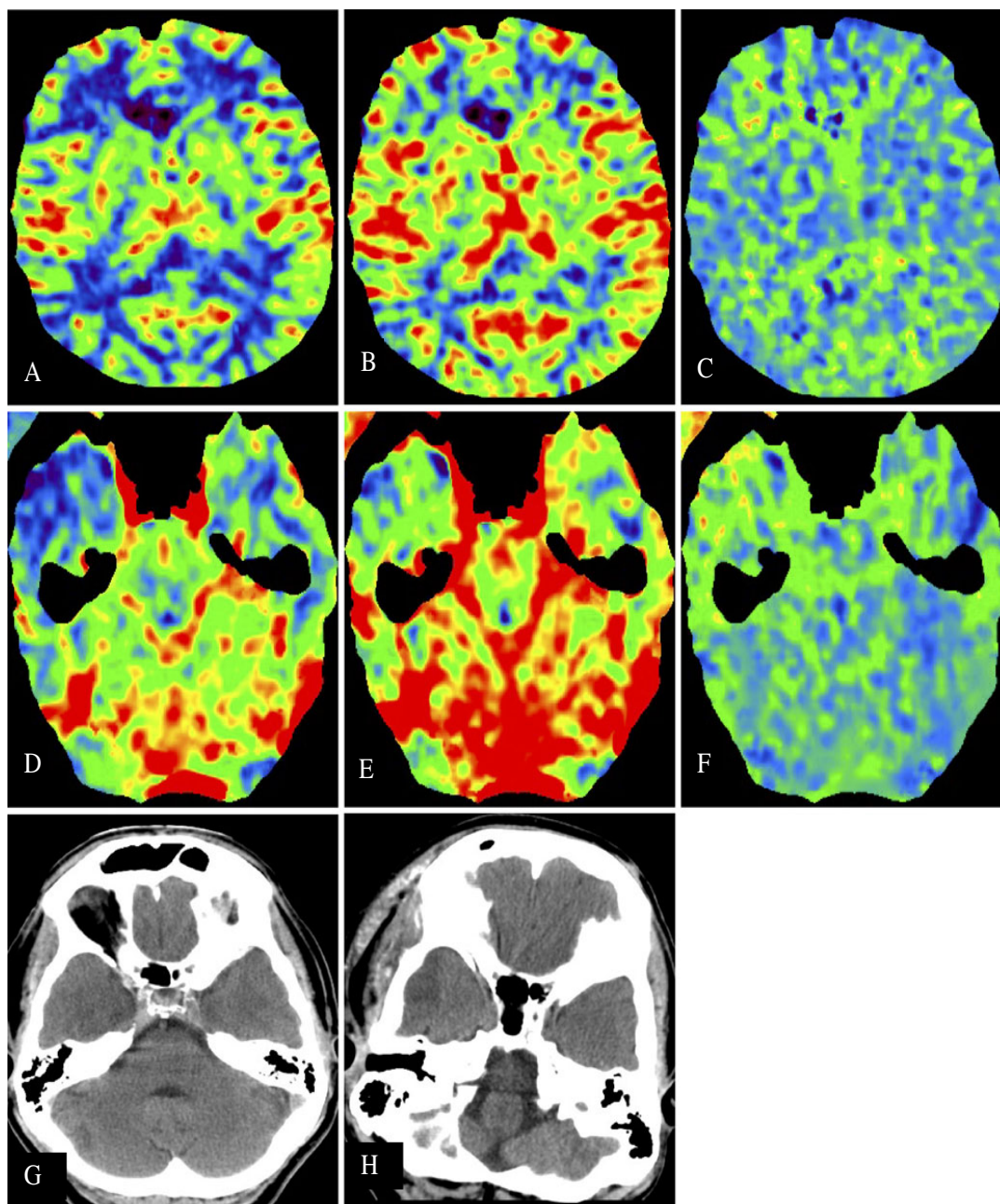


Fig. 1 61-year-old man post-anterior communicating artery aneurysm clipping. CBF, CBV and MTT maps from the 4 cm Z-axis demonstrate an infarct in the anteromedial right frontal lobe. CBF, CBV and MTT maps from a 16 cm Z-axis show an additional infarct in the right temporal lobe. Non-enhanced CT one week before presentation does not show an abnormality in the right temporal lobe

with the follow up CT one week post presentation confirming development of the right temporal infarct. **a-c**, CBF, CBV and MTT at typical section of the 4 cm Z-axis **d-f**, CBF, CBV and MTT using the 16 cm Z-axis **g**, NECT brain one week before presentation **h**, NECT brain one week post-presentation

Image analysis

27 patients were identified. Two experienced readers undertook consensus assessment of the studies using the axial CTP maps. They reviewed the standard 4 cm Z-axis coverage CTP centred around the foramen of Monro reconstructed from the raw data and a diagnosis was assigned. This was followed by review of the 16 cm Z-axis CTP image data set covering the whole brain and a diagnosis was assigned. All results were recorded and analysis was performed with regard to the extent of disease and change of diagnosis. Some of the CTP studies included a CTA, and when available this was also reviewed to aid the diagnosis in both the 4 cm Z-axis and 16 cm Z-axis. Parameters used in the analysis included: change in the craniocaudal size of the initial abnormality detected and new abnormalities detected outside the 4 cm Z-axis.

Results

27 patients who underwent CTP were assessed, (mean age 58.1 years, 9 male, range 32–80) of whom 14 had abnormal CTP. The results are displayed in Table 1. The mean effective radiation dose for CTP was 7.6 mSv (range 7.3–7.9 mSv).

Patients with a normal 4 cm Z-axis CTP did not have any new abnormalities detected on the 16 cm Z-axis CTP. All the 14 patients (100%) with abnormal 4 cm Z-axis had additional diagnostic information based on the 16 cm Z-axis review; this was because of the increased area of ischaemic penumbra (100%) or infarction (78%). 6 (42%) patients had a separate infarction outside the 4 cm Z-axis, of whom 4 patients (28%) had the infarct in the same vascular territory and 2 patients (14%) had an additional

infarct in a separate vascular territory. There was no change in the original diagnosis in any of the patients. No unexpected findings such as neoplasm or vascular malformation were found. The comparison results are provided in Table 1. Sample cases are displayed in Figs. 1, 2, 3 and 4.

Discussion

The 16 cm Z-axis dynamic coverage with 320 slice CT is a considerable improvement upon the options using previous multidetector CT systems. We were able to examine 16 cm along the z-axis in one acquisition. Whole brain CT perfusion was obtained, which not only increased the detection of defects but also altered the severity of perfusion deficits that would not have been detected had the study been undertaken with a 4 cm Z-axis.

Standard 16 or 64 slice CT generally uses ACA or MCA as the reference artery. Partial volume artefact from these small vessels, which do not lie completely in the image plane, reduces the peak intensity and the signal to noise ratio [15]. The MD320 provides the choice of using the arterial and venous reference from the entire imaging volume, allowing the selection of the larger calibre internal carotid artery as the arterial reference rather than the smaller calibre ACA or MCA which are prone to partial volume effect. The largest section of the superior sagittal sinus can be used for the venous reference. These factors increase the accuracy of MTT, CBV and CBF [15]. The ability to acquire the whole brain perfusion in one rotation also increases the accuracy of the MTT, CBV, CBF and TTP measurements because it eliminates the time delay between slices in the “toggling-table” technique [10]. The main advancement of the MD320 compared to its prototype 256-slice predecessor include a larger Z-axis of 16 cm

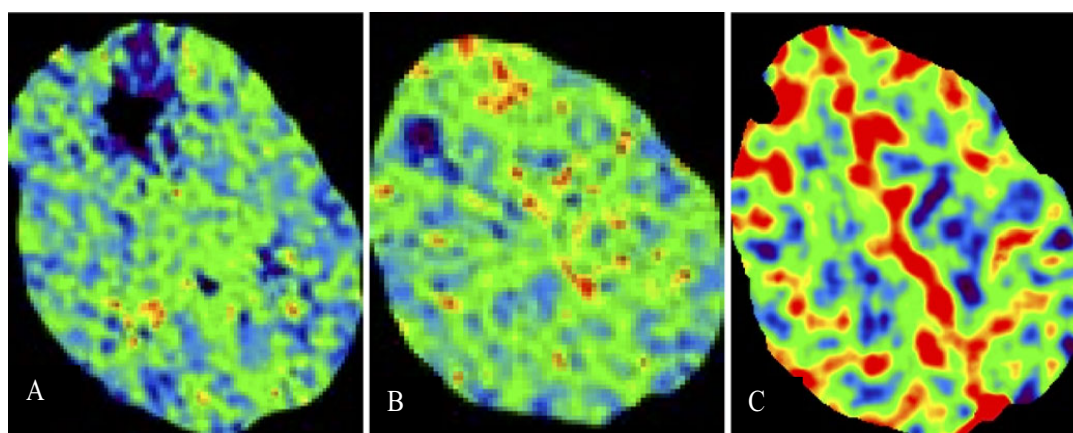


Fig. 2 65-year-old woman with right leg weakness post-pericallosal artery aneurysm clipping. MTT map from the 4 cm Z-axis shows absent MTT in the anterior left frontal lobe. MTT and CBV maps superiorly using a 16 cm Z-axis show an infarct core and large area of penumbra in the superomedial left frontal lobe. **a**, CTP MTT map

from the 4 cm Z-axis shows asymmetrical absent MTT in the anterior left frontal lobe. **b**, CTP MTT map from the 16 cm Z-axis shows increased MTT in the superior left frontal lobe. **c**, CTP CBV map from the 16 cm Z-axis shows decreased CBV in the superior left frontal lobe

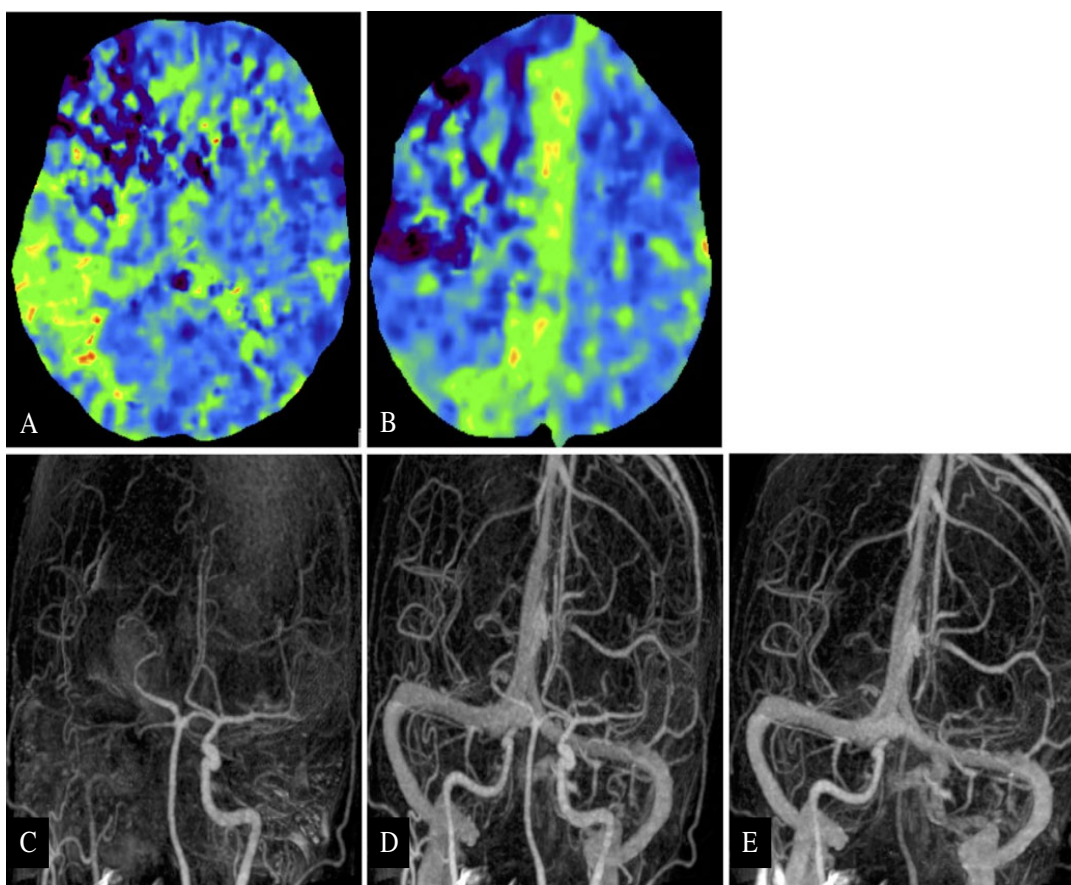


Fig. 3 MTT map from the 4 cm Z-axis shows absent MTT in the right frontal lobe MCA distribution. MTT map from the 16 cm Z-axis shows the increased MTT superiorly in the distribution of the ACA in addition to extension of the MCA distribution abnormality. The dynamic CTA shows contrast opacification of the right ICA with no contrast in the right MCA and ACA. The diagnosis of acute right supraclinoid ICA occlusion was made. In addition the dynamic images showed delayed antegrade opacification of proximal extracranial right ICA which suggested an additional finding of proximal

ICA stenosis. This could not be appreciated on the axial CTA images **a**, 4 cm Z-axis CTP MTT map shows absent MTT time in the right frontal lobe and increased MTT in the right parietal lobe **b**, 16 cm Z-axis CTP MTT map shows absent MTT extending superiorly in the right frontal lobe and increased MTT in the superomedial right frontal lobe. **c-e**, dynamic 16 cm Z-axis CTA shows lack of opacification in the right ICA during the early arterial phase and persistent opacification during the venous phase

vs 12.8 cm. Due to the smaller Z-axis in the 256 prototype, table motion was required for the CTP of the whole brain resulting in some time delay. In addition rotation time improved from 1 second to 750 milliseconds (temporal resolution 375 milliseconds). From a clinical perspective new reconstruction algorithms resulted in faster processing time [19].

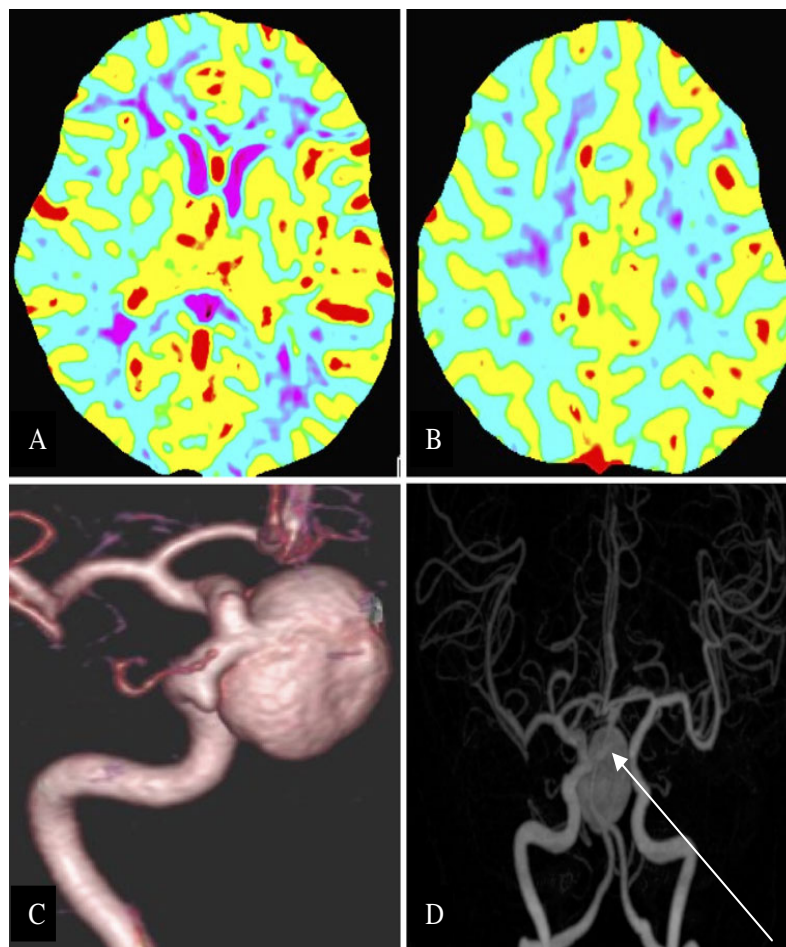
The mean radiation dose of the MD320 NECT, CTP and CTA was 7.6 mSv; this was considerably lower than the equivalent CT examination performed on our department's 64-slice CT system (mean dose 9.59 mSv). The MD320 mean radiation dose was higher than the mean dose using 256-slice CT (4.6 mSv) [19].

Our review showed that all the patients with an abnormal 4 cm Z-axis CTP had additional information either contributing to the original diagnosis or adding a new diagnosis. 28%

had an additional infarct core identified outside the 4 cm Z-axis within the same vascular territory. 14% had an additional infarct core identified outside the 4 cm Z-axis within another vascular territory. In one case a 61 year-old man had a CTP 24 hours after an anterior communicating artery aneurysm clipping for evaluation of vasospasm. The 4 cm Z-axis demonstrated an infarct in the territory of the right ACA. Review of the 16 cm Z-axis demonstrated the large superior extent of the infarct core and ischaemic penumbra. In addition it demonstrated a separate infarct in the right MCA territory.

Another case involving a 47-year-old woman who presented with acute left arm and leg weakness demonstrated the added value of the combination of 16 cm Z-axis CTP with dynamic CTA. 4 cm Z-axis showed a right frontal lobe MCA distribution infarct. 16 cm Z-axis showed superior extension of the MCA distribution infarct

Fig. 4 64-year-old woman with a large right ICA aneurysm. 4 cm Z-axis CBF map shows reduced flow on the right side; the extent of the reduction is further appreciated on the 16 cm Z-axis CBF which shows that the abnormality affected the entire right hemisphere. The dynamic CTA demonstrates contrast streak into the supraclinoid aneurysm originating from the right ICA. **a**, CTP CBF map from the 4 cm Z-axis shows decreased CBF in the right hemisphere consistent with steal phenomena in this case **b**, CTP CBF map from the 16 cm Z-axis shows decreased CBF in the right hemisphere extending superiorly towards the vertex **c**, 3D VR image demonstrates a large right ICA aneurysm **d**, Dynamic CTA image shows contrast plum within the aneurysm originating from the right ICA



with a large area of ischaemic penumbra. In addition a superiorly positioned right paramedian frontal lobe infarct in the ACA distribution was identified. The Dynamic CTA showed contrast opacification of the right ICA with no contrast in the right MCA and ACA. The diagnosis of acute right supraclinoid ICA occlusion was made. In addition the dynamic images showed delayed antegrade opacification of proximal extracranial right ICA which suggested an additional finding of proximal ICA stenosis. This could not be appreciated on the axial CTA images.

Specific assessment of small infarcts in perforator areas was not the aim of the study and was not performed, we expect the identification would be difficult because of limitations in the CTP spatial and contrast resolution. Comparison to MRI DWI would be the gold standard however this was not part of the study design and was not performed. Review of NECT performed for all the 14 patients a week or longer after their CTP did not reveal additional areas of infarction that were not identified on the CTP. This suggests a high negative predictive value.

The whole brain volume acquisition with MD320 also allows simultaneous NECT, CTP and CTA acqui-

sition, which will reduce imaging time and radiation dose. The MD320 perfusion software package allows rapid post-processing time with images made available within 5 minutes of completing CT data acquisition. This provides the clinicians with relevant diagnostic information for patient stratification into an appropriate treatment protocol and can improve patient outcome. Further studies assessing the patient outcomes in acute cerebral ischaemia based on the whole brain CTP coverage are needed [20].

Conclusion

The MD320 provides an increased field of view of 16 cm along the Z-axis allowing whole brain perfusion acquisition. The increased field of view better defined the true extent of the identified infarct core and ischaemic penumbra. It also showed other areas of infarction that were not identified on the 4 cm Z-axis. Further studies are required to assess the implications for stroke diagnosis and treatment outcome.

References

- World Health Organization. The top ten causes of death. Available via WHO www.who.int/mediacentre/factsheets/fs310/en/index.html. Accessed 6 Apr 2009
- National Institute of Neurological Diseases and Stroke rt-PA Stroke Study Group (1995) Tissue plasminogen activator for acute ischemic stroke. *N Engl J Med* 333:1581–1587
- Wintermark M, Sesay M, Barbier E et al (2005) Comparative overview of brain perfusion imaging techniques. *Stroke* 36:e83–e99
- Latchaw RE, Yonas H, Hunter GJ et al (2003) Guidelines and recommendations for perfusion imaging in cerebral ischemia. *Stroke* 34:1084–1104
- Silvernoinen HM, Hamberg LM, Lindberg PJ et al (2008) CT Perfusion identifies increased salvage of tissue in patients receiving intravenous recombinant tissue plasminogen activator within 3 hours of stroke onset. *AJNR Am J Neuroradiol* 29:1118–1123
- Hoeffner EG, Case I, Jain R et al (2004) Cerebral perfusion CT: technique and clinical applications. *Radiology* 231:632–644
- Konig K (2007) Diagnosis of acute stroke. In: Miles KA, Eastwood JD, Konig M (eds) Multidetector computed tomography in cerebrovascular disease, CT perfusion imaging. Informa Healthcare Ltd, Milton Park, pp 83–97
- Miles KA, Menon DK (2007) Cerebrovascular physiology and pathophysiology. In: Miles KA, Eastwood JD, Konig M (eds) Multidetector computed tomography in cerebrovascular disease, CT perfusion imaging. Informa Healthcare, Milton Park, pp 71–82
- Roberts HC, Roberts PL, Wade SS et al (2001) Multisection dynamic CT perfusion for acute cerebral ischemia: the “toggling-table” technique. *AJNR Am J Neuroradiol* 22:1077–1080
- Wintermark M, Maeder P, Verdun FR et al (2000) Using 80 kVp versus 120 kVp in perfusion CT measurement of regional cerebral blood flow. *AJNR Am J Neuroradiol* 21:1881–1884
- Konig M, Bultmann E, Bode-Schnurbus L et al (2007) Image quality in CT perfusion imaging of the brain, the role of iodine concentration. *Eur Radiol* 17:39–47
- Wiesmann M, Berg S, Bohner G et al (2008) Dose reduction in dynamic perfusion CT of the brain: effects of the scan frequency on measurements of cerebral blood flow. Cerebral blood volume and mean transit time. *Eur Radiol* 18:2967–2974
- Wintermark M, Smith WS, Nerissa U et al (2004) Dynamic perfusion CT: optimizing the temporal resolution and contrast volume calculation of perfusion CT parameters in stroke patients. *AJNR Am J Neuroradiol* 25:720–729
- Soustiel JF, Mor N, Zaaroor M et al (2006) Cerebral perfusion computerized tomography: influence of reference vessels, regions of interest and interobserver variability. *Neuroradiology* 48:670–677
- Wintermark M, Fischbein NJ, Smith WS et al (2005) Accuracy of dynamic perfusion CT with deconvolution in detecting acute hemispheric stroke. *AJNR Am J Neuroradiol* 26:104–112
- Eastwood JD, Lev MH, Wintermark M et al (2003) Correlation of early dynamic CT perfusion imaging with whole-brain MR diffusion and perfusion imaging in acute hemispheric stroke. *AJNR Am J Neuroradiol* 24:1869–1875
- Ezzeddine MA, Lev MH, McDonald CT et al (2002) CT angiography with whole brain perfused blood volume imaging: added clinical value in the assessment of acute stroke. *Stroke* 33:959–966
- Klingebl R, Siebert E, Diekmann S et al (2009) 4-D Imaging in cerebrovascular disorders by using 320-slice CT: feasibility and preliminary clinical experience. *Acad Radiol* 16:123–129
- Mori S, Obata T, Nakajima N et al (2005) Volumetric perfusion CT using prototype 256-detector row CT scanner: preliminary study with healthy porcine model. *AJNR Am J Neuroradiol* 26:2536–2541
- Provenzale JM, Shah K, Patel U et al (2008) Systemic review of CT and MR perfusion imaging for assessment of acute cerebrovascular disease. *AJNR Am J Neuroradiol* 29:1476–1482

CHAPTER 3:

NORMAL PERFUSION OF THE LEFT VENTRICULAR MYOCARDIUM

USING 320 MDCT

With the introduction of 64 slice multidetector CT units, which achieved isometric imaging, high resolution imaging was possible up to less than 1mm in resolution. This allowed the subsequent development and utilization of advanced post processing techniques, allowing assessment of tissues in a multiplanar format. Significant advances in vascular assessment were therefore possible. However, whilst spatial anatomical resolution attained this advent, the issue of tissue function was only just beginning.

Tissue function can be secondarily assessed when administering iodinated contrast agents intravenously; the technique is referred to as perfusion. Brain perfusion has gained acceptance and is currently being implemented in routine protocols. However brain perfusion assessment has traditionally been evaluated in the non emergent setting with both NM [35] and MRI[36, 37] with CT being utilized in the emergent setting[38].

Although myocardial tissue may be subject to ischaemia secondary to obstructive coronary artery disease, a fundamental issue is to be able to determine whether the myocardium is subject to functional impairment. The assessment of myocardial perfusion has traditionally been investigated with NM[39-41] and cardiac MRI[42, 43].

However, with the introduction of high diagnostic quality CT imaging of the heart, myocardial perfusion assessment with CT has been of significant interest. CT offers a significant valuable alternative for the diagnosis of coronary artery disease but its value in determination the level of functional obstruction of the relevant coronary stenosis remains uncertain with some provisional research proposing that an abnormal CT of the coronary arteries remains a poor predictor of ischaemia[44, 45].

As wide field of view CT is a relatively new introduction into myocardial perfusion, our next paper intends to establish a baseline of myocardial density assessment. In particular, we aim to establish baseline density measurements of the myocardium in a cohort of patients with

normal coronary arteries, in order to form a foundation from which to better define density variations in those patients with obstructive coronary artery disease.

Our next chapter establishes the CT densities, in Hounsfield Units, of the myocardial segments, in a cohort of patients with normal coronary arteries, in the wide field of view CT scan.

Declaration for Thesis Chapter THREE

Declaration by candidate

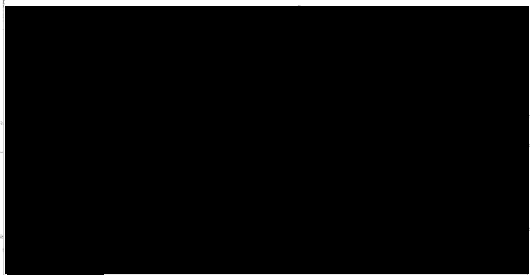
In the case of Chapter Three, the nature and extent of my contribution to the work was the following:

| Nature of contribution | Extent of contribution (%) |
|--|----------------------------|
| Creation of idea, development of structure of the retrospective analysis, creation of the team of researchers, intimately involved with the writing of the paper, guiding the primary author who had very limited experience in this field | 50 |

The following co-authors contributed to the work. If co-authors are students at Monash University, the extent of their contribution in percentage terms must be stated:

| Name | Nature of contribution | Extent of contribution (%) for student co-authors only |
|-------------------------|--|--|
| Marcus P Crossett | Co ordination of analysis of images and primary authorship | Not a University student |
| Michal Schneider-Kolsky | Statistical analysis, proof reading | Not a University student |
| | | |

The undersigned hereby certify that the above declaration correctly reflects the nature and extent of the candidate's and co-authors' contributions to this work*.

| | | |
|---------------------------------|--|---------------------|
| Candidate's Signature |  | Date 12 Nov 2013 |
| Head of Department's Signature* |  | Date 12/11/13 |

Original Research Article

Normal perfusion of the left ventricular myocardium using 320 MDCT

Marcus Peter Crossett, BAppPh^{a,*}, Mical Schneider-Kolsky, PhD^b,
John Troupis, MBBS^a

^aDepartment of Diagnostic Imaging, Monash Medical Centre, Southern Health, 246 Clayton Road, Clayton, Victoria 3168, Australia and ^bDepartment of Medical Imaging & Radiation Sciences, Faculty of Medicine, Nursing and Health Sciences, Monash University, Melbourne, Australia

KEYWORDS:

Myocardium;
Perfusion;
Density;
Computed tomography

BACKGROUND: CT myocardial perfusion imaging is an emerging CT application using density measurements of contrast-enhanced left ventricular (LV) myocardium.

OBJECTIVE: Using a 320-MDCT we have consistently observed lower Hounsfield unit (HU) values in the lateral LV myocardium, potentially mimicking perfusion defects. This study aimed to evaluate contrast-enhancement patterns of the LV myocardium in normal studies.

METHODS: Twenty-one clinical cases with normal coronary MDCT-based angiography findings, as determined by 2 qualified readers, were selected for retrospective evaluation. Using 8 identically sized and positioned ROIs, the HU measurements were recorded from short axis axial reconstructions through the LV myocardium in middle, apical, and basal locations. Scans were acquired on a 320-slice MDCT unit.

RESULTS: The middle short axis location demonstrated HU densities of 79.4 (range 42.3–162.7) in the lateral myocardial wall (regions 2, 3, and 4) compared with 103.9 (range 11.4–159.6) in the inferior, septal, and anterior walls (regions 1, 5, 6, 7, and 8; $P < 0.001$). HU densities for the basal slice were 82.3 (range 51.5–168.4) in the lateral wall compared with 94.9 (range 35.3–144) in the inferior, septal, and anterior walls ($P < 0.001$). In the apical location, HU densities were 79.9 (range 42.3–139.3) in the lateral wall compared with 100.9 (range 69.0–170.5) in the inferior, septal, and anterior walls ($P < 0.001$).

CONCLUSION: Normal LV myocardial enhancement using a 320-slice MDCT demonstrates significantly lower densities in the lateral wall when compared with the anterior, septal, and inferior walls in patients with normal coronary vascular anatomy. Assessment of CT myocardial perfusion studies should therefore be undertaken with caution, to prevent misrepresenting these lower-density values in the LV lateral wall.

Crown Copyright © 2011 Published by Elsevier Inc on behalf of Society of Cardiovascular Computed Tomography. All rights reserved.

Introduction

Multiple studies have shown that noninvasive coronary computed tomography angiography (CTA) has a high negative predictive value in the detection of coronary artery disease when compared with conventional invasive angiography.^{1–3} Similar to conventional angiography, however, the analysis of any obstructive disease using this purely anatomical method

Conflict of interest: The authors report no conflicts of interest.

* Corresponding author.

E-mail address: [REDACTED]

Submitted August 12, 2011. Accepted for publication October 19, 2011.

has proven unreliable in predicting functional significance.⁴ Furthermore, obstructive disease identified by coronary CTA is not a good predictor of reversible ischemia.^{5,6}

The revascularization of reversible ischemia caused by obstructive coronary disease has been shown to improve clinical outcomes,^{7,8} whereas medical therapy appears equally successful in the treatment of nonfunctionally significant coronary disease.⁹ Therefore, functional imaging combined with invasive or noninvasive anatomical assessment is desirable in the assessment of coronary artery disease to determine appropriate treatment.

CT myocardial perfusion imaging using a pharmacological stress agent such as adenosine is a growing application that uses multidetector CT (MDCT) to demonstrate both anatomical and functional information within the one examination. Initial studies have shown a good correlation with quantitative coronary angiography combined with single-photon emission CT imaging in determining obstructive disease and subsequent reversible ischemia.^{10,11}

MDCT perfusion techniques have been evolving over the past few years, although arguably it may be said that myocardial perfusion studies are still a work in progress. Current image analysis methods use either thin multiplanar reconstructions (MPRs), thick MPRs, and minimum intensity projections of the left ventricular (LV) myocardium to highlight areas of reduced contrast enhancement compared with normal myocardium.¹² Another method uses a transmural perfusion ratio, which compares the Hounsfield unit (HU) densities of the subendomyocardial regions with those in the subepimyocardium.¹⁰ All of these methods rely on an accurate assessment of the contrast media perfusion in the myocardium through HU measurements. This attenuation-based assessment can be adversely affected by a number of artifacts, including beam hardening, which have been documented in previous studies.^{13,14} One such study examined normal myocardial perfusion using 64-detector row CT¹⁵ and noted significantly higher attenuation values in the LV myocardium septum compared with values measured in the lateral and inferior myocardial wall regions, which were found to be similar. In our institution, using a 320-detector row CT, we have also observed nonuniform attenuation values in the LV myocardium, even in cases where the presence of coronary disease was not demonstrated.

We therefore designed this study with the aim to identify different attenuation patterns of the contrast-enhanced LV myocardium in patients with no detectable coronary artery disease using a 320-detector row CT scanner.

Methods

Study design

All patients referred to our institution for coronary CTA, and who present with nonacute chest pain, routinely undergo a prospectively gated study using a 320-detector

row CT (Aquilion ONE, Toshiba Medical Systems, Nasu, Japan). Following institutional approval, cases performed over 14 days were evaluated by 2 qualified readers (American Society of Cardiovascular CT Level 3) using the following exclusion criteria: the presence of any coronary artery disease including calcified or noncalcified plaques; coronary anomalies, such as congenital heart disease; cardiomyopathy; cardiac motion; and suboptimal image signal to noise. The 21 cases that were not excluded using these criteria were therefore used for this retrospective study.

Patient preparation

Patient preparation involved heart-rate control using oral metoprolol (if not contraindicated) where the patient's heart rate was above 60 beats per minute. Where the heart rate was between 60 and 70 beats per minute, an oral dose of 50 mg was administered 1 hour before the scan. An oral dose of 100 mg of metoprolol was used for heart rates above 70 beats per minute. This routine was followed despite the scanner's software programming, which performs a single-beat single-sector acquisition at a heart rate of less than 65 beats per minute. The reason for implementing metoprolol therapy in those at the lower end of tolerance was to reduce the likelihood of a rise in heart rate during contrast administration and breath-hold, and the subsequent acquisition of a multibeat study resulting in a higher ionizing radiation burden. If the heart rate was found to be above 65 beats per minute at the time of the scan, intravenous metoprolol was administered in 5-mg boluses up to 30 mg until a heart rate of 60 beats per minute was achieved.

Immediately before the scan, a 40- μ g oral dose of nitrate spray was delivered sublingually. A biphasic contrast injection protocol was used. The initial phase consisted of 75 mL of iohexal 56.6 g/75 mL (Omnipaque 350) at 6 mL per second followed by a secondary phase of 50 mL of normal saline at the same injection rate. Automatic bolus tracking was used to trigger the image acquisition, with the region of interest (ROI) placed in the descending aorta and the scan triggered once the density value reached 300 HU.

Scan technique

The 320-row scanner is unique, as it uses a 320 \times 0.5-mm detector row, providing up to 16 cm of z-axis coverage in a single tube rotation, enough to capture the entire heart. The scan range for the cardiac CTA covered from the inferior carina to immediately below the heart base. Where possible (ie, where the heart size permitted), the number of detector rows used was reduced to 280 or 240 to reduce the radiation dose to the patient. A tube rotation speed of 350 ms was used with a tube potential of 100 kV for patients with a body mass index (BMI) of less than 23 kg/m², 120 kV for BMIs between 23 and 39 kg/m², and 135 kV for patients with a BMI higher than 40 kg/m². A tube current of between 400 to 580 mA was used, also depending on patient BMI. Prospective gating was



Figure 1 Horizontal long-axis slice demonstrating the basal, mid, and apical slice positions used for the density measurements.

used with a modest widened acquisition window providing the opportunity for reconstructed phases between 70% and 80% of the R-to-R interval. Where the heart rate remained below 65 beats per minute during the acquisition, the study was completed within a single heartbeat. Where the heart rate increased to more than 65 beats per minute, or an ectopic beat was encountered, a multisector acquisition was initiated by the scanner's arrhythmia rejection software.

The scan data were automatically reconstructed at the 75% R-to-R phase using 0.5-mm slices overlapping every 0.25 mm using a cardiac algorithm (FC03) developed to reduce beam-hardening artifacts within the LV myocardium primarily caused by the contrast-enhanced LV and descending aorta.¹³

Where cardiac motion was detected in the initial data set, additional phases were reconstructed. Clinical evaluation, including image analysis and postprocessing, were performed using a Vitrea FX Workstation (Vital Images, Minnetonka, MN). All myocardial density ROI measurements, however, were performed using the MDCT scanner's console software.

Image analysis

To measure the left myocardial density values, 5-mm-thick contiguous MPR slices were generated covering the entire LV myocardium in the short axis. The middle slice was selected and labeled as the "mid" slice. A slice 20 mm toward the apex was labeled "apex" and another, 20 mm toward the base, was labeled "base," as shown in Figure 1.

Eight identically sized rectangular ROIs were symmetrically positioned within the LV myocardium for the 3 designated short-axis MPRs, in identical spatial locations for each slice, as shown in Figure 2. The locations of the

ROI measurements did not follow the American Heart Association 17-segment model of myocardial segments. Instead, more frequent samples of the myocardium were performed (a total of 24 ROIs compared with 17 myocardial segments) owing to our assumption of significant variation in myocardial density, which would likely not conform to the traditional 17 segments. We therefore increased the number of sampled regions to more accurately assess the range of LV densities, while at the same time keeping the ROI large enough to maintain adequate signal to noise.

Statistical analyses

All values presented are the mean \pm standard deviation for continuous variables. One observer collected all HU densities using a 24-ROI template under the supervision of an accredited cardiac CT radiologist (American Society of Cardiovascular CT Level 3). HU measurements were recorded for each ROI positioned in the basal, mid, and apical slice locations. Median HU densities were compared between the lateral (regions 2, 3, and 4) and the inferoseptal regions (regions 1, 5–8) and compared using Mann-Whitney *U* tests (SPSS, V 16, Chicago, IL). A *P* value of < 0.05 was defined as statistically significant.

Results

A total of 21 patients (54 ± 10 years, 13 men and 18 women) who had no cardiac disease were included for investigation of HU densities. Baseline characteristics for the study participants, including cardiac risk factors are described in Table 1.

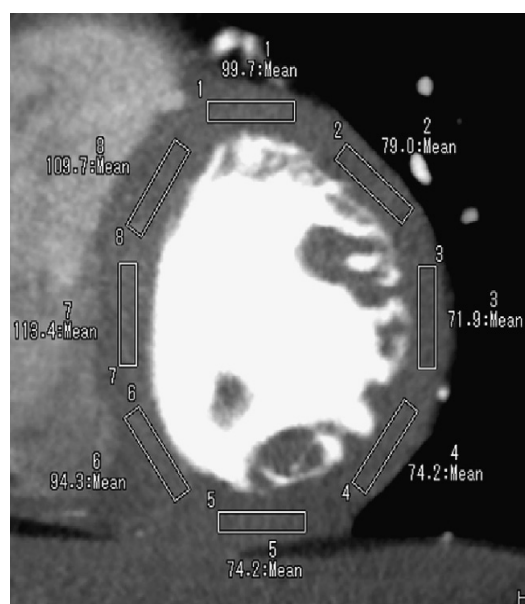


Figure 2 Short-axis slice demonstrating the ROI locations and associated wall densities within the LV myocardium.

Table 1 Demographics for the patients undergoing coronary CT angiography using 320 MDCT

| | n/N |
|---|----------|
| Number | 21 |
| Age, y | 54 ± 10 |
| Male/Female | 13/18 |
| Height, cm | 170 ± 10 |
| Weight, kg | 77 ± 11 |
| Body mass index, kg/m ² | 27 ± 5 |
| Hypertension | 11/21 |
| Non-insulin-dependent diabetes mellitus | 1/21 |
| Current/previous smoker | 3/21 |
| Hypercholesterolemia | 5/21 |

Values shown are mean ± standard deviation.

HU densities (median, ranges) for the ROIs located in the lateral myocardial wall positions (2, 3, and 4) demonstrated significantly lower HU densities when compared with the septal and inferior wall locations, in the basal, mid, and apical slice locations. The middle short-axis location demonstrated HU densities of 79.4 (range 42.3–162.7) in the lateral myocardial wall (regions 2, 3, 4) compared with 103.9 (range 11.4–159.6) in the inferior, septal, and anterior walls (regions 1, 5, 6, 7, 8; $P < 0.001$). HU densities for the basal slice (base) were 82.3 (range 51.5–168.4) in the lateral wall compared with 94.9 (range 35.3–144) in the inferior, septal, and anterior walls ($P < 0.001$). In the apical location, HU densities were 79.9 (range 42.3–139.3) in the lateral wall compared with 100.9 (range 69–170.5) in the inferior, septal, and anterior walls ($P < 0.001$). These results are shown in Table 2.

All 8 individual ROIs within the LV myocardium in the basal, mid, and apical slice locations were compared. Results show that ROI 3, located in the lateral myocardial wall, measured the lowest HU density in each of the 3 axial slice locations. ROI 7, located in the septal wall, measured the highest density in the basal and mid slice locations, whereas ROI 8, located in the anteroseptal wall, measured the highest HU density in the apical slice. Results are shown in Table 3.

Table 2 Comparison of computed tomography attenuation values for lateral myocardial regions (2,3, and 4) and inferoseptal myocardial regions (1, 5–8), (median, ranges)

| | Location 2, 3, and 4 (lateral) | Location 1, 5–8 (septo-basal) | P^* |
|------|--------------------------------|-------------------------------|---------|
| Base | 82.3 (51.5–168.4) | 94.9 (35.3–144) | < 0.001 |
| Mid | 79.4 (42.3–162.7) | 103.9 (11.4–159.6) | < 0.001 |
| Apex | 79.9 (42.3–139.3) | 100.9 (69–170.5) | < 0.001 |

*Mann-Whitney U test.

Table 3 Computed tomography attenuation values of the left ventricular myocardium for all region of interest locations in the basal, mid, and apical slices (median, ranges)

| Location | Region of interest location | Wall density, median (ranges) |
|----------|-----------------------------|-------------------------------|
| Base | 1 Anterior | 88.8 (49.1–141.1) |
| | 2 Anterolateral | 80.4 (51.5–141.5) |
| | 3 Lateral | 80.2 (54.1–168.4) |
| | 4 Inferolateral | 85.4 (60.8–137.8) |
| | 5 Inferior | 87.3 (35.3–133.9) |
| | 6 Inferoseptal | 101.1 (69.5–139.1) |
| | 7 Septal | 112.0 (77.9–144.0) |
| | 8 Anteroseptal | 95.7 (54.4–134.1) |
| Mid | 1 Anterior | 93.1 (60.1–151.0) |
| | 2 Anterolateral | 81.0 (55.9–161.8) |
| | 3 Lateral | 70.8 (42.3–162.7) |
| | 4 Inferolateral | 79.7 (61.7–119.7) |
| | 5 Inferior | 99.9 (77.0–152.3) |
| | 6 Inferoseptal | 99.6 (80.2–159.6) |
| | 7 Septal | 109.9 (11.4–152.8) |
| | 8 Anteroseptal | 107.2 (75.7–156.6) |
| Apex | 1 Anterior | 98.9 (73.9–148.0) |
| | 2 Anterolateral | 87.6 (56.1–139.3) |
| | 3 Lateral | 73.4 (42.3–134.9) |
| | 4 Inferolateral | 82.2 (67.4–127.4) |
| | 5 Inferior | 102.2 (78.8–159.2) |
| | 6 Inferoseptal | 100.4 (69.5–149.3) |
| | 7 Septal | 98.9 (69.0–170.5) |
| | 8 Anteroseptal | 103.4 (75.1–167.4) |

Discussion

Our results demonstrate a consistent pattern of reduced HU density within the lateral LV myocardial wall in all short-axis slice locations. More specifically, the average HU density for ROI 3 located in the lateral myocardial wall in the mid short-axis slice was only 70.8 HUs, compared with 109.9 HUs in ROI 7 located in the septal wall, representing a difference of 39.1 HUs. This differential may be of sufficient magnitude to affect the accuracy of MDCT myocardial perfusion imaging, where the recognition of small differences in HU densities between ischemic myocardium and normally perfused myocardium is crucial. Furthermore, failure to appreciate the potential for lower density regions within the lateral myocardium, even within normal cases, could result in false-positive conclusions. Our results demonstrate that the patterns of HU densities within the LV myocardium are not consistent throughout the entire myocardium, even in cases without identified coronary artery disease.

The reasons for an inconsistent HU density pattern are most likely complex. Dense structures adjacent to the

inferior and septal myocardium, such as the diaphragm and right heart, contribute to an increase in HU density owing to beam-hardening effects, whereas the lateral myocardial wall, typically located adjacent to air within the lung, is not subject to similar beam-hardening effects as those myocardial areas adjacent to more dense thoracic structures. Additionally, cone beam artifacts, owing to the wide fan beam angle used by the 320-detector row CT, should also be considered given the inferior LV wall was typically positioned toward the inferior edge of the detector row in the z direction. This region demonstrated higher HU densities when compared with the lateral LV wall, which was typically located in the center of the detector row.

A number of limitations exist in our study. First, density measurements of the myocardium were performed only by placing ROIs in the center of the myocardial wall, and therefore specific measurements of the subepicardial, midmyocardial, and subendocardial layers were not performed. Pathological processes, such as ischemia, infiltration, endothelial dysfunction, and inflammation, which may target specific areas or layers within the myocardium, have therefore not been taken into account in our study. Second, no correlation with functional imaging, such as myocardial perfusion imaging or echocardiography was able to be performed. These results may have demonstrated a perfusion defect or functional abnormality owing to nonischemic causes, despite the absence of MDCT-evident coronary artery disease. Furthermore, our study used coronary CTA to determine the absence of occlusive coronary artery disease and not the gold standard of catheter-based angiography; however, we believe this was a reasonable part of our study design owing to the recognized high negative predictive value of coronary CTA for the detection of coronary artery disease generally.

Coronary CTA using a 320-row detector system is a static acquisition where the examination is performed in single phase of contrast perfusion from as little as a fraction of 1 heartbeat. The study, therefore, does not account for possible normal changes or variations in myocardial perfusion over time. It is possible that MDCT-based LV myocardium perfusion may demonstrate a different pattern of enhancement at an earlier or later acquisition time after contrast media administration; however, this was not performed, because to collect such data would involve a substantial increase in the patient's radiation exposure, as it would involve multiple electrocardiogram-gated acquisitions covering the entire heart. Our study included data using a limited range of cardiac phases, typically between 70% and 80% of the R-to-R cycle, and all within the same heartbeat. This variation in cardiac phase was necessary to produce a diagnostic study with no coronary artery or myocardial motion; however, phases outside those described were not evaluated, as they demonstrated artifacts within the myocardium owing to cardiac motion. Data recorded from such phases could potentially result in inaccurate density measurements of the myocardium where

areas of dense contrast from the enhanced LV blood pool, or air from the lung, blur together with the myocardium to cause false density values. The effects of beta-blockade medication on coronary macrovascular or microvascular blood flow within the myocardium, affecting contrast perfusion, may also be a limitation. Our findings, however, are still noteworthy, as the use of metoprolol has been described for the purpose of heart rate control in CT myocardial perfusion imaging.¹⁶

Despite these limitations, our study demonstrates a pattern of lower HU densities within the lateral LV myocardial wall, which was replicated in all axial-slice locations and in all patients. Further research into the cause and potential solution to this varied attenuation pattern is therefore required. An identical study to examine HU density patterns of the LV myocardium in MDCT perfusion using other MDCT detector rows (ie, 128 detector row), including dual-source units, is also required to further quantify this effect in terms of beam hardening and the effect of various reconstruction algorithms. In addition, examining the effects of variations in scan parameters, such as acquisition slice width, beam pitch, and reconstruction algorithms, may also be warranted.

Conclusion

In healthy patients, where coronary artery disease is not identified on coronary CTA, LV myocardial enhancement using a 320-MDCT protocol demonstrated significantly lower HU densities in the lateral wall when compared with the anterior, septal, and inferior wall regions in apical, mid, and basal short-axis locations. Assessment of the LV myocardium using HU perfusion studies should therefore be undertaken with caution to prevent misrepresenting the lower HU density values in the LV lateral wall as necessarily indicating disease status. Further research into the cause of this nonuniform myocardial density pattern would be of great clinical value, but must include a similar assessment of other MDCT and allied technologies currently used for perfusion studies of the LV myocardium.

References

1. Budoff MJ, Dowe D, Jollis JG, Gitter M, Sutherland J, Halamert E, Scherer M, Bellinger R, Martin A, Benton R, Delago A, Min JK: Diagnostic performance of 64-multidetector row coronary computed tomographic angiography for evaluation of coronary artery stenosis in individuals without known coronary artery disease: results from the prospective multicenter ACCURACY (Assessment by Coronary Computed Tomographic Angiography of Individuals Undergoing Invasive Coronary Angiography) trial. *J Am Coll Cardiol*. 2008;52:1724-32.
2. Scheffel H, Alkadhi H, Plass A, Vachenaer R, Desbiolles L, Gaemperli O, Schepis T, Frauenfelder T, Schertler T, Husmann L, Grunenfelder J, Genoni M, Kaufmann PA, Marinck B, Leschka S: Accuracy of dual-source CT coronary angiography: first experience in a high pre-test probability population without heart rate control. *Eur Radiol*. 2006;16:2739-47.

3. Raff GL, Gallagher MJ, O'Neill WW, Goldstein JA: Diagnostic accuracy of noninvasive coronary angiography using 64-slice spiral computed tomography. *J Am Coll Cardiol.* 2005;46:552-7.
4. Sarno G, Decraemer I, Vanhoenacker PK, De Bruyne B, Hamilos M, Cuisset T, Wyffels E, Bartunek J, Heyndrickx GR, Wijns W: On the inappropriateness of noninvasive multidetector computed tomography coronary angiography to trigger coronary revascularization: a comparison with invasive angiography. *JACC Cardiovasc Interv.* 2009;2:550-7.
5. Schuijf JD, Wijns W, Jukema JW, Atsma DE, de Roos A, Lamb HJ, Stokkel MP, Dibbets-Schneider P, Decramer I, De Bondt P, van der Wall EE, Vanhoenacker PK, Bax JJ: Relationship between noninvasive coronary angiography with multi-slice computed tomography and myocardial perfusion imaging. *J Am Coll Cardiol.* 2006;48:2508-14.
6. Rispler S, Keidar Z, Ghersin E, Roguin A, Soil A, Dragu R, Litmanovich D, Frenkel A, Aronson D, Engel A, Beyar R, Israel O: Integrated single-photon emission computed tomography and computed tomography coronary angiography for the assessment of hemodynamically significant coronary artery lesions. *J Am Coll Cardiol.* 2007;49:1059-67.
7. Shaw LJ, Berman DS, Maron DJ, Mancini GB, Hayes SW, Hartigan PM, Weintraub WS, O'Rourke RA, Dada M, Spertus JA, Chaitman BR, Friedman J, Slomka P, Heller GV, Germano G, Gosselin G, Berger P, Kostuk WJ, Schwartz RG, Knudtson M, Veledar E, Bates ER, McCallister B, Teo KK, Boden WE; COURAGE Investigators: Optimal medical therapy with or without percutaneous coronary intervention to reduce ischemic burden: results from the Clinical Outcomes Utilizing Revascularization and Aggressive Drug Evaluation (COURAGE) trial nuclear substudy. *Circulation.* 2008; 117:1283-91.
8. Tonino PA, De Bruyne B, Pijls NH, Siebert U, Ikeno F, van't Veer M, Klauss V, Manoharan G, Engström T, Oldroyd KG, Ver Lee PN, MacCarthy PA, Fearon WF; FAME Study Investigators: Fractional flow reserve versus angiography for guiding percutaneous coronary intervention. *N Engl J Med.* 2009;360:213-24.
9. Pijls NH, van Schaardenburgh P, Manoharan G, Boersma E, Bech JW, van't Veer M, Bär F, Hoorntje J, Koolen J, Wijns W, de Bruyne B: Percutaneous coronary intervention of functionally nonsignificant stenosis: 5-year follow-up of the DEFER Study. *J Am Coll Cardiol.* 2007;49:2105-11.
10. George RT, Arbab-Zadeh A, Miller JM, Kitagawa K, Chang HJ, Bluemke DA, Becker L, Yousuf O, Texter J, Lardo AC, Lima JA: Adenosine stress 64- and 256-row detector computed tomography angiography and perfusion imaging: a pilot study evaluating the transmural extent of perfusion abnormalities to predict atherosclerosis causing myocardial ischemia. *Circ Cardiovasc Imaging.* 2009;2: 174-82.
11. Blankstein R, Shturman LD, Rogers IS, Rocha-Filho JA, Okada DR, Sarwar A, Soni AV, Bezerra H, Ghoshhajra BB, Petranovic M, Loureiro R, Feuchtnner G, Gewirtz H, Hoffmann U, Mamuya WS, Brady TJ, Cury RC: Adenosine-induced stress myocardial perfusion imaging using dual-source cardiac computed tomography. *J Am Coll Cardiol.* 2009;54:1072-84.
12. Rogers IS, Cury RC, Blankstein R, Shapiro MD, Nieman K, Hoffmann U, Brady TJ, Abbara S: Comparison of postprocessing techniques for the detection of perfusion defects by cardiac computed tomography in patients presenting with acute ST-segment elevation myocardial infarction. *J Cardiovasc Comput Tomogr.* 2010;4:258-66.
13. Kitagawa K, George RT, Arbab-Zadeh A, Lima JA, Lardo AC: Characterization and correction of beam-hardening artifacts during dynamic volume CT assessment of myocardial perfusion. *Radiology.* 2010;256:111-8.
14. Rodríguez-Granillo GA, Rosales MA, Degrossi E, Rodríguez AE: Signal density of left ventricular myocardial segments and impact of beam hardening artifact: implications for myocardial perfusion assessment by multidetector CT coronary angiography. *Int J Cardiovasc Imaging.* 2010;26:345-54.
15. Stanton CL, Haramati LB, Berko NS, Travin MI, Jain VR, Jacobi AH, Burton WB, Levsky JM: Normal myocardial perfusion on 64-detector resting cardiac CT. *J Cardiovasc Comput Tomogr.* 2011;5:52-60.
16. Ko BS, Cameron JD, Meredith IT, Leung M, Antonis PR, Nasis A, Crossett M, Hope SA, Lehman SJ, Troupis J, DeFrance T, Seneviratne SK: Computed tomography stress myocardial perfusion imaging in patients considered for revascularization: a comparison with fractional flow reserve. *Eur Heart J.* 2011. In Press.

CHAPTER 4:

**MYOCARDIAL DENSITY ANALYSIS UTILIZING AUTOMATED MYOCARDIAL
DEFECT ANALYSIS SOFTWARE ON RESTING 320-DETECTOR MDCT**

With our establishment of a baseline of normal myocardial segmental densities in the setting of wide field of view CT scanning of coronary arteries, we considered the issue of functionally significant obstructive coronary artery disease. A number of investigators had begun to consider the issue of CT stress perfusion and the ability to detect functionally significant ischaemia with density variations of the myocardium[46-49]

Our next aim was to determine whether it was possible, with wide field of view CT scanning, to detect a statistically significant difference between myocardial segments, which were not subject to diseased vessels, versus those which were subject to ischaemia.

We performed a retrospective analysis of a cohort of patients who had confirmed functionally obstructive coronary artery disease by catheter angiography.

Our fourth chapter investigates this relationship with wide field of view CT scanning of the coronary arteries and assessment of the myocardium.

In summary, we intended to investigate the impact of wide field of view CT on myocardial density in order to establish baseline parameter for further work to be performed in myocardial perfusion. Our data confirmed that myocardial density differences between ischaemic and non ischaemic segments was not statistically significant thereby allowing further perfusion work to be performed.

Declaration for Thesis Chapter FOUR

Declaration by candidate

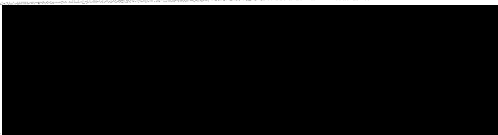
In the case of Chapter Four, the nature and extent of my contribution to the work was the following:

| Nature of contribution | Extent of contribution (%) |
|--|----------------------------|
| Creation of idea, development of structure of the retrospective analysis, creation of the team of researchers, primary authorship, providing technical support for the connection between the two advanced post processing work stations | 70 |

The following co-authors contributed to the work. If co-authors are students at Monash University, the extent of their contribution in percentage terms must be stated:

| Name | Nature of contribution | Extent of contribution (%) for student co-authors only |
|--------------------|--|--|
| Alex Karge | Collected data from interactive work station | Not a University student |
| Sujith Seneviratne | Review of manuscript | Not a University student |
| Arthur Nasis | Review of manuscript | 5 |

The undersigned hereby certify that the above declaration correctly reflects the nature and extent of the candidate's and co-authors' contributions to this work*.

| | | |
|---------------------------------|---|---------------------|
| Candidate's Signature |  | Date 12 Nov 2013 |
| Head of Department's Signature* |  | Date 12/11/13 |

Myocardial density analysis utilizing automated myocardial defect analysis software on resting 320-detector MDCT

John M. Troupis · Alex Karge · Sujith Seneviratne ·
Arthur Nasis · Eileen C. Ang · Brian S. Ko · Dee Nandurkar ·
Eldho Paul · Roland Hilling-Smith · James Cameron

Received: 5 October 2012 / Accepted: 20 December 2012
© Springer Science+Business Media Dordrecht 2013

Abstract Cardiac CT myocardial perfusion is an emerging tool utilizing differences in myocardial density of ischemic compared to normal myocardium. We sought to document the contrast enhanced density profile of myocardial segments subtended by severely stenotic coronary arteries on rest (non stress) cardiac CT imaging, and compare the density with identical segments without ischemic disease. 100 cardiac CT studies were identified resulting in 25 normal patients, 37 with severe left anterior descending artery stenosis, 14 with severe left circumflex artery stenosis, and 24 with severe right coronary artery stenosis. The studies were reviewed on a workstation with dedicated myocardial analysis software. Left anterior descending artery ischemic segments (apical anterior and apical septal) measured 82.2 (± 3) and 102 (± 3) Hounsfield

unit (HU) respectively comparing with non-ischemic segments 89 (± 4) and 109 (± 4) HU respectively (both *P* values 0.16). Left circumflex artery segments (basal anterolateral and mid anterolateral) demonstrated 80 (± 4) and 76 (± 4) HU respectively compared to non-ischemic segments, 89 (± 4) and 87 (± 4) HU (*P* value 0.13 and 0.07 respectively). Right coronary artery ischemic segments (basal inferoseptal and basal inferior) measured 104 (± 3) and 105 (± 3) HU respectively and these compared with non-ischemic segments, 102 (± 4) and 105 (± 4) HU respectively (*P* Value 0.69 and 0.94 respectively). Comparison of ischemic myocardial segments with non-ischemic segments demonstrated no significant difference in myocardial density. In prospectively acquired resting 320 multi detector CT, the myocardium subtended by severely stenotic vessels demonstrates no significant density difference compared with those supplied by vessels with no stenosis, confirming that myocardial ischaemia cannot be reliably detected on rest coronary computed tomography angiography by qualitative nor quantitative assessment.

J. M. Troupis (✉) · E. C. Ang · D. Nandurkar
Department of Diagnostic Imaging, Monash Medical Centre,
Melbourne, VIC, Australia

J. M. Troupis · S. Seneviratne · A. Nasis ·
B. S. Ko · R. Hilling-Smith · J. Cameron
Monash Cardiovascular Research Centre, MonashHEART,
Monash University Department of Medicine, Monash Medical
Centre, Melbourne, VIC, Australia

A. Karge
Department of Biochemistry and Cell Biology, Rice University,
Houston, TX 77251-1892, USA

E. Paul
School of Public Health and Preventive Medicine, Monash
University, Melbourne, VIC, Australia

Keywords Cardiac computed tomography angiography (CCTA) · Perfusion · Myocardial density

Abbreviations

| | |
|--------|--|
| CCTA | Coronary computed tomography angiography |
| CAD | Coronary artery disease |
| MINIPs | Minimum intensity projections |
| MPRs | Multiplanar reconstructions |
| HU | Hounsfield unit |
| PCI | Percutaneous intervention |
| LAD | Left anterior descending artery |
| LCX | Left circumflex artery |
| RCA | Right coronary artery |
| MDCT | Multi detector CT |

Introduction

Coronary computed tomography angiography (CCTA) is now considered a useful diagnostic tool in the setting of stable and acute chest pain syndromes to exclude the presence of coronary artery disease (CAD) [1].

Numerous studies have demonstrated that CCTA has a high negative predictive value in the exclusion of coronary artery disease [2–4]. The clinical significance of moderate severity CAD is usually further assessed with either functional imaging, or coronary catheter angiography with fractional flow reserve assessment [5]. CCTA is widely recognized as suffering from limitations in predicting reversible ischemia [6, 7].

The management of reversible ischemia involves consideration toward revascularization [8, 9], whereas non-reversible ischemia is usually considered for medical therapy [10]. As such, optimal clinical management would entail the combination of both anatomical assessment and functional imaging.

CT detection of functionally significant obstructive coronary artery disease is currently being assessed with the assistance of a pharmacological stress agent such as adenosine, termed myocardial perfusion [11, 12]. CCTA perfusion aims to highlight areas of reduced contrast enhancement in the stress phase, when compared to the rest phase [13].

It has been shown that CCTA may have a role in comprehensive myocardial assessment for infarct detection [14, 15]. In a recent study by Nagao et al. [16], it was found that myocardial hypo enhancement, as determined by myocardial density assessment, can be detected in up to 91 % of patients with acute coronary syndrome, and 96 % of patients with acute myocardial infarct. There has been further suggestion of transient endocardial hypo-enhancement at systole and normal enhancement at diastole as the ischemic pattern on CCTA when defined by rest/stress perfusion scintigraphy [17].

A comparison of reconstruction and viewing parameters on image quality and accuracy of rest and stress myocardial CT perfusion when interpreted by independent readers demonstrated narrow window width and window level settings as optimal for subjective interpretation of perfusion defects [18].

Perfusion CCTA images are assessed with several techniques including minimum intensity projections (MINIPs), thin multiplanar reconstructions (MPRs), and thick MPRs, aiming to detect a difference in HU. Previous studies have demonstrated consistent variation in HU measurements over the lateral aspect of the myocardium in normal patients without CAD [19–21].

Whilst CCTA is able to identify the severity of a stenosis, and while CT stress perfusion is showing promise as

an investigative tool, the determination of whether CCTA is able to detect statistically significant myocardial HU differences in prospectively acquired end diastole non-stress CCTA is unknown.

The purpose of this study is to assess the sensitivity of 320-detector CT in detecting changes in myocardial density in the prospectively acquired mid diastole rest CCTA by comparing patients with severe coronary artery stenoses and patients with no CAD.

Methods

The study was performed as a retrospective audit and was approved by the institutional review board affiliated with our hospital.

The patients were identified from our database of patients having had CCTA over the preceding 24 months (2008–2010) for the assessment of CAD in patients with chest pain at low to intermediate risk of an acute coronary syndrome. All patients were scanned in the resting state with prospective imaging targeting end diastole.

Those patients who subsequently underwent coronary catheter angiography and percutaneous intervention (PCI) of a proximally stenotic dominant artery [Left anterior descending (LAD), Left circumflex artery (LCX), Right coronary artery (RCA)] within 1 week of the CCTA were included for analysis. Of these patients, coronary catheter angiography images were reviewed with quantitative coronary angiography (QCA) analysis (assessed by 2 dimensional analysis of the catheter angiography images (cross sectional area of the stenosis was not assessed). All studies with significant (>75 %) stenosis were included. In addition, patients with entirely normal CCTA were also randomly selected for comparison.

Subjects

Exclusion criteria consisted of patients having a critical stenosis of a non dominant vessel, critical stenosis of the distal segment of a dominant vessel, or of a branch of the main vessel, patients with more than one stenosis, poor quality studies due to motion artifact, or insufficient contrast enhancement. In addition, any patient with known or documented myocardial wall hypertrophy, previous or acute infarct, and collateral circulation (one of the two non stenotic vessels shown to extend to the myocardial segments of interest, in accordance with previously recognized and accepted variation of coronary arterial supply) were excluded. 356 consecutive patients were initially identified. Of these, the following were excluded: Non dominant critical stenosis (22), distal segment dominant vessel stenosis (31), stenosis of a branch of a main vessel (77), more

than one critical stenosis (42), motion artefact (26), insufficient contrast enhancement (21), myocardial wall hypertrophy (30), previous or acute infarct (2), significant collateral circulation (5). After applying our exclusion criteria, 100 patients were identified of which 25 had no coronary artery disease. Of the remaining 75 there were 37 patients with severe LAD stenosis, 14 with severe LCX stenosis, and 24 with severe RCA stenosis.

Patient preparation

Routine CCTA departmental protocol includes patient fasting for at least 2 h before scan acquisition and abstaining from caffeine on the day of scanning. Each patient's heart rate and blood pressure were recorded 1 h before imaging. An 18-gauge IV cannula was inserted into the right antecubital fossa.

All patients with heart rates greater than 60 beats/min were administered beta-blocker medication unless contraindicated (e.g., anaphylaxis or severe asthma). With normal blood pressure confirmed, oral Metoprolol was administered with 50 mg given if heart rate was between 60 and 70 beats/min and 100 mg given if heart rate was greater than 70 beats/min. If the heart rate at the time of the scan remained above 65 beats/min immediately before scanning, IV Metoprolol was administered (up to 30 mg) until the desired heart rate of less than 65 and optimally 60 beats/min was achieved. 400 mcg of sublingual glyceryl trinitrate was given 2 min before imaging for coronary artery dilation.

75mls of Iohexal 56.6 g/75 ml (Omnipaque 350) was administered for each patient at a rate of 6 ml/s, followed by 50 ml of normal saline flush (biphasic contrast injection protocol). Bolus tracking with a region of interest placed in the left ventricle was performed using a 300 HU threshold.

Scan technique

Images were acquired using a 320×0.5 mm detector row CT (Aquillion One, Toshiba Medical Systems). The field of view (z-axis) included the mid-ascending aorta (inferior carina) to the upper abdomen (immediately below the heart base). No table movement occurred during axial volumetric scanning because the scanner provides 16 cm of z-axis volume using 0.5-mm detectors. The number of detectors selected was based on cardiac size as displayed on the anteroposterior and lateral surface images (detectors can be reduced to either 280 or 240 for radiation reduction). All relevant cardiac anatomy was successfully displayed on the field of view. No patient required more z-axis coverage than the detector bank could cover in a single acquisition.

Prospective scanning technique was utilized with phase window acquired between 65 and 80 % and reconstructions

optimized at 75 %. Tube voltages used were optimised at 120 kVp, with variation to 100 kVp depending on the patient's BMI. The tube current ranged between 400 and 580 mAs. The default medium scan field of view (350 mm with adjustment according to patient/anatomy size to include heart) was selected. The large field of view option will result in an increased pixel size and therefore decrease spatial resolution; the small field of view (250 mm) is considered too small for complete coverage of cardiac anatomy and in addition greatly limit the ability to assess adjacent extra cardiac structures, which is a requirement in accordance with departmental policy. The gantry rotation time (tube rotation speed) was 350 ms, with a minimum temporal resolution of 175 ms. Single gantry rotation (single heart beat) occurred if images were obtained with a heart rate of 65 beats/min or less. With the commencement of a dedicated cardiac ct service, our protocol involved exclusively retrospective acquisition. However, we updated our protocols during the relevant study period, resulting in a preference for widening the prospective acquisition window when the heart rate is borderline. In view of the above, there were no patients with two full beat volume acquisitions in the relevant study dates. With regard to current departmental policy, when the patient's heart rate is in sinus rhythm and borderline at or just below 65 beats/min, our departmental protocol indicates preference for widening of the prospective acquisition window to 65–85 %, rather than two beat acquisition. Images were obtained in moderate inspiration with breath holding. Breath-holding and heart rate tests were performed before image-acquisition. The final heart rate was recorded at the time of acquisition.

The scan data was reconstructed at the 75 % R–R phase using 0.5 mm slices overlapping every 0.25 mm using a specialized cardiac algorithm (FC03) to reduce beam-hardening artifacts from the contrast-enhanced descending aorta and the LV manifesting in the LV myocardium [13, 20, 21, 23].

Image data manipulation

If the initial data set demonstrated coronary motion artifact, additional phases were reconstructed.

The left ventricle was divided into sixteen segments according to the American Heart Association classification [24]. The Philips Intellispace Portal (Philips Healthcare, Cleveland, USA) Myocardial Defect Assessment software segments the coronary arteries, four chambers and the myocardium. A physiologically oriented algorithm is applied to the segmented myocardium for both visual (qualitative) and quantification of hypo-dense regions. The calculated results are presented as average density of the myocardium in each segment in normalized Hounsfield

units (HU) [24, 25]. This process of quantitative analysis of HU is automated. Although further quantitative analysis is provided, transmural perfusion ratio (subendocardial attenuation density/subepicardial attenuation density) was not assessed [13].

Analysis

Coronary arterial supply variation to the various myocardial segments is well recognized. For our purposes, we elected to identify relevant myocardial segments, which would be subjected to reduced myocardial blood flow due to severe proximal stenosis in the subtending dominant coronary artery.

Wall thickness was not assessed as known or documented wall thickening and thinning (due to previous infarction) were part of the exclusion criteria.

Statistical analysis

All data were analyzed using SAS software version 9.2 (SAS Institute, Cary, NC, USA). The primary outcome variable myocardial density was assessed for normality and found to be well approximated by a normal distribution. Analysis was performed using repeated measures analysis of variance, as the observations were not independent.

In order to increase the ability to detect a significant difference in density, we grouped the two major segments supplied by the stenotic vessel. The following segments were therefore assessed as one larger myocardial region [24]:

- Left anterior descending artery (LAD)-apical septal, apical anterior,
- Left circumflex artery (LCX)-basal anterolateral, mid anterolateral and
- Right coronary artery (RCA)-basal inferoseptal, basal inferior. The above segments were grouped due to the recognized supply by the relevant dominant vessel, in the absence of collateral circulation.

We compared the ischemic segments of each group with the corresponding segments in the normal group with results reported as parameter estimates \pm standard errors. Furthermore, in order to detect differences between the non-ischemic and ischemic segments, the grouped segments were combined and then compared with the equivalent grouped segments in the non CAD (normal) group. Statistical significance was set at a two-sided *P* value of 0.05.

Results

Age and sex distribution are demonstrated in Table 1 and corresponding radiation dose exposure analysis is outlined

in Table 2. Note is made of the average radiation dose which is considered greater than current standards; however this is considered appropriate for scanning protocols (since updated) which resulted in predominant retrospective acquisitions for the time period of interest. Table 3 demonstrates the mean percentage stenosis in the three subgroups of symptomatic patients.

Average densities for the relevant ischemic and non-ischemic segments are highlighted in Table 4. Table 5 demonstrates the average density obtained when grouping the two relevant segments (average HU) being supplied by the dominant stenotic vessel, and comparing with the combined average density of the equivalent two segments from the normal group.

The HU of the relevant ischemic segments within all three ischemic groups demonstrated no statistically significant difference from the normal group. When comparing the two segments of each stenotic group both individually and combined with the same segments in the normal patients, there was no statistically detectable difference in the density profile.

Discussion

Our study was intended as a preliminary investigation into the possibility that a statistically significant difference in ischemic myocardial density could be documented. Our results indicate that no such difference has been found. We postulate that functionally significant obstructive arterial disease does not produce consistent and detectable reduction in density within the limitation of current parameters of acquisition in routine CCTA scanning.

Despite the fact that changes in myocardial density could not be detected, there is evidence that changes in coronary enhancement do correlate with disease, especially with regard to contrast differences and contrast gradients [26, 27]. Moreover there is evidence that contrast differences, even those with 64-detector row CT that are then normalized to aortic enhancement, are related to flow [28].

Although our finding is contrary to the previous findings of Nagao et al. [29] our acquisitions were performed with

Table 1 Gender and age distribution

| Group | Total number (M:F) | Age, median (IQR) |
|---------------|--------------------|-------------------|
| Normal | 25 (12:13) | 70 (59–79) |
| LAD ischaemia | 37 (21:16) | 68 (54–76) |
| LCX ischaemia | 14 (7:7) | 63 (59–76) |
| RCA ischaemia | 24 (19:5) | 72 (56–77) |

IQR inter-quartile range

Table 2 Radiation dose exposure

| | Average DLP | Min DLP | Max DLP | Mean effective dose | Minimum effective dose | Maximum effective dose | Retrospective | Prospective |
|---------|-------------|---------|---------|---------------------|------------------------|------------------------|---------------|-------------|
| LAD | 945.97 | 325.5 | 1899.83 | 13.24 | 4.56 | 26.6 | 23 | 12 |
| LCx | 1064.17 | 291.41 | 1899.83 | 14.9 | 4.08 | 26.6 | 8 | 5 |
| RCA | 822.13 | 291.41 | 1709.93 | 11.51 | 4.08 | 23.94 | 11 | 9 |
| Normals | 1231.83 | 408.7 | 1876.8 | 17.25 | 5.72 | 26.28 | 12 | 2 |
| Overall | 983.31 | 325.99 | 1849.58 | 13.77 | 4.56 | 25.90 | | |

Table 3 Mean percentage stenosis in the three subgroups of stenosis

| Mean percentage stenosis | | |
|--------------------------|-----|-----|
| LAD | LCX | RCA |
| 75 | 78 | 76 |

Table 4 Myocardial density (HU) in comparable ischemic and non ischemic segments

| | LAD territory myocardial density (HU) | |
|----------------|---------------------------------------|----------------------------|
| | Apical anterior | Apical septal |
| Normal group | 89.5 ± 4.1 | 109.9 ± 4.1 |
| LAD ischemia | 82.2 ± 3.1 | 102.6 ± 3.1 |
| <i>P</i> value | 0.16 | 0.16 |
| | LCX territory myocardial density (HU) | |
| | Basal anterolateral | Mid anterolateral |
| Normal group | 89.5 ± 4.1 | 87.2 ± 4.1 |
| LCX Ischemia | 80.8 ± 4.0 | 76.9 ± 4.0 |
| <i>P</i> value | 0.13 | 0.07 |
| | RCA territory myocardial density (HU) | |
| | Basal inferoseptal | Basal inferior (segment 4) |
| Normal group | 102.2 ± 4.1 | 105.5 ± 4.1 |
| RCA ischemia | 104.3 ± 3.4 | 105.9 ± 3.4 |
| <i>P</i> value | 0.69 | 0.94 |

Values are parameter estimates ± standard errors

prospective scanning targeting end diastole, without assessment of systolic and diastolic density differences.

The possibility of a more critical stenosis (>90 %) consistently producing reduced myocardial density has been previously introduced. Our stenosis were on average at between 75 and 80 % and due to small numbers within each of the ischaemic groups, we have been unable to investigate this issue.

As our results demonstrate no statistically detectable difference in myocardial density between normal and segments supplied by severely stenotic vessels, we propose

Table 5 Combining relevant ischemic segments and comparing with corresponding segments of normal patients

| | HU density average | SE | <i>P</i> value |
|---|--------------------|-----|----------------|
| <i>LAD relevant segments: grouped apical anterior & apical septal</i> | | | |
| Normal | 99.7 | 3.9 | 0.14 |
| LAD | 92.4 | 2.9 | |
| <i>LCX relevant segments: grouped basal anterolateral & mid anterolateral</i> | | | |
| Normal | 88.4 | 3.9 | 0.15 |
| LCX | 81.3 | 2.9 | |
| <i>RCA relevant segments: grouped basal inferoseptal & basal inferior</i> | | | |
| Normal | 103.8 | 3.9 | 0.78 |
| RCA | 105.2 | 2.9 | |

SE standard error

that studies evaluating the myocardial density, either at rest or with stress, should consider this assessment be performed quantitatively, rather than qualitatively.

We note that there is a difference in kVp utilized throughout the studies due to differences in patient body habitus. Although the variation of kVp is recognized as having influence on HU, for the purpose of detection of significant difference in density of contrast enhanced myocardium, this is thought to be not statistically significant [22]. Our results also demonstrate the previously recognized consistent appearance of reduction in HU density over the basal and mid lateral and inferolateral LV myocardium in all four groups [21].

Basal and mid inferolateral myocardial density reduction is currently of unknown cause [21] and thought due to a combination of causes including increased density of structures adjacent to the inferior and septal myocardium (diaphragm and right heart) contributing to an increase in HU density owing to beam hardening artifacts. This is contrasted with the inferolateral and lateral myocardium, which is typically located adjacent to aerated lung, and therefore less subject to beam hardening artifact.

Although there is no visually detectable reduction in HU density in clinically affected ischemic myocardial segments, when utilizing automated assessment of HU density,

and statistically analyzing the results, no statistically significant difference in density could be documented.

Our study utilized automated density assessment, which produced an average HU density for each segment. As has been documented in stress cardiac MRI [30], the possibility of reduction in density of the subepicardium component of the ischemic myocardial segments is raised and consideration toward specific assessment of subepicardial density may be of use [13]. The limitations of a quantitative system are also recognized, with the possibility of small perfusion defects averaging out and perfusion defects straddling different segments also diluting the effect on the calculated segment density.

A limitation of our study is the absence of significant numbers of patients with critical (>90 %) stenosis. Almost all of our patients had stenoses between 75 and 80 %. The number of critical stenosis patients was thought too small to be assessable. This may be a consideration for further investigation.

As CCTA is acquired with routine intravenous contrast media, Iohexal (56.6 g/75 ml), the possibility of small changes in myocardial density becoming detectable with increased density of the contrast media is raised.

Stress myocardial perfusion has been increasingly utilized for the detection of myocardial density differences. Our work would suggest that the severe 75 % stenosis is, in itself, unable to produce significant flow reduction however note is also made of recent work indicating that coronary gradients assessment may be of use in this area.

Dual energy scanning may offer further potential in eliciting relatively minor or subtle myocardial density differences due to the possibility of iodine mapping with or without stress imaging [31–33]. The CCTA study using a 320-row detector system is typically a prospectively acquired study, at a single point in time during the R–R cycle, where the examination is performed in a single phase of contrast perfusion within a component of a single heart beat. It is possible that variations in myocardial enhancement and density would be visible and detectable in different phases of the cardiac cycle and also at different points in time in contrast perfusion through the myocardium. As our study was retrospective, we were not able to investigate differences in density due to either perfusion timing or phase timing. We do not routinely acquire CCTA with extended scanning times to assess perfusion variability. This may be a consideration for further exploration with the advent of significant reduction in radiation dose exposure. In addition, we considered normal CCTA as normal; we do recognize the accepted gold standard of catheter-based angiography however we believe that due to the accepted high negative specificity of CCTA, this was a reasonable perspective.

Beta-blockade medication for the purpose of heart rate control by definition, contributes to alteration in heart rate

and contractility. The effect on myocardial density may also be a limitation, however the use of metoprolol is well recognized as being utilized in heart rate control for CT myocardial perfusion imaging.

A further limitation of our study is inclusion of all patients who might possibly be prone to small vessel accelerated atheromatous disease, such as diabetics, hypertensives or connective tissue disorders. Further analysis of this sub group of patients may well be of use in evaluation of myocardial density differences.

Conclusion

When comparing the density of myocardium supplied by a dominant vessel with at least 75 % stenosis (confirmed at QCA) and without significant collateral circulation, with identical segments of normal patients, we confirm that we were unable to detect statistically significant differences between the two groups of patients. As such, this study may be considered as a baseline demonstrating that resting density difference between ischemic and non-ischemic myocardium at end diastole is not detectable. Further analysis in the setting of stress myocardial perfusion, with or without dual energy scanning may be of use.

Conflict of interest All of the above co authors disclose that there is neither conflict of interest nor financial disclosure for this manuscript.

References

- Schlett CL, Banerji D, Siegel E et al (2011) Prognostic value of CT angiography for major adverse cardiac events in patients with acute chest pain from the emergency department: 2-year outcomes of the ROMICAT trial. *JACC Cardiovasc Imaging* 4:481–491
- Budoff MJ, Dowe D, Jollis JG et al (2008) Diagnostic performance of 64-multidetector row coronary computed tomographic angiography for evaluation of coronary artery stenosis in individuals without known coronary artery disease: results from the prospective multicenter ACCURACY (assessment by coronary computed tomographic angiography of individuals undergoing invasive coronary angiography) trial. *J Am Coll Cardiol* 52:1724–1732
- Raff GL, Gallagher MJ, O'Neill WW, Goldstein JA (2005) Diagnostic accuracy of noninvasive coronary angiography using 64-slice spiral computed tomography. *J Am Coll Cardiol* 46: 552–557
- Scheffel H, Alkadhi H, Plass A et al (2006) Accuracy of dual-source CT coronary angiography: first experience in a high pre-test probability population without heart rate control. *Eur Radiol* 16:2739–2747
- Sarno G, Decraemer I, Vanhoenacker PK et al (2009) On the inappropriateness of noninvasive multidetector computed tomography coronary angiography to trigger coronary revascularization: a comparison with invasive angiography. *JACC Cardiovasc Interv* 2:550–557
- Schuijf JD, Wijns W, Jukema JW et al (2006) Relationship between noninvasive coronary angiography with multi-slice

- computed tomography and myocardial perfusion imaging. *J Am Coll Cardiol* 48:2508–2514
7. Rispler S, Keidar Z, Ghersin E et al (2007) Integrated single-photon emission computed tomography and computed tomography coronary angiography for the assessment of hemodynamically significant coronary artery lesions. *J Am Coll Cardiol* 49:1059–1067
 8. Shaw LJ, Berman DS, Maron DJ et al (2008) Optimal medical therapy with or without percutaneous coronary intervention to reduce ischemic burden: results from the clinical outcomes utilizing revascularization and aggressive drug evaluation (COURAGE) trial nuclear substudy. *Circulation* 117:1283–1291
 9. Tonino PA, De Bruyne B, Pijls NH et al (2009) Fractional flow reserve versus angiography for guiding percutaneous coronary intervention. *N Engl J Med* 360:213–224
 10. Pijls NH, Fearon WF, Tonino PA et al (2010) Fractional flow reserve versus angiography for guiding percutaneous coronary intervention in patients with multivessel coronary artery disease: 2-year follow-up of the FAME (fractional flow reserve versus angiography for multivessel evaluation) study. *J Am Coll Cardiol* 56:177–184
 11. Ko BS, Cameron JD, DeFrance T, Seneviratne SK (2011) CT stress myocardial perfusion imaging using multidetector CT—a review. *J Cardiovasc Comput Tomogr* 5:345–356
 12. Ko BS, Cameron JD, Meredith IT et al (2012) Computed tomography stress myocardial perfusion imaging in patients considered for revascularization: a comparison with fractional flow reserve. *Eur Heart J* 33:67–77
 13. George RT, Arbab-Zadeh A, Miller JM et al (2009) Adenosine stress 64- and 256-row detector computed tomography angiography and perfusion imaging: a pilot study evaluating the transmural extent of perfusion abnormalities to predict atherosclerosis causing myocardial ischemia. *Circ Cardiovasc Imaging* 2:174–182
 14. Ghoshhajra BB, Maurovich-Horvat P, Techasith T et al (2012) Infarct detection with a comprehensive cardiac CT protocol. *J Cardiovasc Comput Tomogr* 6:14–23
 15. Mehra VC, Valdiviezo C, Arbab-Zadeh A et al (2011) A stepwise approach to the visual interpretation of CT-based myocardial perfusion. *J Cardiovasc Comput Tomogr* 5:357–369
 16. Nagao M, Matsuoka H, Kawakami H et al (2009) Myocardial ischemia in acute coronary syndrome: assessment using 64-MDCT. *AJR Am J Roentgenol* 193:1097–1106
 17. Nagao M, Matsuoka H, Kawakami H et al (2009) Detection of myocardial ischemia using 64-slice MDCT. *Circ J* 73:905–911
 18. Ghoshhajra BB, Rogers IS, Maurovich-Horvat P et al (2011) A comparison of reconstruction and viewing parameters on image quality and accuracy of stress myocardial CT perfusion. *J Cardiovasc Comput Tomogr* 5:459–466
 19. Rogers IS, Cury RC, Blankstein R et al (2010) Comparison of postprocessing techniques for the detection of perfusion defects by cardiac computed tomography in patients presenting with acute ST-segment elevation myocardial infarction. *J Cardiovasc Comput Tomogr* 4:258–266
 20. Rodriguez-Granillo GA, Rosales MA, Degrossi E, Rodriguez AE (2010) Signal density of left ventricular myocardial segments and impact of beam hardening artifact: implications for myocardial perfusion assessment by multidetector CT coronary angiography. *Int J Cardiovasc Imaging* 26:345–354
 21. Crossett MP, Schneider-Kolsky M, Troupis J (2011) Normal perfusion of the left ventricular myocardium using 320 MDCT. *J Cardiovasc Comput Tomogr* 5:406–411
 22. Stadler A, Schima W, Prager G et al (2004) CT density measurements for characterization of adrenal tumors ex vivo: variability among three CT scanners. *AJR Am J Roentgenol* 182: 671–675
 23. Kitagawa K, George RT, Arbab-Zadeh A, Lima JA, Lardo AC (2010) Characterization and correction of beam-hardening artifacts during dynamic volume CT assessment of myocardial perfusion. *Radiology* 256:111–118
 24. Cerqueira MD, Weissman NJ, Dilsizian V et al (2002) Standardized myocardial segmentation and nomenclature for tomographic imaging of the heart: a statement for healthcare professionals from the Cardiac Imaging Committee of the Council on Clinical Cardiology of the American Heart Association. *Circulation* 105:539–542
 25. Lamash YLJ, Gringauz A (2011) An automatic method for the identification and quantification of myocardial perfusion defects or infarction from cardiac CT images. *IEEE international symposium on biomedical imaging: from nano to macro*, 2011, pp 1314–1317. doi:10.1109/ISBI.2011.5872642
 26. Rybicki FJ, Otero HJ, Steigner ML et al (2008) Initial evaluation of coronary images from 320-detector row computed tomography. *Int J Cardiovasc Imaging* 24:535–546
 27. Steigner ML, Mitsouras D, Whitmore AG et al (2010) Iodinated contrast opacification gradients in normal coronary arteries imaged with prospectively ECG-gated single heart beat 320-detector row computed tomography. *Circ Cardiovasc Imaging* 3:179–186
 28. Chow BJ, Kass M, Gagne O et al (2011) Can differences in corrected coronary opacification measured with computed tomography predict resting coronary artery flow? *J Am Coll Cardiol* 57:1280–1288
 29. Nagao M, Matsuoka H, Kawakami H et al (2008) Quantification of myocardial perfusion by contrast-enhanced 64-MDCT: characterization of ischemic myocardium. *AJR Am J Roentgenol* 191:19–25
 30. Chan W, Ellims AH, Duffy SJ, Kaye DM, Taylor AJ (2011) Principles, current status and clinical implications of ischemic heart disease assessment by cardiac magnetic resonance imaging. *Intern Med J*
 31. Kim ST, Lee H, Paik SH, Park JS (2012) Apical-sparing variant of stress cardiomyopathy: integrative analysis with multidetector row cardiac computed tomography in dual-energy mode. *J Cardiovasc Comput Tomogr* 6:140–142
 32. So A, Lee TY, Imai Y et al (2011) Quantitative myocardial perfusion imaging using rapid kVp switch dual-energy CT: preliminary experience. *J Cardiovasc Comput Tomogr* 5:430–442
 33. Arnoldi E, Lee YS, Ruzsics B et al (2011) CT detection of myocardial blood volume deficits: dual-energy CT compared with single-energy CT spectra. *J Cardiovasc Comput Tomogr* 5:421–429

CHAPTER 5:**THE NEW 4-DIMENSIONAL COMPUTED TOMOGRAPHIC SCANNER ALLOWS
DYNAMIC VISUALISATION AND MEASUREMENT OF NORMAL
ACROMIOCLAVICULAR JOINT MOTION IN AN UNLOADED AND LOADED
CONDITION**

A further extension of the utility of wide field of view CT, beyond tissue perfusion, was the concept of motion. Although 4D CT has been used in radiation therapy planning since the advent of 4 cm z axis 64 slice multidetector CT units, the significantly wider latest generation CT units have not been fully explored.

Our next consideration was to determine whether 4D CT, with a 16 cm z axis, could be of use in the musculoskeletal imaging field and in particular in the setting of joint imaging. Although MRI has traditionally offered excellent spatial and contrast resolution for the assessment of internal derangement[50, 51], it has been limited in motion assessment. Motion disorders of joints have been largely previously assessed non operatively through clinical examination, ultrasound or fluoroscopic imaging[52].

We considered the acromioclavicular[53] joint (AC) to be of interest due to the recognized difficulty in managing mid range severity separations[54-56].

As the AC joint has not been previously assessed with 4D CT, we considered establishing a baseline of measurements detailing the amount and type of motion of the AC joint in asymptomatic volunteers. We also aimed to determine whether any age related changes in this joint were detectable. We present our fifth publication.

Declaration for Thesis Chapter FIVE

Declaration by candidate

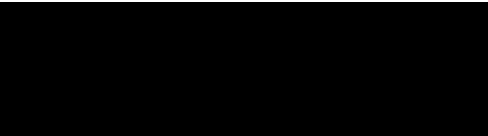
In the case of Chapter Five, the nature and extent of my contribution to the work was the following:

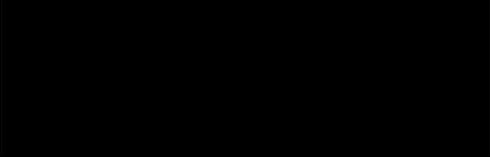
| Nature of contribution | Extent of contribution (%) |
|--|----------------------------|
| Creation of idea, development of structure of the retrospective analysis, creation of the team of researchers, providing technical support for the connection between the two advanced post processing work stations | 50 |

The following co-authors contributed to the work. If co-authors are students at Monash University, the extent of their contribution in percentage terms must be stated:

| Name | Nature of contribution | Extent of contribution (%) for student co-authors only |
|------------------|--|--|
| Tjarco D Alta | Collected data from interactive work station, primary authorship | Not a University student |
| Simon N Bell | Review of manuscript | Not a University student |
| Jennifer Coghlan | Review of manuscript | Not a University student |

The undersigned hereby certify that the above declaration correctly reflects the nature and extent of the candidate's and co-authors' contributions to this work*.

| | | |
|-----------------------|---|---------------------|
| Candidate's Signature |  | Date 12 Nov 2013 |
|-----------------------|---|---------------------|

| | | |
|---------------------------------|---|---------------|
| Head of Department's Signature* |  | Date 12/11/13 |
|---------------------------------|---|---------------|

The New 4-Dimensional Computed Tomographic Scanner Allows Dynamic Visualization and Measurement of Normal Acromioclavicular Joint Motion in an Unloaded and Loaded Condition

Tjarco D. Alta, MD,*† Simon N. Bell, PhD, FRCS, FRACS, FAOrthA,*‡
John M. Troupis, MBBS, FRANZCR,§ Jennifer A. Coghlan, PhD,*‡
and David Miller, MBChB, MRCS, FRCS(Orth)*

Objective: Using 4-dimensional computed tomographic scanner to determine the motion pattern of the acromioclavicular (AC) joint during adduction of the arm, with and without resisted superior elevation.

Methods: Sixteen healthy volunteers (5 women and 11 men; mean \pm SD age, 42 ± 11 years). Four different motions were measured: AC joint width, anteroposterior translation, superoinferior translation, and opening of the superior aspect of the joint. Measurements between arm positions of neutral, adduction, and loaded were compared.

Results: Predominant movement is posterior translation (1.1 ± 0.9 mm, $P = 0.001$); in the coronal plane, superior translation of the clavicle (0.6 ± 0.5 mm, $P = 0.001$) and some opening of the superior joint space. Changes in the AC joint width and anteroposterior translation were significantly related to age ($P = 0.016$ and $P = 0.006$).

Conclusions: Four-dimensional computed tomographic scans record the motion pattern of an asymptomatic AC joint and demonstrated that in adduction plus resisted elevation of the arm, the main movement of the AC joint is posterior and superior translation of the clavicle.

Key Words: AC joint motion, motion analysis, BvR test, acromioclavicular joint, 4D CT scan

(*J Comput Assist Tomogr* 2012;36: 749–754)

Imman et al¹ discussed the combined contribution of the clavicle, scapula, and humerus to overall shoulder movement in 1944. In this complex system, the integrated motion of the acromioclavicular (AC), sternoclavicular (SC), glenohumeral, and scapulothoracic joints are required.²

Several authors have investigated the motion of the clavicle using a 3-dimensional (3D) electromagnetic tracking system.^{3–8} However, this method has some disadvantages, such as skin motion artifacts of the sensors.^{3,9} Ludewig et al¹⁰ used a similar tracking system combined with transcortical pins into the

clavicle, scapula, and humerus, allowing the sensors to be rigidly fixed. Describing the motion of the AC joint in a noninvasive way, Sahara et al^{2,11} used a vertically open magnetic resonance imaging (MRI) and scanned the arm in 7 static abducted positions in the coronal plane. With the recent arrival of the 4D computed tomographic (CT) scanner, it is now possible to scan a 16-cm volume in 0.175 second, resulting in cine motion with 6 frames per second. We postulated that it should be possible to scan shoulder joint motion within this volume, thus recording the movement in real time of the AC joint.

The previously described new test for AC joint pathology, the Bell-van Riet (BvR),¹² distinguishes itself from other AC joint pathology tests by adding load to the joint when the arm is adducted. This test has proven its sensitivity, and a positive sign is pain combined with the inability of the patient to maintain the arm in the adducted position against resisted elevation. Movement in pathological joints would cause pain by compression of inflamed tissues. It is known that in the BvR test, the motion produced in the AC joint causes pain, which is why the test is positive in pathological AC joints. However, it is unclear what kind of motion takes place in the AC joint when the test is performed.

To try and understand the movements of the AC joint during the BvR test, this study was devised. It determines the pattern of normal motion in the AC joint with the arm in adduction, in an unloaded and a loaded condition, using the 4D CT scanner.

MATERIALS AND METHODS

Sixteen healthy volunteers, 5 women and 11 men, without a history of shoulder complaints, a normal shoulder examination with no pain on AC joint palpation, and negative O'Brien and BvR test results, participated in this study. The mean \pm SD age of the volunteers was 42 ± 11 years (range, 23–60 years). The institutional ethics committee approved the research protocol, and all participants gave their written informed consent before the scan procedure.

The Aquilion One (Toshiba Medical Systems, Otawara-shi, Tochigi-ken, Japan) 4D CT scanner was used. This machine has 320 detectors with 0.5 mm between each detector. During axial volumetric scanning, no table movement occurs because the detectors cover a 16-cm volume from superior to inferior in one rotation with a duration of 0.35 seconds. As only half of the gantry rotation cycle is required (180 degrees) for imaging, temporal resolution is therefore 175 milliseconds. Repeating this process makes it possible to scan real-time motion within this 16-cm volume. The amount of radiation to which the volunteer is exposed is calculated by using the recorded dose length product and multiplying this with the organ-specific conversion

From the *Melbourne Shoulder and Elbow Centre, Melbourne, Australia; †Department of Orthopaedic Surgery and Traumatology, Onze Lieve Vrouwe Gasthuis, Amsterdam, The Netherlands; ‡Department of Surgery, Monash University, Melbourne, Australia; and §Department of Diagnostic Imaging, Monash Medical Centre, Melbourne, Australia.

Received for publication March 14, 2012; accepted August 6, 2012.

Reprints: Simon N. Bell, PhD, FRCS, FRACS, FAOrthA, Melbourne Shoulder and Elbow Centre, 31 Normanby St, Brighton, Victoria 3186, Australia (e-mail: snbell@bigpond.net.au).

No funding was received from the National Institutes of Health (NIH), Wellcome Trust, Howard Hughes Medical Institute (HHMI), or any other source.

Ethical Board Review statement: Research Directorate, Southern Health, Monash Medical Centre, Melbourne, Australia Approval number 09247B; approved October 20, 2009.

Copyright © 2012 by Lippincott Williams & Wilkins

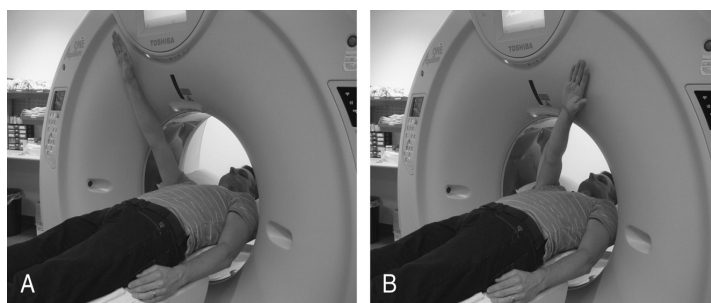


FIGURE 1. Supine position of the volunteer in the 4D CT scan, with the shoulder within the gantry. A, Neutral starting position with the arm elevated to approximately 90 degrees in the sagittal plane. Demonstrating the limitation of the arm movement by the gantry. B, The adducted position of the arm and the loading position with resistance of the gantry, simulating the BvR test.

factor. In the case of the AC joint, the cervical spine conversion factor is used. This product is then termed the effective dose in millisievert (mSv). This corresponds with an effective radiation exposure of 2.5 to 3.5 mSv per scan. The volunteers were positioned supine on a couch in the scanner so that their shoulder joint was within the 16-cm volume of the scan. The neutral starting position was with the arm elevated to 90 degrees in the sagittal plane with their hand against the gantry (Fig. 1A), resulting in an unrestricted positioning of the scapula, without fixation or compression against the thorax, or the x-ray couch. During the 7-second duration of the scan, the volunteers adducted their arm at shoulder level and then loaded the AC joint by pressing their arm against the gantry for 4 seconds, simulating the BvR test (Fig. 1B).

The motion of the AC joint was calculated by measuring the position of the distal end of the clavicle in relation to the acromion at 3 shoulder positions (neutral, adduction, and loaded). The difference between those positions expressed in millimeters (mm) represents the motion. For those 3 positions, the AC joint width in the transverse plane was measured as well as the anteroposterior (AP) translation in the transverse plane, the superoinferior translation, and the opening of the superior aspect of the AC joint in the coronal plane. The width of the AC joint was measured in the middle of the AC joint at the articular surface (Fig. 2). The AP translation was measured also at the level of the articular surface of the joint by drawing a line anterior to the acromion perpendicular to the joint line and a second line anterior to the clavicle parallel to this (Fig. 3). The distance between those 2 parallel lines represents the amount of AP translation, with the anterior side of the perpendicular line having a positive value and the posterior side a negative value. To be able to measure

the superoinferior motion of the distal end of the clavicle, a horizontal line is drawn under the acromion. The distance from the inferior angle of the distal clavicle to this line was measured, with the inferior side of this line having a negative value and the superior side having a positive value. To determine the opening of the superior aspect of the AC joint, a vertical line in the coronal plane was drawn along the articular side of the acromion. The horizontal distance from this line to the superior angle of the distal clavicle was measured.

With regard to maintaining accurate and reproducible measurements from the 2D images, which were reconstructed from the 4D motion study, each of the aforementioned measurements was assessed at the mid level of the respective perpendicular plane. That is, for the purpose of measuring the AC joint space in the transverse dimension, the middle point of the joint was identified in the coronal plane (ie, exactly halfway from anterior to posterior) by cross-referencing both the coronal with the axial plane. For the purpose of measuring AC joint AP translation in the axial plane, the middle portion of the joint space in the coronal plane was identified and the AP measurement was taken at this point. With this technique, reproducibility could be confirmed as all joints were measured at exactly the mid point of the joint, regardless of the 3D motion, which was being assessed. Furthermore, using the aforementioned technique negated the effect of any potential clavicular rotation as the mid point of the joint was always identified.

Statistical analysis was performed by a one-sample *t* test to determine if the motion produced in the adducted position with and without load significantly affected the AC joint width, anteroposterior translation, superoinferior translation, and opening of the superior aspect of the AC joint. Furthermore, we used

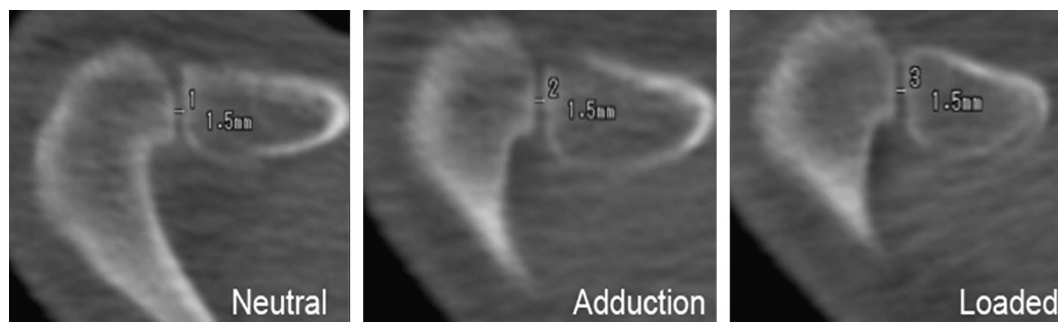


FIGURE 2. Width of the AC joint in the transverse plane for the neutral, adduction, and loaded positions. The width was measured in the middle of the AC joint at the articular surface.

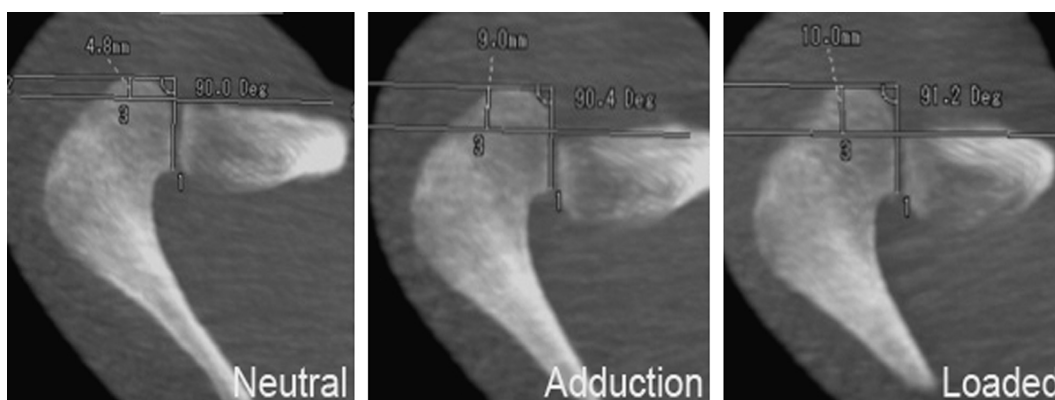


FIGURE 3. Anteroposterior translation of the clavicle compared to the acromion for the neutral, adduction, and loaded positions. The translation was measured at the level of the articular surface of the joint by drawing a line anterior to the acromion perpendicular to the joint line and a second line anterior to the clavicle parallel to this. The distance between those 2 parallel lines represents the amount of anteroposterior translation, with the anterior side of the perpendicular line having a positive value and the posterior side a negative value.

general linear models to assess the effects of sex and age on the amount of motion taking place for the neutral-to-adduction, neutral-to-loaded, and adduction-to-loaded positions. Significance level was set at $P = 0.05$.

RESULTS

The 4 data sets (AC joint width, anteroposterior translation, superoinferior translation, and opening of the superior aspect) between the neutral, adduction, and loaded positions are presented in Table 1 (in very few images due to technical reasons; it was difficult to perform accurate measurements, resulting in lower n values). In the transverse plane, during the movement from neutral to adduction and then when the AC joint was loaded, the width of the AC joint remained nearly constant. The greatest motion in the AC joint for these movements was anteroposterior translation, with the clavicle moving posterior in

relation to the acromion. In the coronal plane, the motion actually consists of 2 movements (Fig. 4), with superior translation of the clavicle being the main part of the AC joint motion, combined with some opening of the superior aspect of the joint.

Loading of the AC joint in the adducted position, simulating the BvR test, resulted in a significant increase in posterior and superior translation of the clavicle ($P = 0.001$; Table 1). There was also an increased opening of the superior aspect of the joint, but this was not significant ($P = 0.269$). Figure 5 shows the association between the AP translation in the transverse plane and age, demonstrating that the amount of motion decreases to zero as age increases (neutral to adduction, $P_{\text{age}} = 0.05$; and neutral to loaded, $P_{\text{age}} = 0.006$). Significant association was also found between the AC joint width for the adduction to loaded positions and age, $P_{\text{age}} = 0.016$. Figure 6 indicates that during the BvR test, not only the amount but also the direction of movement is influenced by age. All the other

TABLE 1. Four Different Data Sets (AC Joint Width, AP Translation, Superoinferior Translation, and Opening of the Superior Aspect) Taking Place in the AC Joint Between the Neutral, Adduction, and Loaded Positions

| AC Joint Motion | Neutral to Adduction | Neutral to Loaded (in Adduction) | Adduction to Loaded | CI and P of Change in Clavicle Position |
|---|---|--|--|---|
| | (mm) | (mm) | (mm) | |
| AC Joint width (transverse plane) to mean \pm SD (range) | 0.0 ± 0.6 (-0.9 to 1.9) $n = 16$ $P_{\text{age}} = 0.885$ | 0.0 ± 0.8 (-1.2 to 1.9) $n = 14$ $P_{\text{age}} = 0.540$ | -0.1 ± 0.3 (-0.8 to 0.4) $n = 14$ $P_{\text{age}} = 0.016$ | * |
| Anteroposterior translation (transverse plane) to mean \pm SD (range) | -1.6 ± 2.3 (-5.3 to 3.3) $n = 16$ $P_{\text{age}} = 0.050$ | -3.1 ± 2.6 (-7.6, 0.5) $n = 14$ $P_{\text{age}} = 0.006$ | -1.1 ± 0.9 (-2.3 to -0.6) $n = 14$ $P_{\text{age}} = 0.138$ | (-1.6 to -0.5) $P = 0.001$ |
| Superoinferior translation (coronal plane) to mean \pm SD (range) | 1.9 ± 1.5 (1.0-2.8) $n = 14$ $P_{\text{age}} = 0.378$ | 2.5 ± 1.9 (1.3-3.7) $n = 12$ $P_{\text{age}} = 0.536$ | 0.6 ± 0.5 (0.0-1.5) $n = 13$ $P_{\text{age}} = 0.401$ | (0.3-0.9) $P = 0.001$ |
| Opening superior aspect AC joint (coronal plane) to mean \pm SD (range) | 0.4 ± 0.8 (-0.1 to 0.9) $n = 14$ $P_{\text{age}} = 0.403$ | 0.6 ± 0.8 (0.1-1.1) $n = 12$ $P_{\text{age}} = 0.897$ | 0.2 ± 0.6 (-1.0 to 0.9) $n = 13$ $P_{\text{age}} = 0.334$ | (-0.2 to 0.5) $P = 0.269$ |

A positive value represents widening anterior or superior translation, and a negative value represents narrowing posterior or inferior translation.

For each of the 3 comparisons, sample sizes (n), which differed for some of the comparisons and the P value, P_{age} of the test for a trend with age are provided. For the adduction to loaded differences, 95% confidence intervals and P values for the mean differences are also given.

*Because the change in AC joint width adduction to loaded depends on age, confidence intervals and P values for the mean change are inappropriate (see also Fig. 6).

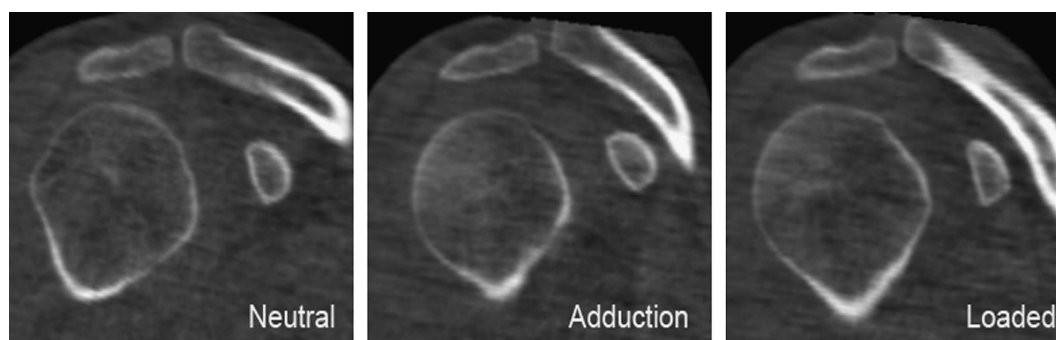


FIGURE 4. Coronal plane for the neutral, adduction, and loaded positions demonstrates that the clavicle is not only moving superiorly but the superior aspect of the AC joint is also opening up.

associations with age were not significant. In addition, none of the associations with sex were found to be significant.

DISCUSSION

The motion of the AC joint has been investigated by several authors using a 3D electromagnetic tracking system³⁻⁸ combined with either skin sensors or transcortical pins for rigid fixation of the sensors,¹⁰ or using a vertically open MRI,^{2,11} all having their advantages and disadvantages. With the arrival of the new 4D CT scanner, it is now possible to noninvasively scan osseous shoulder joint motion in real time. Because our understanding was incomplete as to what kind of motion takes place in the AC joint when the BvR test¹² is performed, we used the 4D CT scanner to determine the motion pattern of the AC joint in a normal shoulder during arm movement and loading that simulated the BvR test.

Use of the 4D CT scanner has some restrictions. First, the motion that can be recorded with the 4D CT scan needs to take place within the gantry of the scanner. This limits the measurable elevation of the shoulder to approximately 90 degrees (Fig. 1A) or a similar motion for scapular plane abduction when measurements are performed in the lateral decubitus position. Sahara et al² have described significant differences in the

motion of the AC joint between the mid range (30–90 degrees) and at the end range (150 degrees maximum) of shoulder abduction. It was possible, however, in this study to adequately scan the motion of the AC joint while simulating the BvR test¹² as the resisted elevation component could be simulated by the volunteers compressing their arm in the adducted position against the gantry for 4 seconds (Fig. 1B). To our knowledge, the motion of the AC joint in living subjects during adduction of the arm, together with loading in resisted elevation, has never been previously described. Second, in the supine position of the volunteers, gravity and the weight of the shoulder girdle result in some posterior force on the shoulder, in contrast to an inferior force in an upright position. This, however, would be a very small force compared with the force of the muscular contraction. During the test, the scapula is elevated from the couch underneath so there should be only a slight alteration in the position of the scapula from the variation in the direction of gravity. Ideally, the scan should have been performed in an upright position; however, this is technically not possible.

The movement of the AC joint in living subjects has been studied by several authors^{2-6,8,10,11} and several cadaveric studies have been conducted as well.^{6,13-15} Teece et al⁶ compared in vitro passive motion in cadaver specimens to in vivo active

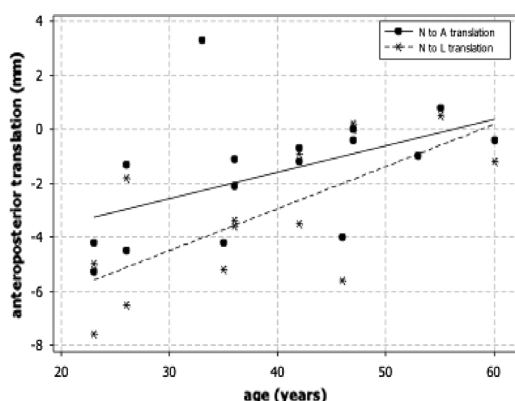


FIGURE 5. Scatterplot of the differences between the neutral-to-adduction and neutral-to-loaded positions for AP translation in the transverse plane compared to age. A positive value of the AP translation implies anterior translation, whereas a negative value implies posterior translation, demonstrating that in our group, the amount of motion taking place decreases toward zero as age increases.

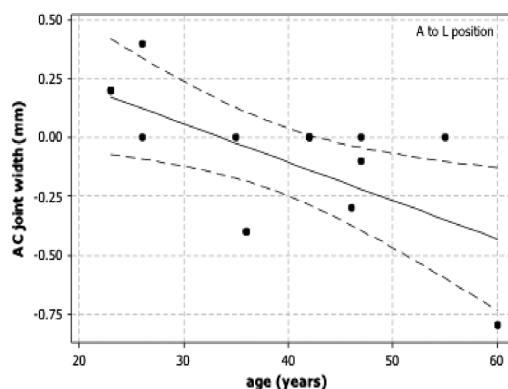


FIGURE 6. Scatterplot of the difference between the adduction and loaded positions for the AC joint width in the transverse plane versus age. A positive value of the AC joint movement implies widening, whereas a negative value implies narrowing. The solid line is the fitted regression line, and the dotted curves are the 95% confidence limits for the mean difference at different ages. This demonstrates that in our group, the amount and the direction of movement is influenced by age.

motion in live subjects, during scapular plane abduction (measured with an electromagnetic tracking device). They found an increased posterior motion in the AC joint in cadavers compared to the active motion of volunteers (in an upright position). This indicates that the deltoid muscle, as the main motor for motion of the glenohumeral joint, and perhaps also the pectoralis minor muscle, is pulling the AC joint more anteriorly. They also found that the AC joint showed less superior movement in passive cadaver testing, which may be due to lack of upper trapezius muscle activation of the joint. Similar motion patterns were demonstrated by Fung et al,¹⁶ which demonstrate that active motion in living subjects is necessary to represent a normal AC joint motion pattern and Sahara et al^{2,11} measured the motion of the AC joint of living subjects with a vertically open MRI in 7 static abducted positions in the coronal plane from 0 degree to maximum abduction with 30-degree intervals, each image requiring 2 minutes 35 second of scanning. This way of measuring the AC joint motion approaches the dynamic movement of the arm, but it is still not a fluid motion with continuous muscle contraction. Therefore, the optimal technique would be 3D in vivo measurements of shoulder kinematics without skin motion artifacts of the sensors. This was obtained by Ludewig et al,¹⁰ where active elevation was measured with the use of a 3D electromagnetic tracking system and transcortical pins into the clavicle, scapula, and humerus. None of the studies previously mentioned measured the motion of the AC joint with the arm adducted and the use of the 4D CT scanner to study active shoulder motion allows dynamic real-time measurements with 3D images and only with a radiation exposure of 2.5 to 3.5 mSv per scan (background radiation is 2.0–3.0 mSv per year). As the obtained images are reconstructed as a volume image, by using a workstation, it is possible to manipulate the images so that they can be examined either as a 3D volume-rendered view (viewing the surface of the sample being imaged) or as a 2D cross-section in any plane. Once the desired surface view is selected, it is possible to view the cross-section file of this region/section to examine changes with motion and perform the measurements (Figs. 2–4). The millimeter amount of measured translation of the distal end of the clavicle in this study in different planes (Table 1) is of similar range to another study,² which measured the AC joint motion in millimeters during elevation. The only motion that could not be measured in this study was the axial rotation of the clavicle relative to the acromion.

The BvR test¹² has clinically proven its sensitivity; however, it was not clear what kind of motion took place in the AC joint during the test, which could account for the pain and weakness in a positive test. The BvR test is a modification of the cross-body adduction test and active compressive test, as described by O'Brien et al.¹⁷ During the O'Brien test, the arm is adducted to only 15 degrees and the acromion is loaded by the supraspinatus tendon compressing the AC joint from the under surface of the acromion,¹⁸ leading to a positive result of the test. The BvR test adds loading to the AC joint in full adduction to produce the positive result. In this study, it was shown that the loading produces predominately extra posterior translation of the distal end of the clavicle in the transverse plane (Table 1). It also provides superior translation and some opening of the superior aspect of the AC joint in the coronal plane. We assume these movements of the clavicle relative to the acromion produces tissue and joint surface stress, resulting in a positive response to the test when there is pathologic abnormality in the AC joint.

We also investigated whether there is an association between AC joint motion and age because in general, joints tend to have a reduced range of motion in older people as the capsule

and ligaments lose their flexibility. The statistically significant association we found between anteroposterior translation and age (Fig. 5) demonstrates that AC joint flexibility reduces with age. This could also explain why excision of the distal clavicle has, in general, a good clinical outcome in the older patients but can lead to anteroposterior instability in younger patients.

In trying to place the applicability of this technique in a broader spectrum of the musculoskeletal system, there are a number of potential clinical applications for the 4D CT scan analysis of dynamic joint motion, such as, athletes who developed pain arising from the AC joint but have normal imaging, in which a 4D CT scan could demonstrate pathological AC joint movement. In the knee, dynamic tracking of the patella could be demonstrated and in the wrist, the precise movements of the carpal bones during motion. The Aquilion One, with 320 detectors, is well suited for this kind of motion analysis, as it has a reasonably large z-axis coverage of 16 cm, which will cover most joints and keep them in the field of view despite the joint moving to new positions. All other CT scanners have less than 16 cm; however, the next largest z-axis coverage of 8 cm with the 256-slice scanner may potentially be useful in smaller joints. The 64-slice machines have a z-axis coverage of approximately 4 cm and therefore are of limited usefulness.

In conclusion, the new 4D CT scan is an investigation tool that can be used to record the motion pattern of the AC joint in a normal shoulder during active movement. It demonstrated that in adduction plus resisted elevation, to simulate the BvR test, the primary movement of the AC joint is posterior and superior translation of the clavicle relative to the acromion, with some opening of the superior aspect of the joint, but with little alteration of the width of the joint. This gives good insight in what happens to the AC joint during the BvR test.

ACKNOWLEDGMENTS

The authors thank all those who kindly volunteered to take part in this study. They also thank Marcus Crossett, chief CT radiographer, Diagnostic Imaging, Monash Medical Centre and Southern Health Care Network, Melbourne, Australia, for performing all the scans and his participation in the development of this study. The authors likewise thank Ken Sharpe from the Statistical Consulting Centre, Department of Mathematics and Statistics, University of Melbourne, Australia, for his help with the statistical analysis and interpretation of their data.

REFERENCES

1. Inman VT, Saunders JB, Abbott LC. Observations of the function of the shoulder joint. *Clin Orthop Relat Res.* 1944;1996:3–12.
2. Sahara W, Sugamoto K, Murai M, et al. 3D kinematic analysis of the acromioclavicular joint during arm abduction using vertically open MRI. *J Orthop Res.* 2006;24:1823–1831.
3. Ludewig PM, Behrens SA, Meyer SM, et al. Three-dimensional clavicular motion during arm elevation: reliability and descriptive data. *J Orthop Sports Phys Ther.* 2004;34:140–149.
4. Meskers CG, Vermeulen HM, de Groot JH, et al. 3D shoulder position measurements using a six-degree-of-freedom electromagnetic tracking device. *Clin Biomech (Bristol, Avon).* 1998;13:280–292.
5. Pronk GM, van der Helm FC, Rozendaal LA. Interaction between the joints in the shoulder mechanism: the function of the costoclavicular, conoid and trapezoid ligaments. *Proc Inst Mech Eng H.* 1993;207:219–229.
6. Teece RM, Lunden JB, Lloyd AS, et al. Three-dimensional acromioclavicular joint motions during elevation of the arm. *J Orthop Sports Phys Ther.* 2008;38:181–190.

7. McClure PW, Michener LA, Sennett BJ, et al. Direct 3-dimensional measurement of scapular kinematics during dynamic movements in vivo. *J Shoulder Elbow Surgery*. 2001;10:269–277.
8. Ebaugh DD, McClure PW, Karduna AR. Three-dimensional scapulothoracic motion during active and passive arm elevation. *Clin Biomech (Bristol, Avon)*. 2005;20:700–709.
9. Karduna AR, McClure PW, Michener LA, et al. Dynamic measurements of three-dimensional scapular kinematics: a validation study. *J Biomech Eng*. 2001;123:184–190.
10. Ludewig PM, Phadke V, Braman JP, et al. Motion of the shoulder complex during multiplanar humeral elevation. *J Bone Joint Surg Am*. 2009;91:378–389.
11. Sahara W, Sugamoto K, Murai M, et al. Three-dimensional clavicular and acromioclavicular rotations during arm abduction using vertically open MRI. *J Orthopa Res*. 2007;25:1243–1249.
12. van Riet RP, Bell SN. Clinical evaluation of acromioclavicular joint pathology: sensitivity of a new test. *J Shoulder Elbow Surg*. 2011;20:73–76.
13. Cattrysse E, Baeyens JP, Van Roy P, et al. Intra-articular kinematics of the upper limb joints: a six degrees of freedom study of coupled motions. *Ergonomics*. 2005;48:1657–1671.
14. Klimkiewicz JJ, Williams GR, Sher JS, et al. The acromioclavicular capsule as a restraint to posterior translation of the clavicle: a biomechanical analysis. *J Shoulder Elbow Surg*. 1999;8:119–124.
15. Lee KW, Debski RE, Chen CH, et al. Functional evaluation of the ligaments at the acromioclavicular joint during anteroposterior and superoinferior translation. *Am J Sports Med*. 1997;25:858–862.
16. Fung M, Kato S, Barrance PJ, et al. Scapular and clavicular kinematics during humeral elevation: a study with cadavers. *J Shoulder Elbow Surg*. 2001;10:278–285.
17. O'Brien SJ, Pagnani MJ, Fealy S, et al. The active compression test: a new and effective test for diagnosing labral tears and acromioclavicular joint abnormality. *Am J Sports Med*. 1998;26:610–613.
18. Parentis MA, Jobe CM, Pink MM, et al. An anatomic evaluation of the active compression test. *J Shoulder Elbow Surg*. 2004;13:410–416.

CHAPTER 6:

**DYNAMIC MOTION ANALYSIS OF DART THROWERS MOTION VISUALIZED
THROUGH COMPUTERIZED TOMOGRAPHY AND CALCULATION OF THE
AXIS OF ROTATION**

An extension of the 4D CT and functional joint imaging concept was to determine if this technical innovation would be of benefit in assessment of a poorly understood joint with regard to dynamic motion. We considered the wrist joint, and in particular the intercarpal related motion.

It is recognized that wrist joints with excess laxity have scaphoid rotation mainly along the sagittal plane of flexion and extension, during hand lateral/radial deviation. In contrast, wrists with decreased laxity demonstrate scaphoid rotation mostly in the coronal plane with radioulnar deviation with minimal flexion extension[57]. However, this understanding has arisen from either cadaveric[58, 59], in vivo surgical, or fluoroscopic imaging with image intensifier, the latter subject to the absence of the ability to perform cross sectional analysis.

In order to address motion disorders of the wrist, an establishment of normal baseline measurements is required. We considered the dart throwers motion. This motion has been considered [60] to be of significance in scapho-lunate ligament disorders and is now considered the index motion of the wrist.

We present our sixth publication establishing, with cross sectional accuracy, the exact motion of the wrist when undergoing dart throwers motion.

Declaration for Thesis Chapter SIX

Declaration by candidate

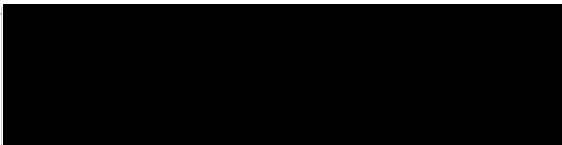
In the case of Chapter Six, the nature and extent of my contribution to the work was the following:

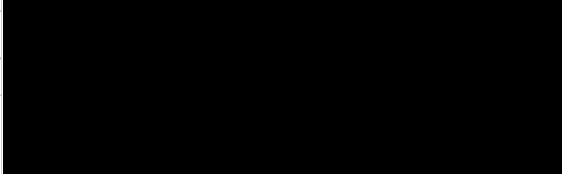
| Nature of contribution | Extent of contribution (%) |
|--|----------------------------|
| Creation of idea, development of structure of the prospective analysis, intimately involved with the writing of the paper with the primary author, guiding the primary author in the assessment with the interactive work station and the analysis of the volume rendered images | 50 |

The following co-authors contributed to the work. If co-authors are students at Monash University, the extent of their contribution in percentage terms must be stated:

| Name | Nature of contribution | Extent of contribution (%) for student co-authors only |
|---------------------------|--|--|
| Yasith Edirisinghe | Primary authorship, collection of data | Not a University student |
| Minoo Patel | Review of manuscript | Not a University student |
| Julian Smith | Review of manuscript | Not a University student |

The undersigned hereby certify that the above declaration correctly reflects the nature and extent of the candidate's and co-authors' contributions to this work*.

| | | |
|------------------------------|--|----------------------------|
| Candidate's Signature |  | Date 12 Nov 2013 |
|------------------------------|--|----------------------------|

| | | |
|--|--|-------------------------|
| Head of Department's Signature* |  | Date 12/11/13 |
|--|--|-------------------------|

Dynamic motion analysis of dart throwers motion visualized through computerized tomography and calculation of the axis of rotation

The Journal of Hand Surgery
(European Volume)
0E[0] 1–9
© The Author(s) 2013
Reprints and permissions:
sagepub.co.uk/journalsPermissions.nav
DOI: 10.1177/1753193413508709
jhs.sagepub.com


Y. Edirisinghe

Department of Surgery, Monash University, Victoria Epworth Healthcare, Richmond, Victoria, Australia

J. M. Troupis

Department of Diagnostic Imaging, Southern Health, Victoria, Australia

M. Patel

Department of Surgery, Monash University, Victoria Epworth Healthcare, Richmond, Victoria, Australia

J. Smith

Department of Surgery, Monash University, Victoria, Australia

M. Crossett

Department of Diagnostic Imaging, Southern Health, Victoria, Australia

Abstract

We used a dynamic three-dimensional (3D) mapping method to model the wrist in dynamic unrestricted dart throwers motion in three men and four women. With the aid of precision landmark identification, a 3D coordinate system was applied to the distal radius and the movement of the carpus was described. Subsequently, with dynamic 3D reconstructions and freedom to position the camera viewpoint anywhere in space, we observed the motion pathways of all carpal bones in dart throwers motion and calculated its axis of rotation. This was calculated to lie in 27° of anteversion from the coronal plane and 44° of varus angulation relative to the transverse plane. This technique is a safe and a feasible carpal imaging method to gain key information for decision making in future hand surgical and rehabilitative practices.

Keywords

Dart throwers motion, carpal kinematics, 4D CT, musculoskeletal imaging, motion mapping, axis of rotation, midcarpal joint

Date received: 1st January 2013; revised: 7th February 2013; accepted: 7th February 2013

Introduction

The wrist is a complex joint. It involves articulation of eight small bones with intricate inter- and intra-osseous kinematics. They demonstrate multidirectional movement and synergy that allow for the unique motion of the hand. In particular, the dart throwers motion has been considered to have given humans an evolutionary advantage by allowing for enhancement of power swing as well as improvement in hand precision for the use of weapons, tools, and instruments (Rohde et al., 2010; Wolfe et al.,

2006; Young, 2003). The term *dart throwers motion* (DTM) was popularized by the work of Palmer et al. (1985), when they described the functional movements of the wrist. DTM describes a carpal movement pathway from radial extension to ulnar flexion.

Corresponding author:

Dr. Yasith Edirisinghe, Epworth Healthcare, 5, Silverash Drive, Bundoora, VIC 3121, Australia

Studies have shown that the axis of rotation of this motion does not adhere to the pure orthogonal flexion/extension, radial/ulnar deviation planes of wrist movement (Ishikawa et al., 1999; Werner et al., 2004). Thus, imaging DTM has been a considerable challenge using two-dimensional (2D) imaging modalities such as plain radiography, cineradiography, sonic digitization, or fluoroscopy (Arkless, 1966; Berger et al., 1982; Linscheid et al., 1972; Ruby et al., 1988; Wolfe et al., 1997). 3D computerized tomography (CT) has been used to map the DTM pathway using multiple static position imaging (Kamal et al., 2012; Wolfe et al., 1997; 2000). The next step to advance the knowledgebase of carpal kinematics demands a dynamic motion mapping method that can be performed on live subjects while performing unrestricted natural motion (Moojen et al., 2003; Wolfe et al., 2000). This was previously deemed unfeasible due to lack of technology and potential unsafe radiation exposure posed to participants (Wolfe et al., 2006).

With advancing technology, this challenge may finally have a solution. With the advent of 4D CT imaging, i.e., dynamic recording of 3D images over time, we had the opportunity to capture dynamic motion sequences of subjects performing unrestricted natural DTM. This novel technology is an excellent tool for 3D dynamic motion capture. Garcia-Elias et al. (2013) managed to demonstrate the difference in motion patterns of the scaphoid and lunate in patients with and without scapholunate instability.

The calculation of the unique axis of rotation of DTM has recently been documented using surface marker techniques by Brigstocke et al. (2012) and calculated to lie 44° to the sagittal plane of the wrist. Dynamic-volume rendered 4D CT technology also provides us with a platform to do a mathematical calculation of the axis of rotation of DTM using carpal bone topography.

We hypothesized that *in vivo* dynamic analysis of DTM may provide new information regarding the mid-carpal kinematics of DTM and allow us to mathematically define the DTM axis of rotation.

Methods

We utilized 4D CT to acquire high-resolution dynamic motion imaging of the wrist in seven adult volunteers with normal wrists during unrestricted DTM. This study was conducted under the auspices of the Diagnostic Imaging Department of Southern Health (Clayton, Victoria, Australia).

Prior to the wrist scans, volunteers were trained to perform the desired motion under the guidance of a

hand surgeon and radiologist. Volunteers then performed the DTM motion in the CT scanner over 3–5 s. Subjects were aided in their posture by being made to grasp and throw a pen forward as if it were a dart over 3–5 s. The accuracy of the scan was reviewed closely by a musculoskeletal radiologist who confirmed whether the anatomical start and end positions of the DTM were met. The start position was defined as the anatomical congruent articulation of the trapezoid with the waist of the scaphoid; and the end point was defined as the engagement of the hook of hamate with the triquetrum. If the start and end points were not met, the scan was repeated until the end points were achieved. Complete scans were achieved within a mean of 2.28 (range 1–3) attempts. Radiation exposure for three DTM scans was calculated not to exceed 0.15 mSv.

4D CT sequence acquisition

The nomenclature of 4D CT is derived from its ability to capture an extra dimension to 3D CT, namely time. Examinations were performed using a 320-slice detector CT (Aquilion ONE™, Toshiba™ Medical Systems, Tokyo, Japan). The scanner is capable of acquiring 16 cm of z-axis volume data in half a gantry rotation without table movement. When performed repeatedly over a length of time, a dynamic volume study is achieved. For the purpose of this study, wrists were scanned over 5–6 s while performing DTM in the CT scanner.

The scanner had inbuilt mechanisms to minimize radiation exposure to very low levels for these dynamic scans. The Aquilion ONE™ CT scanner can scan a 16 cm z-axis in one rotation, and so eliminate the need for helical scanning, which greatly helps to reduce the radiation dose. In addition, the scanner uses the adaptive iterative dose reduction (AIDR) algorithm, which allows for radiation dose minimization by reducing the noise in both the 3D reconstruction data and raw data domains. This allows for up to 75% radiation dose reduction for the same standard deviation for noise (Deák et al., 2012; Kulkarni et al., 2012; Romagnoli et al., 2012; Singh et al., 2012; Yamada et al., 2012; Yoon et al., 2012)

As per institution protocol, a radiation exposure analysis was undertaken prior to the informed consent process. For this purpose, an independent medical physicist was employed as nominated by the Southern Health Human Research Ethics Committee. Using detailed knowledge of previous 4D CT scans for both upper limb impingement, lower limb impingement, and thoracic interventional studies, the degree of expected radiation exposure including CT dose index (CTDI), dose length product (DLP), and



Figure 1. Set-up of the volunteer performing DTM.

the conversion factor (0.0001) were calculated. The effective maximum dose of radiation to any one study volunteer was calculated to be 0.15 mSv. This compares favourably with a normal background radiation for any individual, which is 2 mSv per year (Charles, 2001). Thus, the risk posed by this study under the principle of ALARA (as low as reasonably achievable) was considered very low.

In our study, the full 16 cm z-axis helix was centred over the wrist and its surrounding structures. The scan acquisition was initiated manually and the patient was instructed to perform DTM (Figure 1). Once the movement was completed, the acquisition was terminated manually. For maximum temporal resolution, the tube rotation time was set to the minimum 350 ms. The tube potential was 80 kVp with 80 mA.

The dynamic data were reconstructed into volume data sets or *phases* using a 180° interpolator. These phases were reconstructed time contiguously every 175 ms, resulting in a frame rate of approximately six phases/s. Each phase was reconstructed using contiguous 0.5 mm slices. An iterative reconstruction technique was used in preference to a traditional filtered back projection to further improve signal-to-noise ratio.

Multiple high-resolution 3D moving models were reconstructed over time with the Vitrea Enterprise Suite™ Version 6.3 (Vital Images, Inc., Minnetonka, Minnesota, USA). This software allows advanced manipulation of 3D models with accurate surface marker placement on topographical landmarks. It also allows for measurement of the distance and angles between these markers, which can then be applied to mathematical models to acquire the desired kinematic information.

Observation of dynamic motion of carpal bones

The Vitrea software allowed us to create high-resolution 3D models of the wrist performing DTM. This software

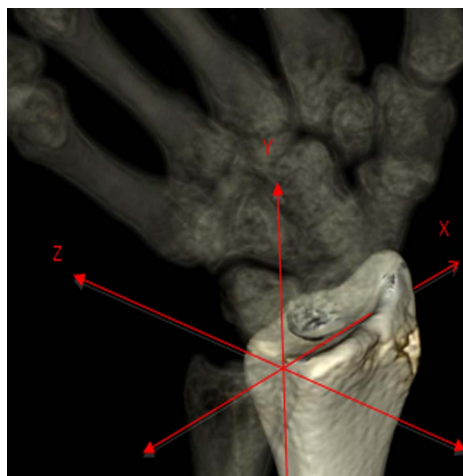


Figure 2. Set-up of the coordinate system on the distal radius. X is incremental from ulnar-radial direction, Y is incremental from proximal-distal direction, and Z is incremental from volar-dorsal direction.

allows for click, drag, and zoom to any desired point in space around the wrist model.

The camera was positioned in space around multi-dimensional volume-rendered images at ventral/lateral, ventral/medial, dorsal/medial, and dorsal/lateral positions. The wrist was then studied in dynamic motion, and displacement of the carpal bones relative to each other was measured. These are demonstrated in Figures 4–6. The clinical validity and applicability of using volume-rendered 4D CT technology in this manner and the measuring techniques have been proven by the work of Blum et al. (2009).

Examples of taped videos of the DTM viewed through three different viewpoints (camera visualizing the coronal plane, oblique plane between coronal and sagittal planes, and sagittal plane) can be accessed in the online content accompanying this article (Videos 1–3). We were also able to manipulate, zoom in, and focus on any bone at any time of the sequence and make observations from any angle as desired.

Calculation of the axis of rotation

We analyzed the volume-rendered sequences by using a mathematical modelling algorithm, which utilized the trilateration principle to place a point of interest onto a coordinate system based on the distal radius (Manolakis, 1996). This coordinate system was defined with the origin ($x=0, y=0, z=0$) centred on the midpoint between the volar and dorsal corners of the ulnar side of the radius (Figure 2). The

z-axis was defined as the line connecting the volar to the dorsal corner of the ulnar side of the distal radius. The x-axis was calculated by utilizing the line perpendicular to the previously defined z-axis running through the point at the tip of the radial styloid. Then the x-axis was derived by trigonometry by factoring in the radial height of the wrist. Thus, the x-axis runs from ulnar to radial direction of the distal radius. The y-axis was then defined as the orthogonal axis relative to these defined x and z axes using trigonometry. The y-axis thus lies in line with the radial shaft (Figure 2). The Vitrea software allowed us to perform markerless bone analysis through identification of topographical landmarks on carpal bones. Markers were applied manually to the dorso-ulnar corner of the radius, volar-ulnar corner of the radius, and tip of the radial styloid. We measured the distances between points of interest on a carpal bone (i.e., capitate) to each of these points. Using the mathematical principle of trilateration, accurate 3D coordinates for these points were derived (Manolakis, 1996).

In this study, the capitate axis of rotation was calculated. We placed two clearly identifiable topographical landmarks on the capitate, i.e., proximal and distal poles (P1 and P2), and their coordinates were calculated as defined. Vector *a* was defined as the vector P1 – P2 at radial extension of the capitate, and vector *b* was defined as the vector P1 – P2 at full ulnar flexion. The axis of rotation of the capitate in DTM can be defined as the cross product of vectors *a* and *b* (Figure 3a–c). The necessary analytical computer coding was written using MATLAB™ (MathsWorks, Natick, Massachusetts, USA) for the above mathematical derivations.

This study was conducted under the auspices and approval of Human Research and Ethics committee of Southern Health.

Results

Our data show that DTM involves substantial motion of the midcarpal joint (between the proximal and distal carpal rows), besides large radiocarpal joint motion. The four distal row bones were observed to move as one intercalated unit with no motion in between them. We observed that the loose packing proximal carpal row allowed for toggle movements to accommodate the distal carpal row in DTM. This can be seen in the Videos 1–3, which accompany this article online. Figure 4a–d demonstrates the wrist from four different viewpoints at full radial extension, and Figure 5a–c demonstrates the wrist in full ulnar

flexion. Video 4 demonstrates a 360° spin of the wrist at full radial extension, and Video 5 demonstrates a 360° spin of the wrist at full ulnar flexion.

The following carpal morphological features and kinematical behaviour were noted on close observation of the DTM sequences.

Lunate-capitate hinge

We observed that in DTM the distal carpal row flexed relative to the proximal carpal row. The pivot point for this motion was observed to lie between the lunate and capitate (Figure 6). The lunate-capitate anatomical interface is a ball socket arrangement and can accommodate global range of motion. In DTM, the net force from the flexors was demonstrated to drive the motion of the capitate on the lunate in a uniform direction. This axis was calculated and will be demonstrated later in this article.

Trapezium-trapezoid motion arc

The trapezium and trapezoid bones moved in a motion arc guided by the congruence of the convexity of the dorsum of the scaphoid in ulnar-flexion movement (Videos 1–3). At full radial extension, the trapezium lies over the dorsal waist of the scaphoid, and the trapezoid is congruent with the dorsal waist of the scaphoid (Figure 4d). The trapezium and trapezoid glide over the distal scaphoid. The scaphoid was also found to have subtle toggle movements to accommodate this motion (Figure 5b).

Hamate-triquetrum motion

The triquetrum-hamate articulation moved with the distal carpal segment in the axis of rotation defined by the lunate-capitate hinge. The triquetrum demonstrated toggle motion in all seven wrists to accommodate the subtle hamate topographical irregularities. Views at the extremity of ulnar flexion demonstrated engagement of the hook of hamate with the triquetrum (Figure 5a,c). This abutment of the hook of hamate with the triquetrum was observed to provide a mechanical block to further ulnar flexion.

Calculation of DTM axis of rotation

The axis of rotation of the DTM was determined by calculating the axis of rotation of the capitate relative to the distal radius, through mathematical derivation of the cross product of the initial and final positions of the capitate. The result from this calculation was a

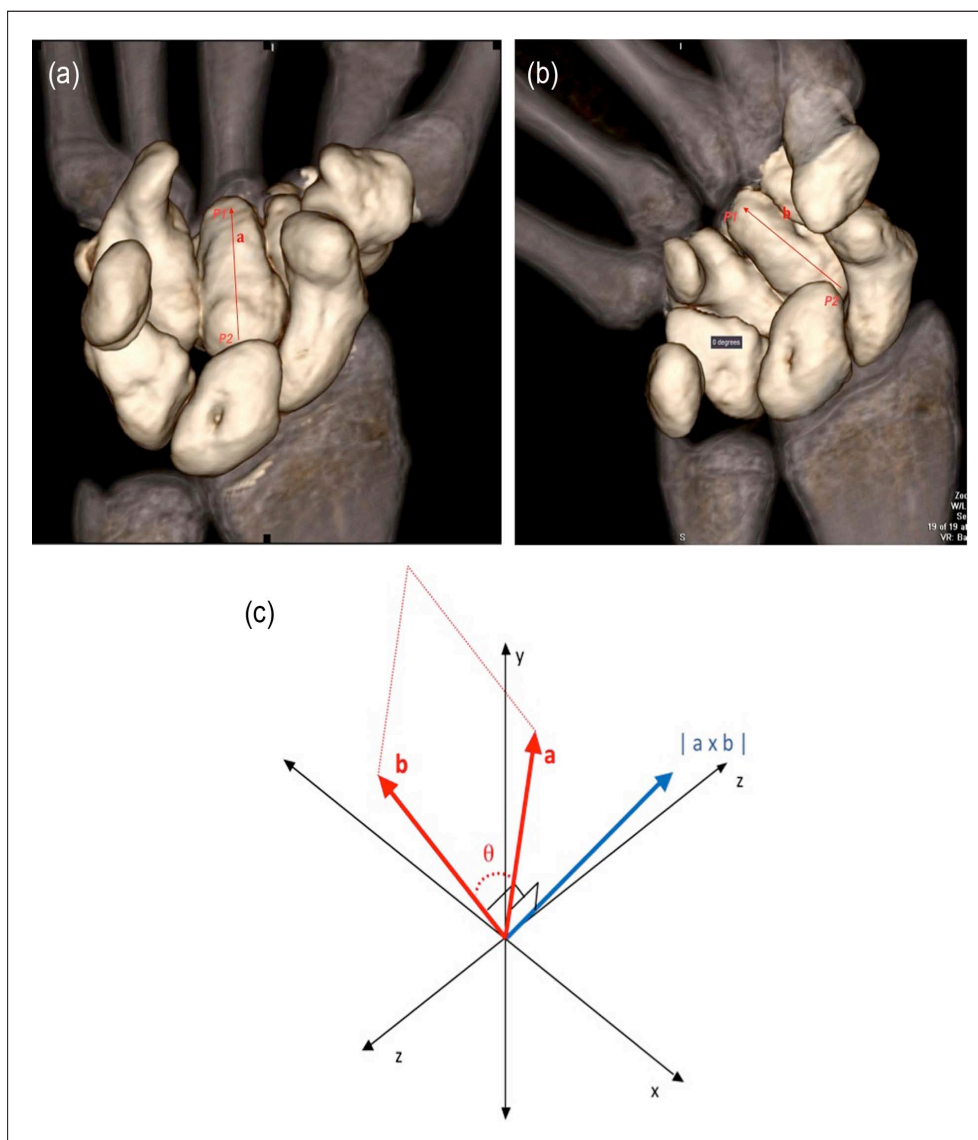


Figure 3. (a) Definition of vector a . (b) Definition of vector b . (c) Mathematical derivation of the axis of rotation of the capitate. This can be calculated by calculating the cross product of vector a and vector b (represented as $|a \times b|$). (The cross product of two vectors' point is a vector perpendicular to the two vectors, as per this figure).

unit vector of $[0.6730, 0.6468, -0.3446]$ to represent the axis of rotation. These figures can be interpreted as the axis of rotation pointing from the centre of rotation of DTM in the lunate-capitate hinge to a point 0.6730 unit radial, 0.6468 unit distal, and 0.3446 unit volar. This can also be described in different terms as the axis of rotation pointing from the centre of rotation in the lunate-capitate hinge to the direction of 27° [95% CI 21.1–32.3] of anteversion (angle between axis of rotation and coronal plane) and 44° [95% CI 32.8–54.9] of angulation with the transverse plane.

Discussion

The 4D CT imaging modality allowed for dynamic acquisition of unrestricted DTM. Imaging the carpus in dynamic sequences as in this study is practical and safe. This methodology can have significant diagnostic application to clinical practice in investigating poorly understood pathologies as well as evaluating outcomes of surgical and rehabilitative practices (Alta et al., 2012; Garcia-Elias, 2008). The dose length product for upper limb radiation exposure remains a

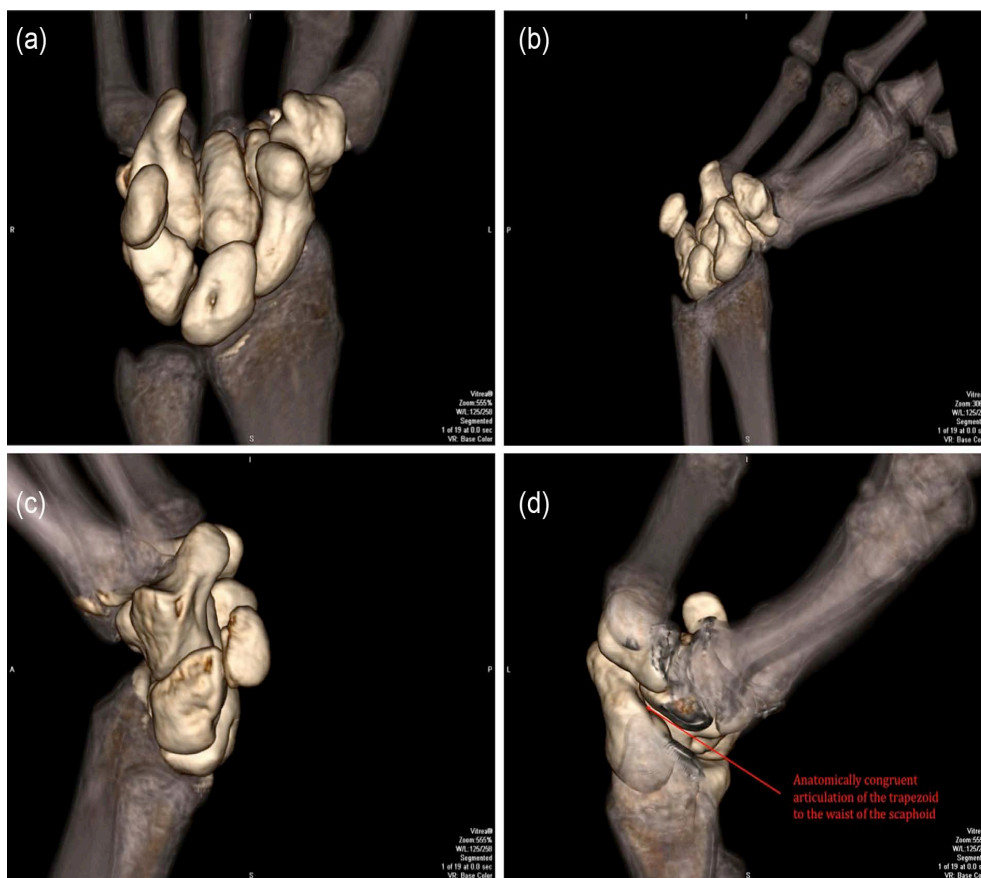


Figure 4. (a) View of the wrist in full radial extension from an anterior to posterior view point. (b) View of the wrist in full radial extension from a radial to ulnar view point. (c) View of the wrist in full radial extension from an ulnar to radial view point. This view aids to illustrate the position of the hamate relative to the triquetral. (d) Wrist in full radial extension with the camera viewpoint set-up between sagittal and posterior-anterior plane looking towards the ulnar-volar direction. This figure closely demonstrates the anatomical congruent articulation of the trapezoid to the ulnar side of the waist of the scaphoid.

very low value, and thus, the risk of harm from radiation from these scans remains extremely low [Alta et al., 2012].

Before the availability of this technology, carpal kinematics analyses largely consisted of models of motion using static position imaging [Moritomo et al., 2004; 2008]. In 2004, Moritomo et al. presented video models to demonstrate radial-ulnar deviation sequences of the wrist using CT and magnetic resonance imaging. These sequences were constructed with separate static scans of the wrist being positioned along the radial-ulnar deviation pathway at 15° increments. However, these static imaging methods were limited by their ability to acknowledge inertial or functional effects of dynamic motion [Moritomo et al., 2004]. Through the technology used in this study, we were able to capture dynamic in vivo DTM at a rate of

6 frames/s. This enabled us to make observations and mathematical calculations to describe carpal behaviour. The main findings of this study can be summarized as follows.

1. DTM demonstrates a definable pathway of motion through the mid-carpal joint. This can be described as a hinge motion of the distal carpal row on the proximal carpal row with the centre of rotation situated in the lunate-capitate joint.
2. The distal carpal row (trapezium, trapezoid, capitate, and hamate) behaves as one intercalated unit with no movement observed between the bones. However, we must acknowledge that “no movement” is the general finding based on video observation. Previous investigators reported a small range of motion (< 5–10°) using a variety of

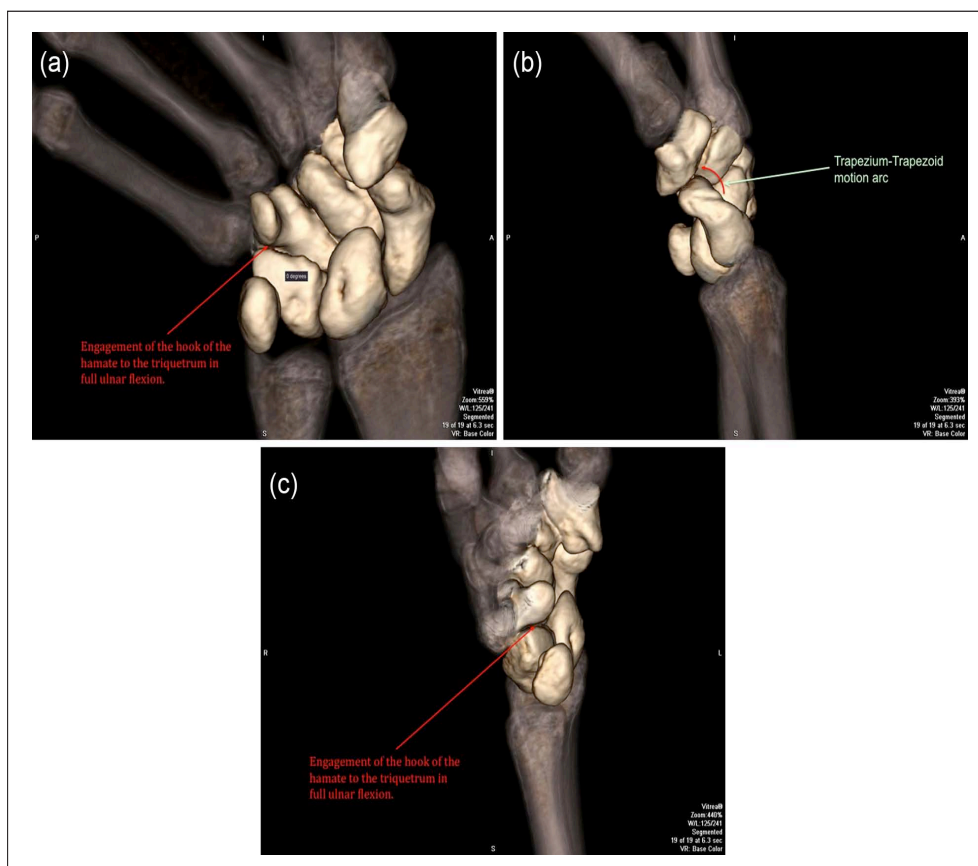


Figure 5. (a) View of the wrist in full ulnar flexion from an anterior to posterior view point. This view demonstrates the engagement of the hook of hamate with the distal triquetrum to limit further ulnar-flexion. (b) View of the wrist in full radial flexion from a radial to ulnar view point. This figure illustrates the trapezium trapezoid motion arc along the congruence of the dorsal distal scaphoid. (c) View of the wrist in full ulnar flexion from a distal to proximal view point. This view demonstrates the engagement of the hook of hamate with the triquetrum to limit further ulnar flexion.

methods (Moritomo et al., 2004; 2007; Savelberg et al., 1993). Observation of taped video may not have allowed detection of such small range of inter-bone motion in the distal carpal row in our study.

3. The proximal row (scaphoid, lunate, and triquetrum) is loosely held. We observed toggle behaviour of the carpal bones in the DTM pathway. We speculate that this adds tolerance to morphological irregularities and subtle deviations from the DTM pathway.
4. Mathematical derivation of the axis of rotation of DTM is possible and can be described relative to the radial shaft.

Vitrea software gave us the ability to manipulate the 3D camera viewpoint, which allowed observations of carpal bones from unconventional angles. In particular, use of these unconventional viewpoints allowed

for direct visualization of the trapezium-trapezoid key with the waist of the scaphoid at full radial extension (Figure 4d). We also observed the concave distal ridge of the hamate guiding the triquetrum toward the hook of hamate until it is fully engaged. This engagement of the hook of hamate with the triquetrum appeared to limit further ulnar flexion of the wrist, which is consistent with the findings of Kamal et al. (2012).

The software we used allowed virtual marker application to topographical landmarks on carpal bones and mathematical calculations to describe carpal motion. With identification of three reference points on the distal radius and its relationship to two landmarks on the poles of the capitate, we were able to mathematically derive the axis of rotation of DTM. This axis was mathematically derived to lie in 27° of anteversion from the coronal plane (62° from the sagittal plane) and 44° varus angulation.

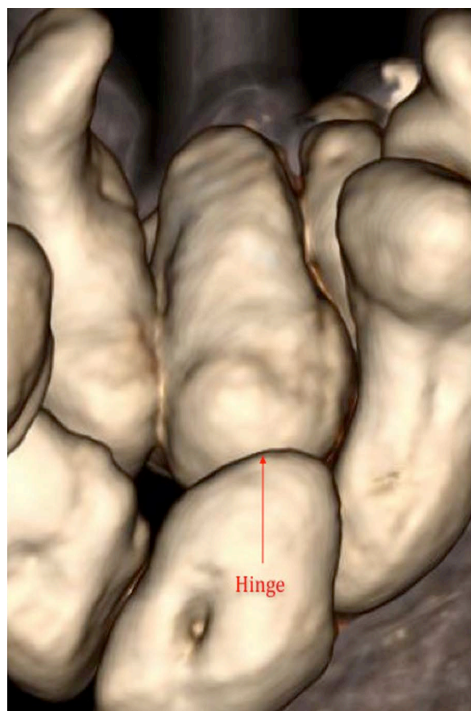


Figure 6. Lunate-capitate hinge.

We did find variability in the DTM pathway amongst the seven volunteers. Bone morphology, variations in ligamentous insertions, and manual landmark identification on the bones using the Vitrea console could all have contributed to this variation.

The intention of this study was to simulate and study natural dynamic DTM. This posed a considerable challenge in the standardization and definition of the start and end positions of DTM. It is acknowledged that there have been many recent studies analyzing components of DTM using goniometric boundaries (Bugden, 2013; Tang et al., 2011). Tang et al. have done ligament length analyses based on the definition of DTM as the wrist motion arc from the position of 20° radial deviation 60° extension to 40° ulnar deviation and 60° flexion (Tang et al., 2011). In this study we analyzed DTM in a different way, which did not utilize goniometric boundaries. We defined the start position of DTM as the wrist position of congruent articulation of the trapezoid and the end position of DTM as the engagement of the hook of hamate to the triquetrum. We acknowledge that the wrists show DTM movement beyond these boundaries into further radial-extension or ulnar-flexion. These movements beyond our defined end points demonstrated a large degree of variability due to the biological properties of the multiple joints involved in this motion. From our repeat scanning and observations, we noted that the

behaviour of the carpal bones remained consistent between the two end points defined in this study.

However, in our limited study the extended end points of DTM were largely variable due to effort-dependent confounding effects. We noted that the start and end points of DTM could not be defined by a particular angle, as this was noted to vary based on how much effort the subject puts into radial extension/ulnar flexion. Hence, goniometric measurements were not used to define the start and end points of DTM in this study. The most consistent/uniform motion in DTM was noted to lie between the articulation of the trapezium/scaphoid in radial extension to the first point of engagement of the hook of hamate with the triquetrum in ulnar flexion. Thus, the axis of rotation between these two points was calculated as it is the most mathematically appropriate description for this motion model. This calculation provided an accurate direction of motion irrespective of the start and end position of the wrist. Currently, other studies that can be used for comparison remain limited.

We must acknowledge the limitations of this study. This study had to rely on manual topographical landmark identification on each wrist scan of the seven volunteers. Meticulous care was taken to apply markers consistently to the desired landmarks. However, minute measurement error cannot be excluded, which can translate into minute error in calculating the axis of rotation. This was a limited study of seven subjects. A larger scale study with a wider demographic would have been useful in performing a statistical analysis on the variability of the axis of rotation and making observations regarding outlier wrists. This study utilized 4D CT, which is an imaging modality yet to be widely available. Therefore, the availability of this technology for routine wrist analysis currently remains limited. As mentioned earlier, it is important to acknowledge that “no movement”, the general finding based on video observation, may not be a true absence of motion. Observation of captured video may not allow detection of small interbone motion in distal carpal row. We could not provide exact data of interbone motion except descriptive statement of general motion patterns.

Nonetheless, with increasing availability of dynamic volume scanning technology, the methods described in this study may be of great significance. Many carpal pathologies are difficult to diagnose and the pathomechanics are poorly understood. Dynamic assessment using novel technology may be helpful to assess complex pathologies and underlying mechanism.

Conflicts of interests

None to declare.

Funding

This research received no specific grant from any funding agency in the public, commercial, or not-for-profit sectors.

References

- Alta TD, Bell SN, Troupis JM, Coghlan JA, Miller D. The new 4-dimensional computed tomographic scanner allows dynamic visualization and measurement of normal acromioclavicular joint motion in an unloaded and loaded condition. *J Comput Assist Tomogr.* 2012, 36: 749–54.
- Arkless R. Cineradiography in normal and abnormal wrists. *Am J Roentgenol Radium Ther Nucl Med.* 1966, 96: 837–44.
- Berger RA, Crowninshield RD, Flatt AE. The three-dimensional rotational behaviors of the carpal bones. *Clin Orthop Relat Res.* 1982, 167: 303–10.
- Brigstocke GHO, Hearnden A, Holt C, Whatling G. In-vivo confirmation of the use of the dart thrower's motion during activities of daily living. *J Hand Surg Eur Vol.* 2012 (epub).
- Bugden B. A proposed method of goniometric measurement of the dart-throwers motion. *J Hand Ther.* 2013, 26: 77–80.
- Charles M. UNSCEAR report 2000: Sources and effects of ionizing radiation. United Nations Scientific Committee on the Effects of Atomic Radiation. *J Radiol Prot.* 2001, 21: 83–5.
- Deák Z, Grimm JM, Treitl M et al. Filtered back projection, adaptive statistical iterative reconstruction, and a model-based iterative reconstruction in abdominal CT: an experimental clinical study. *Radiology.* 2012, 266: 197–206.
- Garcia-Elias M. The non-dissociative clunking wrist: a personal view. *J Hand Surg Eur Vol.* 2008, 33: 698–711.
- Garcia-Elias M, Alomar Serrallach X, Monill Serra J. Dart-throwing motion in patients with scapholunate instability. A dynamic four-dimensional computed tomography study. *J Hand Surg Eur Vol.* 2013 (epub).
- Ishikawa K, Cooney WP, Neibur G, An KN, Minami A, Kaneda K. The effects of wrist distraction on carpal kinematics. *J Hand Surg Am.* 1999, 24: 112–20.
- Kamal RN, Rainbow MJ, Akelman E, Crisco JJ. In vivo triquetrum-hamate kinematics through a simulated hammering task wrist motion. *J Bone Joint Surg Am.* 2012, 94: e85.
- Kulkarni NM, Uppot RN, Eisner BH, Sahani DV. Radiation dose reduction at multidetector CT with adaptive statistical iterative reconstruction for evaluation of urolithiasis: how low can we go? *Radiology.* 2012, 265: 158–66.
- Linscheid RL, Dobyns JH, Beabout JW, Bryan RS. Traumatic instability of the wrist. Diagnosis, classification, and pathomechanics. *J Bone Joint Surg Am.* 1972, 54: 1612–32.
- Manolakis DE. Efficient solution and performance analysis of 3D position estimation by trilateration. *Aerospace and Electronic Systems.* 1996, 32: 1239–48.
- Moojen TM, Snel JG, Ritt MJ, Venema HW, Kauer JM, Bos KE. In vivo analysis of carpal kinematics and comparative review of the literature. *J Hand Surg Am.* 2003, 28: 81–7.
- Moritomo H, Murase T, Goto A, Oka K, Sugamoto K, Yoshikawa H. Capitate-based kinematics of the midcarpal joint during wrist radioulnar deviation: an in vivo three-dimensional motion analysis. *J Hand Surg Am.* 2004, 29A: 668–75.
- Moritomo H, Apergis EP, Herzberg G, Werner FW, Wolfe SW, Garcia-Elias M. 2007 IFSSH committee report of wrist biomechanics committee: biomechanics of the so-called dart-throwing motion of the wrist. *J Hand Surg Am.* 2007, 32: 1447–53.
- Moritomo H, Murase T, Oka K, Tanaka H, Yoshikawa H, Sugamoto K. Relationship between the fracture location and the kinematic pattern in scaphoid nonunion. *J Hand Surg Am.* 2008, 33: 1459–68.
- Rohde RS, Crisco JJ, Wolfe SW. The advantage of throwing the first stone: how understanding the evolutionary demands of *Homo sapiens* is helping us understand carpal motion. *J Am Acad Orthop Surg.* 2010, 18: 51–8.
- Romagnoli A, Funel V, Meschini A et al. Optimisation of low-dose CT with adaptive statistical iterative reconstruction in total body examination. *Radiol Med.* 2012, 117: 1333–46.
- Ruby LK, Cooney WP, An KN, Linscheid RL, Chao EY. Relative motion of selected carpal bones: a kinematic analysis of the normal wrist. *J Hand Surg Am.* 1988, 13: 1–10.
- Savelberg HH, Otten JD, Kooloos JG, Huiskes R, Kauer JM. Carpal bone kinematics and ligament lengthening studied for the full range of joint movement. *J Biomech.* 1993, 26: 1389–402.
- Singh S, Kalra MK, Do S et al. Comparison of hybrid and pure iterative reconstruction techniques with conventional filtered back projection: dose reduction potential in the abdomen. *J Comput Assist Tomogr.* 2012, 36: 347–53.
- Tang JB, Xiao KG, Jing X, Juan HG. In vivo length changes of carpal ligaments of the wrist during dart-throwing motion. *J Hand Surg Am.* 2011, 36: 284–90.
- Werner FW, Green JK, Short WH, Masaoka S. Scaphoid and lunate motion during a wrist dart throw motion. *J Hand Surg Am.* 2004, 29: 418–22.
- Wolfe SW, Crisco JJ, Orr CM, Marzke MW. The dart-throwing motion of the wrist: is it unique to humans? *J Hand Surg Am.* 2006, 31: 1429–37.
- Wolfe SW, Gupta A, Crisco JJ. Kinematics of the scaphoid shift test. *J Hand Surg Am.* 1997, 22: 801–6.
- Wolfe SW, Neu CP, Crisco JJ. In vivo scaphoid, lunate and capitate kinematics in wrist flexion and extension. *J Hand Surg Am.* 2000, 25: 860–9.
- Yamada Y, Jinzaki M, Hosokawa T et al. Dose reduction in chest CT: comparison of the adaptive iterative dose reduction 3D, adaptive iterative dose reduction, and filtered back projection reconstruction techniques. *Eur J Radiol.* 2012, 81: 4185–95.
- Yoon MA, Kim SH, Lee JM et al. Adaptive statistical iterative reconstruction and Veo: assessment of image quality and diagnostic performance in CT colonography at various radiation doses. *J Comput Assist Tomogr.* 2012, 36: 596–601.
- Young RW. Evolution of the human hand: the role of throwing and clubbing. *J Anat.* 2003, 202: 165–74.

CHAPTER 7:**Four-dimensional Computed Tomography and****Trigger Lunate Syndrome**

Clunking of the wrist can be the result of a combination of radiocarpal and mid carpal ligament insufficiency, coupled with inadequate neuromuscular coordination[61]. Under load-bearing conditions, any bone tends to rotate into a specific direction depending on several factors, including the position of the wrist and the time of loading, the direction of the forces being transferred, and the inclination and shape of the articular surfaces on which the bone stands[62].

When the clunking derives from an isolated injury of one joint, ligament reconstruction may be an effective solution. However the traditional concept is that wrist instability is a primary feature of wrist clunking.

We considered the issue of 4D CT and whether the detection of motion disorders may yield further information with regard to wrist clunking. In particular, we were interested in whether impingement of any one of the carpal bones may be present in this clinical setting.

Impingement has been previously difficult to investigate which may potentially reflect the lack of consideration in the setting of wrist clunking.

The final published paper investigates whether wrist impingement may potentially exist and possibly co exist with wrist instability. The reclassification of mid carpal instability to include the presence or absence of impingement of one or more of the carpal bones may need consideration.

Declaration for Thesis Chapter SEVEN

Declaration by candidate

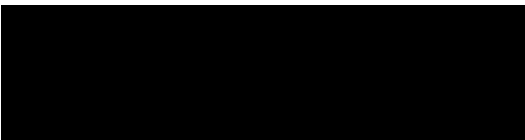
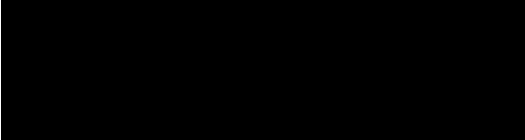
In the case of Chapter Seven, the nature and extent of my contribution to the work was the following:

| Nature of contribution | Extent of contribution (%) |
|--|----------------------------|
| Creation of idea, development of structure of the retrospective analysis, primary authorship | 70 |

The following co-authors contributed to the work. If co-authors are students at Monash University, the extent of their contribution in percentage terms must be stated:

| Name | Nature of contribution | Extent of contribution (%) for student co-authors only |
|---------------|------------------------------------|--|
| Benjamin Amis | Assisted with workstation analysis | Not a University student |
| | | |
| | | |

The undersigned hereby certify that the above declaration correctly reflects the nature and extent of the candidate's and co-authors' contributions to this work*.

| | | |
|---------------------------------|---|---------------------|
| Candidate's Signature |  | Date 12 Nov 2013 |
| Head of Department's Signature* |  | Date 12/11/13 |

CASE REPORT

Four-dimensional Computed Tomography and Trigger Lunate Syndrome

John M. Troupis, MBBS, FRANZCR,* and Benjamin Amis, MD†

Background: A 22-year-old man with no history of trauma and normal plain films, ultrasound, and magnetic resonance imaging presents with several months of increasingly severe pain and clicking in the right wrist. He is clinically diagnosed with midcarpal instability and undergoes a 4-dimensional computed tomography scan of his wrist for further evaluation. **Methods:** The motion of the subject's lunate was evaluated through a full arc of flexion and extension as well as radial and ulnar deviation. A comparison was made with the lunate of an asymptomatic patient demonstrating the same motions.

Results: The symptomatic lunate demonstrated early smooth motion, followed by cessation of motion, and then again followed by smooth catch up motion. The asymptomatic patient demonstrated smooth lunate motion throughout the study.

Discussion: The lunate motion, with an abrupt cessation and commencement of flexion/extension, was consistent with a triggering phenomenon. This trigger lunate motion abnormality, although consistent with the "clunking" sensation often described during the physical examination, has not been previously recognized radiographically as a feature of midcarpal instability.

Key Words: 4D CT, midcarpal instability, trigger lunate syndrome

(*J Comput Assist Tomogr* 2013;37: 639–643)

A 22-year-old man with no history of trauma presents with several months of increasingly severe pain and clicking in the right wrist. Plain film radiography, ultrasound, and magnetic resonance imaging examinations demonstrate largely unremarkable appearance, without evidence of joint space disturbance or tendon or other superficial tissue abnormalities, and normal intrinsic and extrinsic ligaments of the wrist and midcarpal region. The provisional clinical diagnosis was midcarpal instability syndrome. We further investigated this condition with the assistance of a wide volume detector computed tomography (CT) scanning (4-dimensional CT [4D CT]) technique.

METHODS

The patient was asked to undergo a 4D CT scan of his symptomatic wrist to analyze the clinically diagnosed midcarpal instability. Data from a previously scanned asymptomatic wrist were utilized as a comparison for this study.

The CT scan was performed using 320×0.5 -mm multi-detector CT (Aquilion One Toshiba Medical Systems, Otawara-shi, Tochigi-ken, Japan). Because of the wide z axis scan volume of 16 cm (proximal to distal) and gantry rotation speed of

350 milliseconds, we were able to acquire approximately 6 volume data sets per second (each volume data second can be acquired in half an x-ray tube rotation). Because we performed a volumetric acquisition, no table movement was necessary.

The patient was coached by the imaging technologist to perform similar motions of both wrists (symptomatic and asymptomatic) in the CT scanner consisting of full wrist flexion/extension and radial/ulnar deviation. The CT scans were captured, and 4D motion reconstructions in the traditional axial, sagittal, and coronal planes were created. The data set was examined specifically for the position of the hand and the radiolunate angle during each arc from full extension to flexion and from full ulnar to radial deviation. The radiolunate angle was determined by drawing a line connecting the 2 poles of the lunate on a sagittal image and then drawing a line perpendicular to this. The angle between this line and a line drawn along the axis of the radius defined the radiolunate angle. The position of the hand was determined by drawing a line along the axis of



FIGURE 1. To determine the radiolunate angle, a line is drawn that connects the 2 poles of the lunate on a sagittal image, and then a new line is drawn that is perpendicular to this. The angle between this line and a line drawn along the long axis of the radius through to the third metacarpal defines the radiolunate angle.

From the *Department of Diagnostic Imaging, Monash Medical Centre, Melbourne, Australia; and †CV Starr Hand Surgery Center, New York, NY. Received for publication January 31, 2013; accepted February 4, 2013. Reprints: Benjamin Amis, MD, CV Starr Hand Surgery Center, 3rd Floor, Roosevelt Hospital, 1000 10th Ave at 58th St, New York, NY 10019

The authors report no conflicts of interest.
Copyright © 2013 by Lippincott Williams & Wilkins

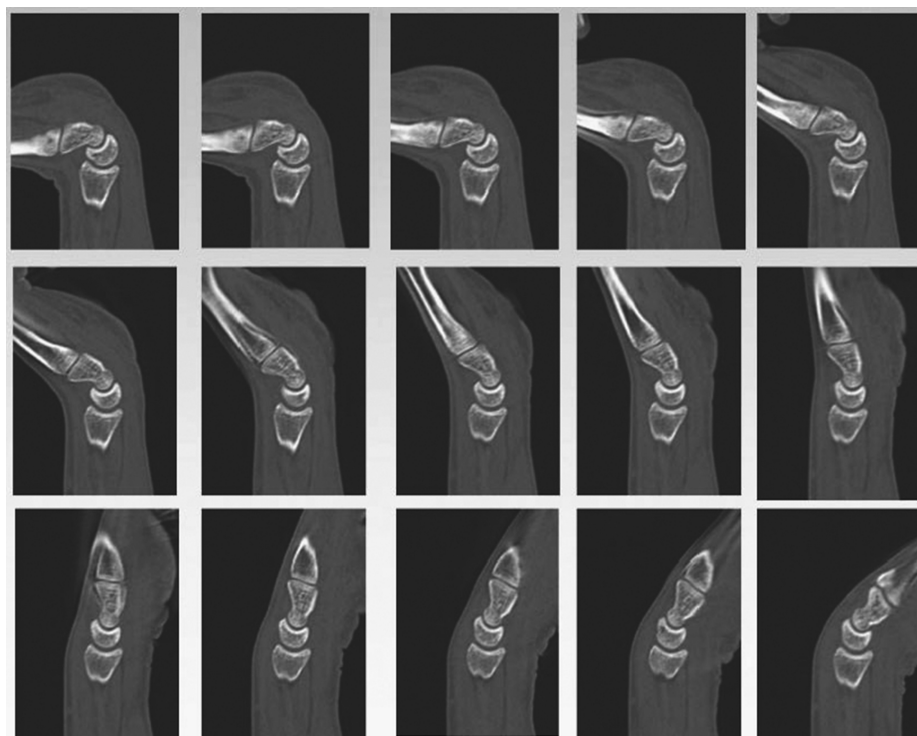


FIGURE 2. A series of sagittal images of the asymptomatic wrist reconstructed through the midlunate during the motion of hand extension through to hand flexion from which subsequent angles are obtained.

the capitate and third metacarpal and comparing this to a line drawn along the axis of the radius (Fig. 1). Each reconstructed image is labeled with a phase time allowing for measurement taken on different spatial reconstructions to be correlated by phase (as the wrist is not centered within the image volume,

automated analysis is not possible). All analysis was performed on OsiriX DICOM Viewer.

The results were then plotted on a simple line graph. The x axis on the graph represents phases (each image of acquisition represents an individual phase). The arc of radiolunate angle

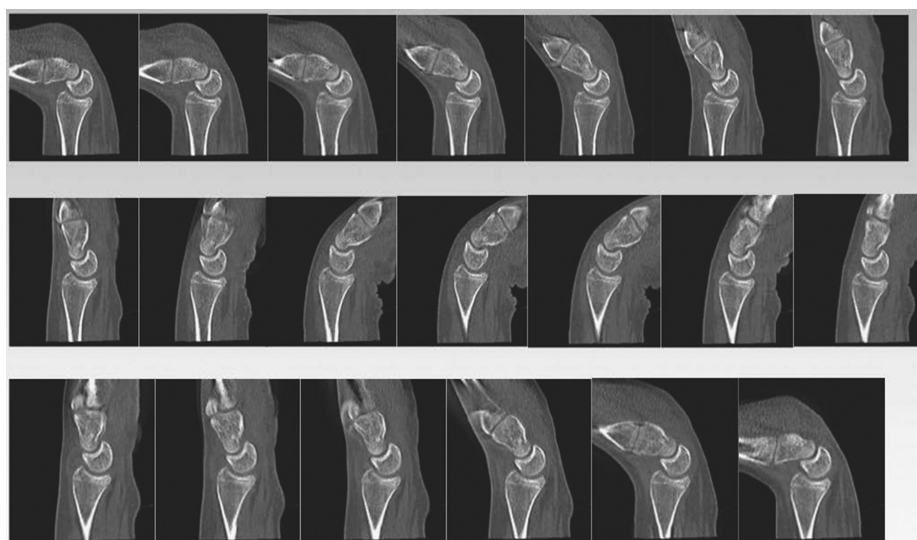


FIGURE 3. A series of sagittal images of the symptomatic wrist reconstructed through the midlunate during the motion of hand extension through to hand flexion and back to hand extension.

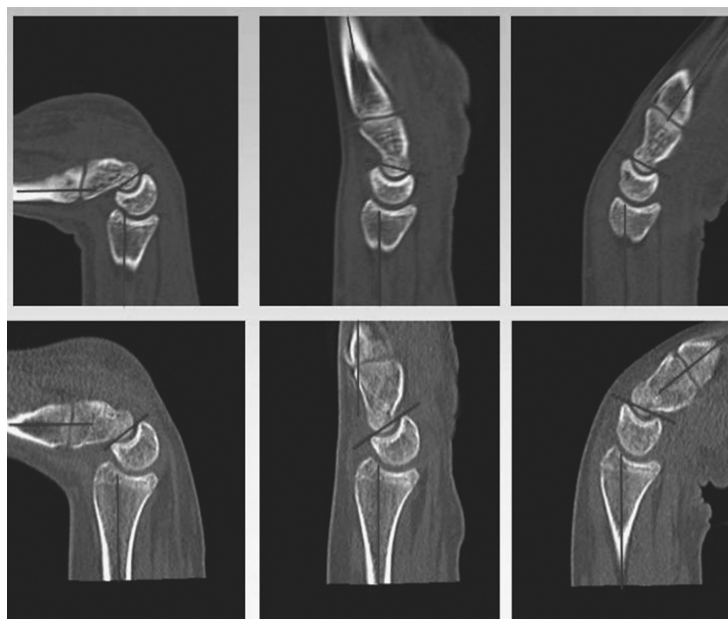


FIGURE 4. A series of representative images highlighting the delayed flexion of the abnormal wrist (bottom row) when compared with the normal wrist (top row) with both hands in a neutral position. The middle image of both rows best demonstrates the delayed lunate flexion with hand in neutral.

was plotted on each graph to allow for objective comparison between the symptomatic and asymptomatic carpus.

The effective radiation exposure was calculated using the dose-length product (DLP) and multiplying this with an organ specific conversion factor (0.0001).

RESULTS

Figures 2 and 3 are a series of sagittal images of the asymptomatic and symptomatic wrists respectively, demonstrating the position of the lunate in each phase.

Figure 4 (normal wrist top row, abnormal wrist bottom row) is a series of representative images highlighting the delayed flexion of the abnormal wrist when both hands are in a neutral position.

Assessment of all cine movie files revealed abnormal motion of the lunate in the sagittal projection when compared with the normal wrist. In our symptomatic patient, we noted that in both hand flexion/extension and ulnar/radial deviation, there was

a notable absence of smooth lunate transition from extension to flexion when compared with our normal control (Figs. 5–8). In particular, during the smooth arc of motion of the hand in both of these motions, the lunate demonstrated early smooth motion, followed by cessation of motion, and then again followed by smooth catch-up motion. Throughout the study, the symptomatic lunate demonstrated no evidence of subluxation, with the radial, capitate, and scaphoid articulations remaining congruent. In all imaging planes, including both volume-rendered and multiplanar imaging, no abnormality of either the lunate or other carpal bone configuration was identified.

The assessment of the normal lunate motion confirmed the expected normal motion extension with hand extension, flexion with hand flexion, flexion with radial deviation, and extension with ulnar deviation.

In our case of lunate motion assessment, each acquisition recorded DLP of approximately 410.7 mGy · cm, with total DLP of 1789.2 mGy · cm (includes all acquisitions and scouts),

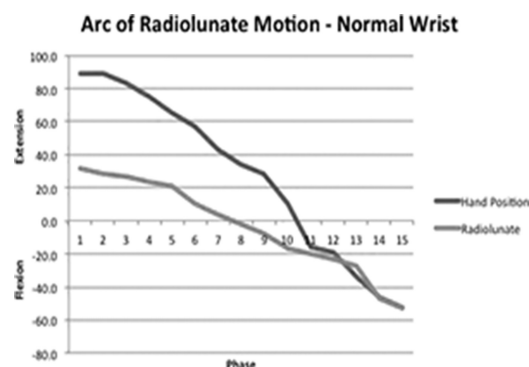


FIGURE 5. Arc of radiolunate motion of normal wrist—hand extension to flexion.

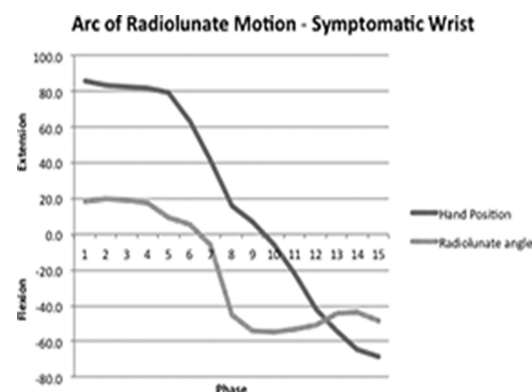


FIGURE 6. Arc of radiolunate motion of symptomatic wrist—hand extension to flexion.

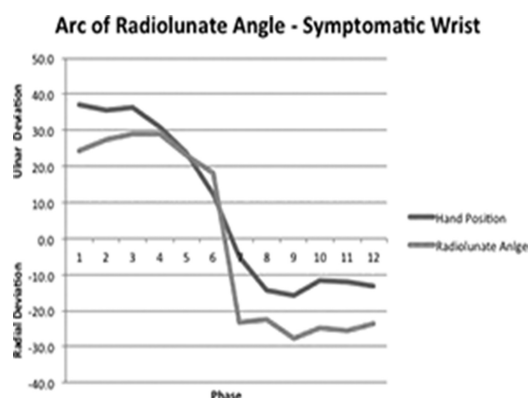


FIGURE 7. Arc of radiolunate motion of symptomatic wrist—hand ulnar to radial deviation.

resulting in effective radiation exposure of 0.05 mSv per CT acquisition and 0.18 mSv for the entire series (including scout images).

DISCUSSION

Midcarpal instability was first described by Mouchet and Belot¹ in 1934 using the term “snapping wrist.” Midcarpal instability syndrome typically presents with pain and clunking on wrist flexion/extension or ulnar/radial deviation.^{2–4} It is defined as a dysfunction between the 2 carpal rows in which there is no evidence of dissociation of the bones in a single carpal row and is classified as in the spectrum of carpal instabilities as indicated in Table 1.⁵ It requires disruption/dysfunction of the ligaments, which cross the midcarpal joint, such as the scaphocapitate, triquetro-hamate-capitate ligament, and, to a lesser extent, the scaphocapitate and scapho-trapezio-trapezoid ligaments. Whereas a wide variety of the clinical findings of midcarpal instability spectrum pathologies have been described, radiographic evidence of the underlying causes has been elusive because of the dynamic nature of the condition.

To evaluate for abnormal lunate motion, knowledge regarding the normal motion is paramount. The normal lunate tends to follow the wrist in flexion and extension. However, as the hand radially deviates, the distal carpal row pushes the distal scaphoid into flexion and the lunate follows due to the strong scapholunate ligament. As the hand ulnarly deviates, the lunate

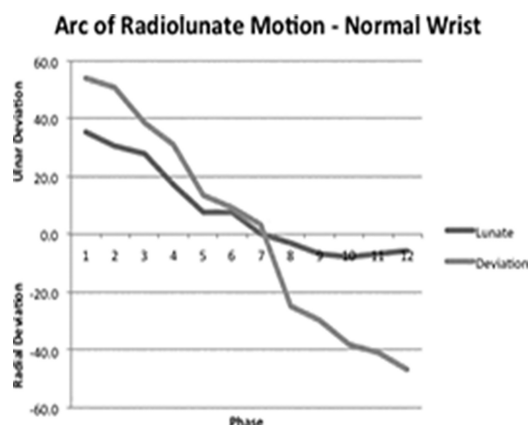


FIGURE 8. Arc of radiolunate motion of normal wrist—hand ulnar to radial deviation.

TABLE 1. Classification of Carpal Instabilities

| |
|--|
| I. Perilunate instabilities (carpal instability dissociative) |
| A. Lesser arc pattern |
| 1. Scapholunate instability |
| 2. Triquetrolunate instability |
| 3. Complete perilunate dislocation |
| B. Greater arc pattern |
| 1. Scaphoid fracture |
| a. Stable |
| b. Unstable (DISI) |
| 2. Naviculocapitate syndrome |
| 3. Transcapitoid transtriquetral perilunate dislocations |
| 4. Variations and combinations of points B1 through B3 |
| II. MCIs (midcarpal CIND) |
| A. Intrinsic (ligamentous laxity) |
| 1. Palmar MCI (VISI) |
| 2. Dorsal MCI (DISI) |
| 3. Combined |
| B. Extrinsic (dorsally displaced radial fracture) |
| III. Proximal carpal instabilities |
| A. Ulnar translocation of the carpus |
| B. Dorsal instability (after dorsal rim fracture—dorsal Barton fracture) |
| C. Palmar instability (after volar rim distal radial fracture—volar Barton fracture) |
| IV. Miscellaneous |
| A. Axial |
| B. Periscaphoid |

CIND indicates carpal instability non dissociative; DISI, dorsal intercalated segmental instability; MCIs, mid carpal instability; VISI: volar intercalated segmental instability.

and scaphoid rotate into extension through a combined effect of the interosseous ligaments and the coupled rotation of the distal row into a dorsally translated position.⁴

In our case study, we determined that the patient’s symptoms (pain and clunking on hand motion) were directly associated with abnormal lunate motion. The lunate motion, with an abrupt cessation and recommencement of flexion/extension, was consistent with a triggering phenomenon. This trigger lunate motion abnormality, although consistent with the “clunking” sensation often described during the physical examination, has not been previously recognized radiographically as a feature of midcarpal instability, which is classified according to instability and not impingement. We have been able to confidently identify triggering of the lunate both visually (assessment of the 3-dimensional volume-rendered video files) and objectively (documentation of the radius/lunate angle in comparison with hand position).

In the study of scapholunate (as opposed to midcarpal) instability, the concept of dynamic scaphoid instability and the use of stress radiographs to better identify “occult” carpal abnormalities that were not detectable on static images have been developed.³ More recently, sequential CT and magnetic resonance imaging in combination with complex computerized modeling have allowed for highly accurate analysis of carpal anatomy and kinematics.^{6–10} However, these techniques are limited by their use of segmental static images requiring computerized rendering, which may miss subtle shifts in position

and therefore may not accurately reflect dynamic processes. These techniques are also not readily available for everyday use in clinical diagnosis.

In this case, we have been able to utilize the unique properties of wide volume CT scan to detect motion disturbance of the lunate, which has not been previously reported as a feature of midcarpal instability and which may, in our view, define a specific condition previously generalized under the wide spectrum of midcarpal instability spectrum conditions.

CONCLUSIONS

By using 4D CT to further assess lunate motion in the setting of the clinical condition, midcarpal instability syndrome, we have been able to detect abnormal lunate motion, which has a trigger-type pattern. Our findings present evidence for the existence of a previously unrecognized condition, trigger lunate syndrome, which, to our knowledge, has not been previously reported and which would appear to either mimic lunare instability or, more than likely, be a unique feature of patients who present with midcarpal instability.

We propose that 4D CT should be used to further investigate all functional carpal instability syndromes as this technique has the potential to add significantly to our knowledge carpal bone motion abnormalities.

ACKNOWLEDGMENTS

The authors thank Jacqui Hislop and Marcus Crossett for their support with the use of the Toshiba 4D CT scanner.

REFERENCES

1. Mouchet A, Belot J. Poignet a ressaut (subluxation médiocarpienne en avant). *Bull Mem Soc Natl Chir.* 1934;60:1243–1244.
2. Linscheid RL, Dobyns JH, Beabout JW, et al. Traumatic instability of the wrist. Diagnosis, classification, and pathomechanics. *J Bone Joint Surg Am.* 1972;54:1612–1632.
3. Watson H, Ottoni L, Pitts E, et al. Rotary subluxation of the scaphoid : a spectrum of instability. *J Hand Surg Br.* 1993;18:62–64.
4. Kuo CE, Wolfe SW. Scapholunate instability: current concepts in diagnosis and management. *J Hand Surg Am.* 2008;33:998–1013.
5. Lichtman DM, Wroten ES. Understanding midcarpal instability. *J Hand Surg Am.* 2006;31:491–498.
6. Crisco JJ, Wolfe SW, Neu CP, et al. Advances in the in vivo measurement of normal and abnormal carpal kinematics. *Orthop Clin North Am.* 2001;32:219–231, vii.
7. Moojen TM, Snel JG, Ritt MJPF, et al. Three-dimensional carpal kinematics in vivo. *Clin Biomech (Bristol, Avon).* 2002;17:506–514.
8. Crisco JJJ, McGovern RDR, Wolfe SWS. Noninvasive technique for measuring in vivo three-dimensional carpal bone kinematics. *J Orthop Res.* 1998;17:96–100.
9. Neu CPC, Crisco JJJ, Wolfe SWS. In vivo kinematic behavior of the radio-capitate joint during wrist flexion-extension and radio-ulnar deviation. *J Biomech.* 2001;34:1429–1438.
10. Majors BJ, Wayne JS. Development and validation of a computational model for investigation of wrist biomechanics. *Ann Biomed Eng.* 2011;39:2807–2815.

DISCUSSION/CONCLUSION

The technical innovation of wide field of view CT has allowed medical imaging to approach the imaging of human anatomy both from a physiological and also from a morphological motion perspective. It is now possible to examine numerous portions of clinically significant tissues at the same point in time, thereby accurately assessing for physiological disturbances. Two organs where this is of acute importance are the brain and heart.

With regard to coronary artery CT, wide field of view CT has allowed an exception to the traditional concept of a requirement to have patient's heart rate below the temporal resolution of the CT unit. We demonstrated that due to capability of volume acquisition, and due to the absence of multisegment reconstruction, diagnostic quality coronary artery images are possible should the patient's heart rate be higher than the CT temporal resolution. This has previously not been possible as the temporal resolution of the CT unit was considered a limiting factor with regard to obtaining diagnostic coronary artery CT.

We have demonstrated the significant advance of wide field of view CT with regard to acute brain perfusion in patients assessed clinically as possibly suffering from cerebrovascular infarction and who may be considered, optimally, for acute thrombolytic therapy as part of the acute stroke management of a tertiary medical institution. As the exact site of perfusion anomaly may be clinically difficult to isolate, the advantage of wide field of view CT is of a significant increase in coverage of neurological tissue, in particular including the brain stem together with the cerebrum and portions of the cerebellum at the same time. We have demonstrated that there may be significant advantages for the patient when the perfusion assessment is performed with wide field of view CT. In addition, the increased z axis coverage makes possible the rapid repeat acquisition of the entire field of view due to the static and not helical acquisition, with contrast continuing to perfuse through the tissue. By performing contrast perfusion with rapid repeat scanning, "real-time" angiography may potentially be

achieved, approaching the diagnostic yield of catheter digital subtraction angiography. This may have the potential impact of limiting catheter digital subtraction angiography to the therapeutic arena. This focus of brain perfusion with wide field of view CT requires further exploration. Our paper has introduced an insight into the different acquisition principles, which should be a catalyst for further investigations.

Myocardial perfusion is considered the “holy grail” of cardiac imaging. The ability to assess the perfusion of myocardium, at one moment in time, with the concurrent assessment of coronary arteries, which may or may not be subject to obstructive coronary artery disease, has been subject to much investigation. Wide field of view CT has allowed the assessment of myocardial density throughout the heart at the same time point, thereby negating the influence of density depending on the timing of contrast administration. Due to inherent nature of coronary artery CT, examination of the whole heart at the same time has not been previously possible. We examined the myocardial density in normal myocardium, and determined that the posterolateral myocardium demonstrates a lower density than the remainder of the myocardium, which shows similar density profile. This phenomenon cannot be attributed to differences in the myocardial position in relation to contrast timing as the examination is performed at all positions of the heart at the same time point. We have therefore confirmed this “difference” in myocardial densities as likely due to structural phenomenon, independent of contrast. This finding allowed us to further examine the influence of clinically significant ischaemia on myocardial segmental densities. We aimed to examine myocardial segments at the same time point in both the non-ischaemic and ischaemic clinical setting. We determined that no statistically significant difference between the segments subject to ischaemia could be identified. Having determined the absence of statistically significant myocardial density change in ischaemia in the rest state, our findings have provided a significant baseline for further investigations. In particular further investigations may now consider the influence of timing of contrast perfusion, contrast

density and volume modification, and the possible detection of ischaemia induced myocardial segmental density reduction either in the early dynamic perfusion assessment or possible detection of hyperdensity in the delayed phase due to abnormal tissue pharmacokinetics, as may be seen in cardiac MRI.

When considering wide field of view with rapid repeat acquisitions, the concept of 4 Dimensional Computer Tomography (4D CT) is introduced. We investigated 4D CT and considered the possible clinical impact in conditions where motion disorder is a dominant finding. In particular, we found that 4D CT has significant clinical utility in musculoskeletal imaging where clinical conditions related to instability, impingement or tethering have been difficult to investigate due to their “dynamic” abnormalities whilst otherwise maintaining unremarkable morphological appearances.

We commenced investigations with the normal acromion-clavicular (AC) joint and identified the pattern of normal joint motion during adduction of the arm, both with and without resisted superior elevation. The exact motion of the AC joint was previously not defined in real time with cross sectional imaging, with the motion assessment limited to real time imaging without cross sectional capabilities such as ultrasonography.

We determined that in arm adduction with resisted elevation, the main movement of the AC joint is posterior and superior translation of the clavicle. A further finding was confirmation that AC joint flexibility reduces with age, which may explain the difference between expected clinical outcome of younger versus older patients in the setting of distal clavicular excision.

One of the more complex joints which is least understood is the wrist and associated intercarpal joints. It is well established that the dart throwers motion is the index motion which best defines the complexity of motion within the carpus. As the knowledge of the intercarpal motions is limited to either cadaveric research, invivo surgical exploration or dynamic non cross-sectional fluoroscopy, we used 4D CT combined with a dynamic 3

Dimensional (3D) mapping method to model the normal wrist in dart throwers motion. By applying a 3D coordinate system and 3D volume rendered reconstructions in multiple motion phases, we observed the motion pathways of all carpal bones and calculated the overall axis of rotation of the motion, which we found to be in 27 degrees of anterversion from the coronal plane, and 44 degrees of varus angulation relative to the transverse plane. The findings have significant implications with regard to wrist and intercarpal surgery. Future hand surgical and rehabilitative practices may benefit from this knowledge.

As our first two 4D CT musculoskeletal imaging investigations yielded significant increase in knowledge of the normal motion of the AC and wrist joints, we then considered the issue of clinical utility in motion disorders. One of the least understood motion disorders is mid carpal instability where patients may present with significant morbidity with unremarkable imaging, requiring exploratory surgery. Our investigation of mid carpal instability yielded a unique insight into the motion of the lunate with respect to both the radius (at the proximal articular surface) and the capitate (at the distal articular surface). We were able to report on a previously unknown clinical entity, that of lunate impingement. We noted that the normal lunate demonstrates a smooth motion from volar to dorsal extension and back. However after carefully examining the sagittal motion of the lunate, we detected an abrupt change in angulation with catch up of the motion. We were intrigued as there had never been a recorded description of this triggering lunate. We postulate the trigger lunate syndrome most likely represents a subset of patients who otherwise present with clinical symptomatology consistent with mid carpal instability. To our knowledge, our report of the trigger lunate syndrome is the first recognition and is due to the functional utility of 4D CT. We propose that 4D CT may continue to yield further insight into the complexity of wrist motion disorders.

Wide field of view CT and, in particular, 4D CT have resulted in a significant increase in knowledge of both conditions which have been previously extensively investigated, and also conditions which have not been well understood. It is considered to be a unique opportunity

for further examination of organs which fluctuate in morphology and density and which routine CT is able to provide limited information.

Further work to investigate both brain and heart is considered crucial especially in the regions of brain death, cerebral perfusion, vascular anomalies and myocardial perfusion. However further work is likely to yield a greater understanding of joint disorders, especially pertaining to instability and impingement.

We suggest that spinal instability in the setting of cervical facet joint osteoarthritis and lumbar spine listhesis (either due to facet joint osteoarthritis or pars inter articularis defects) may also benefit from 4D CT with an ability to possibly further categorize the severity of the underlying pathology by the severity of secondary instability.

Further consideration for 4D CT utility is that of tethering of tissues, which may be of clinical relevance. Areas of interest may include lung carcinoma and possible chest wall or vascular invasion. Differential motion of the carcinoma and the adjacent tissues can be expected during inspiration and expiration. Furthermore, redo sternotomy does have a small but significant mortality risk. Consideration toward 4D CT and the assessment of differential motion between the anterior cardiac/vascular structures and the posterior sternum in the midline may yield results relevant to the managing surgeon, who may elect to modify sternotomy technique.

The technical innovations of wide field of view CT and 4D CT have provided a unique opportunity into further understanding both the normal and also the abnormal human organ.

REFERENCES/BIBLIOGRAPHY

1. Ambrose J, Hounsfield G. Computerized transverse axial tomography. *The British journal of radiology* 1973; 46:148-149
2. Hounsfield GN. Computerized transverse axial scanning (tomography). 1. Description of system. *The British journal of radiology* 1973; 46:1016-1022
3. Beckmann EC. CT scanning the early days. *The British journal of radiology* 2006; 79:5-8
4. Brooks RA, Di Chiro G. Principles of computer assisted tomography (CAT) in radiographic and radioisotopic imaging. *Physics in medicine and biology* 1976; 21:689-732
5. Kalender WA, Seissler W, Klotz E, Vock P. Spiral volumetric CT with single-breath-hold technique, continuous transport, and continuous scanner rotation. *Radiology* 1990; 176:181-183
6. Hu H. Multi-slice helical CT: scan and reconstruction. *Medical physics* 1999; 26:5-18
7. Ropers D, Baum U, Pohle K, et al. Detection of coronary artery stenoses with thin-slice multi-detector row spiral computed tomography and multiplanar reconstruction. *Circulation* 2003; 107:664-666
8. Nikolaou K, Flohr T, Knez A, et al. Advances in cardiac CT imaging: 64-slice scanner. *The international journal of cardiovascular imaging* 2004; 20:535-540
9. Hsiao EM, Rybicki FJ, Steigner M. CT coronary angiography: 256-slice and 320-detector row scanners. *Current cardiology reports* 2010; 12:68-75
10. Mather R. Multislice CT: 64 slices and beyond. *Radiology management* 2005; 27:46-48, 50-42
11. Taguchi K. Temporal resolution and the evaluation of candidate algorithms for four-dimensional CT. *Medical physics* 2003; 30:640-650

12. Moorrees J, Bezak E. Four dimensional radiotherapy: a review of current technologies and modalities. *Australasian physical & engineering sciences in medicine / supported by the Australasian College of Physical Scientists in Medicine and the Australasian Association of Physical Sciences in Medicine* 2012; 35:399-406
13. Otto K. Volumetric modulated arc therapy: IMRT in a single gantry arc. *Medical physics* 2008; 35:310-317
14. Nakagawa K, Kida S, Haga A, et al. 4D digitally reconstructed radiography for verifying a lung tumor position during volumetric modulated arc therapy. *Journal of radiation research* 2012; 53:628-632
15. Chin E, Loewen SK, Nichol A, Otto K. 4D VMAT, gated VMAT, and 3D VMAT for stereotactic body radiation therapy in lung. *Physics in medicine and biology* 2013; 58:749-770
16. Sahiner L, Canpolat U, Aytemir K, et al. Diagnostic accuracy of 16- versus 64-slice multidetector computed tomography angiography in the evaluation of coronary artery bypass grafts: a comparative study. *Interactive cardiovascular and thoracic surgery* 2012; 15:847-853
17. Cademartiri F, Runza G, Belgrano M, et al. Introduction to coronary imaging with 64-slice computed tomography. *La Radiologia medica* 2005; 110:16-41
18. Sodhi JS, Zargar SA, Rashid W, et al. 64-section multiphase CT enterography as a diagnostic tool in the evaluation of obscure gastrointestinal bleeding. *Indian journal of gastroenterology : official journal of the Indian Society of Gastroenterology* 2012; 31:61-68
19. Idris M, Kashif N, Idris S, Memon WA, Tanveer UH, Haider Z. Accuracy of 64-slice multidetector computed tomography scan in detection of the point of transition of small bowel obstruction. *Japanese journal of radiology* 2012; 30:235-241

20. Harrieder A, Geyer LL, Korner M, et al. [Evaluation of radiation dose in 64-row whole-body CT of multiple injured patients compared to 4-row CT]. *RoFo : Fortschritte auf dem Gebiete der Rontgenstrahlen und der Nuklearmedizin* 2012; 184:443-449
21. Yang L, Huang X, Duan S. Clinical application and technique of 64-slice spiral CT subtraction angiography in head and neck. *VASA Zeitschrift fur Gefasskrankheiten* 2012; 41:27-33
22. Agid R, Lee SK, Willinsky RA, Farb RI, terBrugge KG. Acute subarachnoid hemorrhage: using 64-slice multidetector CT angiography to "triage" patients' treatment. *Neuroradiology* 2006; 48:787-794
23. Xu J, Liang Z, Hao S, et al. Pancreatic adenocarcinoma: dynamic 64-slice helical CT with perfusion imaging. *Abdominal imaging* 2009; 34:759-766
24. Wang XM, Wu LB, Sun C, et al. Clinical application of 64-slice spiral CT in the diagnosis of the Tetralogy of Fallot. *European journal of radiology* 2007; 64:296-301
25. Dewey M, Zimmermann E, Laule M, Rutsch W, Hamm B. Three-vessel coronary artery disease examined with 320-slice computed tomography coronary angiography. *European heart journal* 2008; 29:1669
26. Rybicki FJ, Otero HJ, Steigner ML, et al. Initial evaluation of coronary images from 320-detector row computed tomography. *The international journal of cardiovascular imaging* 2008; 24:535-546
27. Nasis A, Antonis PR, Seneviratne SK. 320-detector row cardiac computed tomography in the diagnosis of arrhythmogenic right ventricular cardiomyopathy. *Europace : European pacing, arrhythmias, and cardiac electrophysiology : journal of the working groups on cardiac pacing, arrhythmias, and cardiac cellular electrophysiology of the European Society of Cardiology* 2009; 11:1125-1126

28. Husmann L, Herzog BA, Burkhard N, et al. Body physique and heart rate variability determine the occurrence of stair-step artefacts in 64-slice CT coronary angiography with prospective ECG-triggering. *European radiology* 2009; 19:1698-1703
29. Fleischmann D, Rubin GD, Paik DS, et al. Stair-step artifacts with single versus multiple detector-row helical CT. *Radiology* 2000; 216:185-196
30. Singh A, Sethi Y, Watkins S, Youtsey A, Thomas A. Banding and Step-Stair Artifacts on the Cardiac-CT Caused By Pseudo-Ectopic Beats. *Journal of radiology case reports* 2009; 3:3-8
31. Mendis S. Stroke disability and rehabilitation of stroke: World Health Organization perspective. *International journal of stroke : official journal of the International Stroke Society* 2013; 8:3-4
32. Norrving B, Kissela B. The global burden of stroke and need for a continuum of care. *Neurology* 2013; 80:S5-12
33. Hoang JK, Wang C, Frush DP, et al. Estimation of Radiation Exposure for Brain Perfusion CT: Standard Protocol Compared With Deviations in Protocol. *AJR American journal of roentgenology* 2013; 201:W730-734
34. Oikawa K, Ogasawara K, Saito H, et al. Combined Measurement of Cerebral and Cerebellar Blood Flow on Preoperative Brain Perfusion SPECT Imaging Predicts Development of New Cerebral Ischemic Events After Endarterectomy for Symptomatic Unilateral Cervical Carotid Stenosis. *Clinical nuclear medicine* 2013; 38:957-961
35. Jolepalem P, Balon HR. The Role of Scintigraphy in Confirmation of Suspected Brain Death. *Journal of nuclear medicine technology* 2013;
36. Barbier EL, Lamalle L, Decorps M. Methodology of brain perfusion imaging. *Journal of magnetic resonance imaging : JMRI* 2001; 13:496-520
37. Takekawa T, Kakuda W, Uchiyama M, Ikegaya M, Abo M. Brain perfusion and upper limb motor function: A pilot study on the correlation between evolution of asymmetry

- in cerebral blood flow and improvement in Fugl-Meyer Assessment score after rTMS in chronic post-stroke patients. *Journal of neuroradiology Journal de neuroradiologie* 2013;
38. Page M, Nandurkar D, Crossett MP, et al. Comparison of 4 cm Z-axis and 16 cm Z-axis multidetector CT perfusion. *European radiology* 2010; 20:1508-1514
 39. Dorbala S, Giugliano RP, Logsetty G, et al. Prognostic value of SPECT myocardial perfusion imaging in patients with elevated cardiac troponin I levels and atypical clinical presentation. *Journal of nuclear cardiology : official publication of the American Society of Nuclear Cardiology* 2007; 14:53-58
 40. Kuikka JT. Myocardial perfusion imaging with a novel SPECT/CT system: all that glitters is not gold. *European journal of nuclear medicine and molecular imaging* 2007; 34:611-612
 41. Mahmarian JJ. The troponin conundrum: clarification through stress myocardial perfusion SPECT. *Journal of nuclear cardiology : official publication of the American Society of Nuclear Cardiology* 2007; 14:6-8
 42. Schwitter J. Myocardial perfusion imaging by cardiac magnetic resonance. *Journal of nuclear cardiology : official publication of the American Society of Nuclear Cardiology* 2006; 13:841-854
 43. Wang YN, Jin ZY, Zhang ZH, et al. Assessment of myocardial viability with contrast-enhanced magnetic resonance imaging and comparison with single-photon emission computed tomography. *Chinese medical sciences journal = Chung-kuo i hsueh k'o hsueh tsa chih / Chinese Academy of Medical Sciences* 2006; 21:239-244
 44. Husmann L, Wiegand M, Valenta I, et al. Diagnostic accuracy of myocardial perfusion imaging with single photon emission computed tomography and positron emission tomography: a comparison with coronary angiography. *The international journal of cardiovascular imaging* 2008; 24:511-518

45. Gaemperli O, Schepis T, Koepfli P, et al. Accuracy of 64-slice CT angiography for the detection of functionally relevant coronary stenoses as assessed with myocardial perfusion SPECT. *European journal of nuclear medicine and molecular imaging* 2007; 34:1162-1171
46. Greif M, von Ziegler F, Bamberg F, et al. CT stress perfusion imaging for detection of haemodynamically relevant coronary stenosis as defined by FFR. *Heart* 2013; 99:1004-1011
47. Huber AM, Leber V, Gramer BM, et al. Myocardium: Dynamic versus Single-Shot CT Perfusion Imaging. *Radiology* 2013; 269:378-386
48. Muenzel D, Kabus S, Gramer B, et al. Dynamic CT Perfusion Imaging of the Myocardium: A Technical Note on Improvement of Image Quality. *PloS one* 2013; 8:e75263
49. Koonce JD, Vliegenthart R, Schoepf UJ, et al. Accuracy of dual-energy computed tomography for the measurement of iodine concentration using cardiac CT protocols: validation in a phantom model. *European radiology* 2013;
50. Izadpanah K, Winterer J, Vicari M, et al. A stress MRI of the shoulder for evaluation of ligamentous stabilizers in acute and chronic acromioclavicular joint instabilities. *Journal of magnetic resonance imaging : JMRI* 2013; 37:1486-1492
51. Nemec U, Oberleitner G, Nemec SF, et al. MRI versus radiography of acromioclavicular joint dislocation. *AJR American journal of roentgenology* 2011; 197:968-973
52. Tauber M, Koller H, Hitzl W, Resch H. Dynamic radiologic evaluation of horizontal instability in acute acromioclavicular joint dislocations. *The American journal of sports medicine* 2010; 38:1188-1195
53. Reid D, Polson K, Johnson L. Acromioclavicular joint separations grades I-III: a review of the literature and development of best practice guidelines. *Sports medicine* 2012; 42:681-696

54. Beitzel K, Cote MP, Apostolakos J, et al. Current concepts in the treatment of acromioclavicular joint dislocations. *Arthroscopy : the journal of arthroscopic & related surgery : official publication of the Arthroscopy Association of North America and the International Arthroscopy Association* 2013; 29:387-397
55. Tauber M. Management of acute acromioclavicular joint dislocations: current concepts. *Archives of orthopaedic and trauma surgery* 2013; 133:985-995
56. Wellmann M, da Silva G, Lichtenberg S, Magosch P, Habermeyer P. [Instability pattern of acromioclavicular joint dislocations type Rockwood III: relevance of horizontal instability]. *Der Orthopade* 2013; 42:271-277
57. Garcia-Elias M, Ribe M, Rodriguez J, Cots M, Casas J. Influence of joint laxity on scaphoid kinematics. *Journal of hand surgery* 1995; 20:379-382
58. Horii E, Garcia-Elias M, An KN, et al. A kinematic study of luno-triquetral dissociations. *The Journal of hand surgery* 1991; 16:355-362
59. Garcia-Elias M, An KN, Amadio PC, Cooney WP, Linscheid RL. Reliability of carpal angle determinations. *The Journal of hand surgery* 1989; 14:1017-1021
60. Garcia-Elias M, Alomar Serrallach X, Monill Serra J. Dart-throwing motion in patients with scapholunate instability: a dynamic four-dimensional computed tomography study. *The Journal of hand surgery, European volume* 2013;
61. Garcia-Elias M. The non-dissociative clunking wrist: a personal view. *The Journal of hand surgery, European volume* 2008; 33:698-711
62. Garcia-Elias M. Kinetic analysis of carpal stability during grip. *Hand clinics* 1997; 13:151-158